

CFD Modelling of Laminar, Open-Channel Flows of Non-Newtonian Slurries

by

César Montilla Pérez

A thesis submitted in partial fulfillment of the requirements for the degree of

Master of Science

in

Chemical Engineering

Department of Chemical and Materials Engineering
University of Alberta

© César Montilla Pérez, 2017

Abstract

Current oil sands mining and bitumen extraction methods produce a significant amount of tailings. Recent legislation in Alberta aims to guarantee operators treat their tailings and reclaim them 10 years after the end of mine life. Since 2012, oil sand companies have spent more than \$1.3 billion in developing technologies to improve environmental performance and provide more sustainable operations. Generally, tailings are dewatered, and the solids concentration increases affecting the rheological properties of the mixtures. They can exhibit non-Newtonian, viscoplastic, and in some cases time-dependent behaviour which make them challenging to model. In this study, the behaviour of these clay-water-sand mixtures is studied using a commercially available CFD (Computational Fluids Dynamics) package. To achieve this, the physics of the laminar, open-channel flow of coarse particles suspended in a non-Newtonian fluid are broken down into smaller, less complex cases, to progressively validate the predictions of the CFD package. In all cases, the simulation results were compared with available experimental data. First, the laminar, open-channel flow non-Newtonian fluids is studied. The simulation results were able to predict the depth of flow, velocity field, and wall shear stress accurately. Next, fluid-particle systems are modelled in a way some mechanisms can be studied separately: shear-induced migration was studied and the simulated particle volume fraction and velocity profiles were in agreement with the experimental data. The model is unable to predict a depletion of the particle volume fraction at the wall as the experiments did. Single-particle settling in viscoplastic studied was also modelled using two available drag correlations and the particle settling velocity results were in good agreement when an equivalent Newtonian viscosity approach was used. The modelling of laminar pipeline transport of settling slurries captured the overall behaviour of the experiments; however, the CFD solver struggled with stability when the maximum particle packing concentration was approached anywhere in the flow domain. Finally, the knowledge gathered from previous modelling cases was used to study

the laminar, open-channel flow of coarse particles in non-Newtonian suspension. The model developed in this study was able to predict the settling of coarse particles when compared with experimental data. It was found that particles settle predominantly in the sheared zone where they form a stationary bed, as also indicated by the velocity profiles. In addition, a parametric study was performed to determine which flow parameters and rheological properties have a significant impact on the transport of coarse particles suspended in a non-Newtonian carrier fluid. The simulation results showed that the flow rate, mixture density, and bulk particle volume fraction are the most impactful parameters in hindering coarse particle settling. The variation of the mixture yield stress had no significant effect on coarse particle settling. An increase in particle diameter had an increasing effect on particle settling. Replacing the semi-circular channel geometry by an equivalent rectangular channel increased the size the depth the settled bed. The model presented in this study can be used to evaluate multiple conditions and for scaling purposes, or to enable the selection of a limited experimental matrix.

Acknowledgements

I would like to express my gratitude to my supervisor, Dr. Sean Sanders, for giving me the opportunity of being part of the Pipeline Transport Processes research group, and for guiding me throughout this research project.

Special thanks to Terry for her invaluable support during the project. I would also like to thank my fellow group members for all the insightful conversations.

My sincerest gratitude goes to Diego, friends, and family for their invaluable support along this journey.

This research was conducted through the support of the Institute for Oil Sands Innovation (IOSI) and the NSERC Industrial Research Chair in Pipeline Transport Processes (RSS). The contributions of Canada's Natural Sciences and Engineering Research Council (NSERC) and the Industrial Sponsors (Canadian Natural Resources Limited, CNOOC-Nexen Inc., Saskatchewan Research Council's Pipe Flow Technology Centre™, Shell Canada Energy, Suncor Energy, Syncrude Canada Ltd., Total SA, Teck Resources Ltd., and Paterson & Cooke Consulting Engineering Ltd.) are also recognized with gratitude

Table of Contents

1. Introduction	1
1.1 Oil sands overview	1
1.2 Research context and objectives	2
1.3 Thesis contents	6
1.4 Contributions	6
2. Literature review	8
2.1 Introduction	8
2.2 Fluid behaviour classification	8
2.2.1 Non-Newtonian fluids	9
2.3 Open-channel flow	10
2.3.1 Sheet flow of viscoplastic fluids	10
2.3.2 Friction losses on laminar, open-channel, flow of non-Newtonian fluids	12
2.4 Fluid-particle systems	15
2.4.1 Single-particle systems	16
2.4.2 Multi-particle systems	22
2.5 Numerical modelling	27
2.5.1 Numerical modelling of viscoplastic fluids	27
2.5.2 Numerical modelling of coarse particle suspensions	28
2.6 STAR-CCM+: Overview	29
2.6.1 Meshing capabilities	29
2.6.2 Multiphase flow modelling	32
2.6.3 Non-Newtonian flow modelling	35
2.6.4 Solution Analysis	35
3. Homogeneous, laminar, open-channel flow of non-Newtonian fluids	37
3.1 Semi-circular channel	37
3.1.1 Model validation	41
3.2 Rectangular channel	50

3.2.1	Model validation	51
3.3	Modelling limitations.....	54
3.4	Conclusions.....	55
3.5	Recommendations.....	56
4.	Fluid-particle systems – preliminary studies.....	57
4.1	Shear-induced migration.....	57
4.1.1	Model validation	60
4.2	Single-particle settling in viscoplastic fluids.....	65
4.2.1	Model validation	68
4.3	Laminar transport of coarse particles	70
4.3.1	Model validation	71
4.4	Modelling limitations.....	75
4.5	Conclusions.....	75
4.6	Recommendations.....	76
5.	Laminar, open-channel flow of thickened tailings	77
5.1	Model validation.....	79
5.2	Parametric analysis	85
5.3	Limitations.....	98
5.4	Conclusions.....	99
5.5	Recommendations.....	100
6.	Conclusions and recommendations for future work	101
6.1	Summary and conclusions.....	101
6.2	Recommendations for future work.....	102
	References.....	104
	APPENDIX A: SOFTWARE AND HARDWARE TECHNICAL SPECIFICATIONS.....	113
	APPENDIX B: SIMULATION DATA.....	116

List of Figures

Figure 1.1: Tailings pond schematic ⁵	1
Figure 1.2: Types of fluid flow behaviour (reproduced) ²⁰	3
Figure 1.3: A high-level summary of a tailings disposal design strategy ⁴	4
Figure 2.1: Schematic representation of unidirectional shearing flow ²⁰	9
Figure 2.2: Flow configuration for sheet flow reproduced from De Kee et al. ⁴⁴	11
Figure 2.3: Moody diagram showing the relationship between the Fanning friction factor and the Reynold number defined by Equation (2.21), with Re_H defined by Equation (2.17).....	15
Figure 2.4: Schematic representation of forces acting on a falling solid sphere.....	17
Figure 2.5: Shape of the sheared envelope surrounding a sphere in creeping motion through viscoplastic fluids: (a) Ansley and Smith ⁶⁷ , (b) Yoshioka et al ⁶⁸ ., (c) Beris et al. ⁶² from ⁶¹	19
Figure 2.6: Relative fall velocity versus Reynolds number ⁷⁰ with $\tau_{ref} = 0.3\tau$	21
Figure 2.7: Equation (2.39) prediction using experimental data from Valentik and Whitmore ⁷⁴ , Ansley and Smith ⁶⁷ , Wilson et al. ⁷⁰ , Tran et al. ⁷⁵ , and Shokrollahzadeh ³⁵	22
Figure 2.8: Prism layer mesher example, with (a) Progressive layer stretching and (b) Constant stretching.....	30
Figure 2.9: (a) Source, (b) target, and (c) guide surfaces for directed meshing.....	31
Figure 2.10: Directed mesh example.....	31
Figure 2.11: Example of derived parts created using STAR-CCM+: a plane and a vertical centerline inside a cylinder.....	36
Figure 3.1: Saskatchewan Research Council’s 156.7 mm flume circuit used by Spelay ¹⁷ ...	37
Figure 3.2: Mesh structure for the semi-circular channel simulations.....	38
Figure 3.3: Maximum CFL number monitor extracted from STAR-CCM+ for Case 1A.....	40
Figure 3.4: Example of residuals plot for Case 4A.....	41
Figure 3.5: Contour plot of the volume fraction of mixture for case 1A in a plane perpendicular to the flow direction.....	43
Figure 3.6: Parity plot for experimental and predicted depth of flow for the conditions shown in Table 3.3.....	43
Figure 3.7: Parity plot for experimental and predicted depth of flow for the conditions shown in Table 3.3.....	44
Figure 3.8: Wall stress distribution for Case 2B (experimental conditions shown in Table 3.3).....	45
Figure 3.9: Parity plot for experimental and predicted wall shear stress for the conditions shown in Table 3.3.....	45

Figure 3.10: Parity plot for experimental and predicted average velocity for the conditions shown in Table 3.3.....	46
Figure 3.11: Normalized centerline velocity profile comparison between experiments by Spelay and simulation results for Case 2A.	47
Figure 3.12: Normalized centerline velocity profile comparison between experiments by Spelay and simulation results for Case 2B.	47
Figure 3.13: Normalized centerline velocity profile comparison between experiments by Spelay and simulation results for Case 2G.	48
Figure 3.14: Comparison of the simulation results and Fanning friction factor correlation by Burger et al. ⁵³	49
Figure 3.15: Schematic of rectangular flume used by Haldenwang et al. ⁴⁵	50
Figure 3.16: Mesh structure for the rectangular channel simulations.....	51
Figure 3.17: Comparison of the normalized centerline velocity profile between simulations and the laminar sheet flow model ⁴⁴ for Case 3A.....	52
Figure 3.18: Comparison of the normalized centerline velocity profile between simulations and the laminar sheet flow model ⁴⁴ for Case 3B.....	53
Figure 3.19: Comparison of the normalized centerline velocity profile between simulations and the laminar sheet flow model ⁴⁴ for Case 4A.....	54
Figure 3.20: Comparison of the normalized centerline velocity profile between simulations and the laminar sheet flow model ⁴⁴ for Case 4B.....	54
Figure 4.1: (a) Schematic of the experimental setup (b) Superconducting 1.9 T magnet ²⁹	57
Figure 4.2: Mesh structure for the shear-induced migration simulations	58
Figure 4.3: Minimum particle volume fraction monitor with respect of time for Case 5B....	59
Figure 4.4: Contour plot of the particle volume fraction for Case 5B in a plane perpendicular to the flow direction	60
Figure 4.5: Contour plot of the carrier fluid velocity for Case 5B in a plane perpendicular to the flow direction	61
Figure 4.6: Developed particle volume fraction comparison between simulation results and experiments by Hampton et al. ²⁹ for Case 5A.....	61
Figure 4.7: Developed particle volume fraction comparison between simulation results and experiments by Hampton et al. ²⁹ for Case 5B.....	62
Figure 4.8: Developed particle volume fraction comparison between simulation results and experiments by Hampton et al. ²⁹ for Case 5C.....	62
Figure 4.9: Developed velocity profile comparison between simulation results and experiments by Hampton et al. ²⁹ for Case 5A.....	63

Figure 4.10: Developed velocity profile comparison between simulation results and experiments by Hampton et al. ²⁹ for Case 5B.....	64
Figure 4.11: Developed velocity profile comparison between simulation results and experiments by Hampton et al. ²⁹ for Case 5C.....	64
Figure 4.12: Schematic representation of the settling column used by Shokrollahzadeh ³⁵ .	66
Figure 4.13: Mesh representation for single-particle settling simulations.	67
Figure 4.14: Maximum particle velocity monitor plot using STAR-CCM+ for Case 10B	67
Figure 4.15: Comparison between simulation results and experiments for a particle settling in a viscoplastic fluid. Conditions listed in Table 4.5	69
Figure 4.16: Comparison between simulation results and the Newtonian drag curve	70
Figure 4.17: The 50 mm pipeflow loop used in the experiments by Gillies et al. ³² where: d) Gamma ray densitometer, g) Glass observation section, h) Heat Exchanger, a) Hot film anemometer, s) Sampler, T) Temperature sensor, V) Acrylic observation section	70
Figure 4.18: Mesh structure used in the laminar transport of coarse particles simulations.	71
Figure 4.19: Particle volume fraction profile between simulation results and experiments by Gillies et al. ³² for Case 11A.....	72
Figure 4.20: Particle volume fraction profile between simulation results and experiments by Gillies et al. ³² for Case 11B.....	73
Figure 4.21: Simulated velocity profiles for Cases 11A and 11B	74
Figure 5.1: Mesh structure used for thickened tailings simulations	77
Figure 5.2: Contour plot for particle volume fraction, 14.5 m away from the channel inlet, perpendicular to the flow, for Case 12B.....	80
Figure 5.3: Contour plot for mixture velocity magnitude 14.5 m away from the channel inlet, perpendicular to the flow, for Case 12B.....	80
Figure 5.4: Chord-averaged particle volume fraction comparison between simulation results and experiments by Spelay ¹⁷ for Case 12A	81
Figure 5.5: Chord-averaged particle volume fraction comparison between simulation results and experiments by Spelay ¹⁷ for Case 12B	81
Figure 5.6: Chord-averaged particle volume fraction comparison between simulation results and experiments by Spelay ¹⁷ for Case 12C	82
Figure 5.7: Chord-averaged particle volume fraction comparison between simulation results and experiments by Spelay ¹⁷ for Case 12D	82
Figure 5.8: Simulated centerline velocity profile for the carrier fluid, 14.5 m away from the channel inlet, for Case 12B.....	83
Figure 5.9: Particle volume fraction variation with time for case 10B	84

Figure 5.10: Simulated maximum particle volume fraction variation with distance from the inlet	85
Figure 5.11: Simulated maximum wall shear stress variation with distance from the inlet.	85
Figure 5.12: Chord-averaged particle volume fraction variation with carrier fluid yield stress	86
Figure 5.13: Predicted carrier fluid centerline velocity profile with varying carrier fluid yield stress.....	87
Figure 5.14: Chord-averaged particle volume fraction profile with varying channel diameter and depth of flow	88
Figure 5.15: Predicted carrier fluid centerline velocity profile with varying channel diameter and depth of flow	88
Figure 5.16: Chord-averaged particle volume fraction profile with varying channel diameter and constant depth of flow	89
Figure 5.17: Predicted carrier fluid centerline velocity profile with varying channel diameter and constant depth of flow	89
Figure 5.18: Chord-averaged particle volume fraction profile in a semi-circular and rectangular channel.....	90
Figure 5.19: Predicted carrier fluid centerline velocity profile in a semi-circular and rectangular channel.....	90
Figure 5.20: Contour plot for velocity of the particle phase 14.5 m away from the channel inlet in: (a) Semi-circular channel and (b) rectangular channel	91
Figure 5.21: Contour plot for shear stress 14.5 m away from the channel inlet in: (a) Semi-circular channel and (b) rectangular channel.....	92
Figure 5.22: Chord-averaged particle volume fraction with varying particle diameter	93
Figure 5.23: Predicted carrier fluid centerline velocity profile with varying particle diameter	93
Figure 5.24: Chord-averaged particle volume fraction with varying particle volume fraction	94
Figure 5.25: Relative particle volume fraction profiles with varying inlet particle volume fraction	94
Figure 5.26: Carrier fluid velocity profiles with varying inlet particle volume fraction	95
Figure 5.27: Chord-averaged particle volume fraction with varying carrier fluid density	95
Figure 5.28: Predicted carrier fluid centerline velocity profile with varying carrier fluid density	96
Figure 5.29: Chord averaged particle volume fraction profile with varying flow rate	97

Figure 5.30: Normalized centerline velocity profile with varying flow rate 97

List of Tables

Table 1.1: Tailings management technologies used in current oil sands mining projects	2
Table 2.1: Drag coefficient correlations based on the particle's Reynolds number	16
Table 3.1: STAR-CCM+ models used on the semi-circular channel simulations	39
Table 3.2: Rheological properties of the mixtures modelled in this study ¹⁷	41
Table 3.3: Experimental conditions considered for modelling in the semi-circular channel reported by Spelay ¹⁷	42
Table 3.4: Rheological properties of the fluids evaluated by Haldenwang et al. ⁴⁵	51
Table 3.5: Experimental conditions considered for modelling in the rectangular channel reported by Haldenwang et al. ⁴⁵	51
Table 4.1: STAR-CCM+ models used in the modelling of shear-induced migration	58
Table 4.2: Experimental conditions modelled for shear-induced migration ²⁹	60
Table 4.3: Experimental entrance length and simulated average wall shear stress for cases in Table 4.2.....	65
Table 4.4: STAR-CCM+ models used in the single-particle settling simulations	66
Table 4.5: Experimental conditions used in the particle settling simulations of the present study ³⁵	68
Table 4.6: Modelling approaches for a solid sphere settling in a viscoplastic fluid.....	68
Table 4.7: Experimental conditions modelled for the laminar transport of settling slurries.	72
Table 5.1: STAR-CCM+ models used to model thickened tailings.....	78
Table 5.2: Mixture and particle properties used in the modelling of the laminar, open-channel flow of thickened tailings ¹⁷	79
Table 5.3: Experimental conditions modelled in the transport of coarse particle suspended in a viscoplastic fluid.....	79

List of Symbols

Symbol	Description	Units
A	Area	m^2
a	Geometrical parameter for the Kozicki and Tiu model	-
a	Numerical constant for the Blasius equation	-
a	Particle radius	m
a_T	Temperature factor (Equation 2.68)	-
Bi_{HB}	Bingham number	-
b	Geometrical parameter for the Kozicki and Tiu model	-
b	Numerical constant for the Blasius equation	-
C_D	Drag coefficient	-
C_2	Quadratic coefficient (Equation 2.44)	-
c	Numerical constant for the Blasius equation	-
d	Numerical constant for the Blasius equation	-
d	Particle diameter	m
e	Fitting parameter (Equation 2.18)	-
F_1	Power law relationship for laminar flows	-
F_2	Power law relationship for turbulent flows	-
F_B	Buoyancy force	N
F_D	Drag force	N
F_G	Gravity force	N
$(\mathbf{F}_{int})_i$	Internal forces of the i^{th} phase (Equation 2.65)	N
\mathbf{F}_s	Surface forces acting on the particle	N
\mathbf{F}_b	Body forces acting on the particle	N
$f(\phi)$	Hindrance function	-
$f_{Newtonian}(\phi)$	Hindrance function for a Newtonian fluid	-
f	Fanning friction factor	-
\mathbf{g}	Gravity force vector	m/s^2
g	Gravity force magnitude	m/s^2
h	Depth of flow	m
j	Fitting parameter (Equation 2.18)	-
K_s	Contact contribution (Equation 2.47)	-
K_s	Sedimentation flux coefficient (Equation 2.57)	kg/m^3

K	Numerical constant dependent of channel shape	-
K_c	Proportional constant (Equation 2.53)	-
K_η	Proportional constant (Equation 2.54)	-
K_n	Contact contribution (Equation 2.55)	-
k	Consistency index	Pa.s ⁿ
k_r	Relative consistency index	-
m_{ij}	Mass transfer rate to phase i, from phase j ($m_{ij} \geq 0$).	kg/s
m_{ji}	Mass transfer rate to phase j, from phase i ($m_{ji} \geq 0$).	kg/s
m_p	Particle mass	kg
N_s	Flux due to sedimentation (Equation 2.57)	m/s
N_c	Flux due to spatially varying interaction (Equation 2.53)	m/s
N_η	Flux due to spatially varying viscosity (Equation 2.54)	m/s
n	Power law exponent	-
n_r	Relative power law exponent	-
p	Pressure	Pa
Q^*	Modified dynamic parameter	-
Re	Reynolds number	-
Re^*	Shear Reynolds number	-
Re_B^*	Reynolds number for Bingham fluids in open-channel flow	-
Re_B	Abulnaga's Reynolds number	-
Re_H	Haldenwang et al. Reynolds number	-
Re_p	Particle Reynolds number	-
Re_{PL}	Reynolds number for power law fluids	-
Re_p^*	Reynolds number for power law fluids in open-channel flow	-
Re_{Zhang}	Zhang's Reynolds number	-
R_h	Hydraulic radius	m
s_i^α	Phase mass source term (Equation 2.66)	kg/m ³
s_i^V	Phase momentum source term (Equation 2.65)	kg*m/s
t	Fitting parameter (Equation 2.18)	-
\bar{V}	Average velocity	m/s
V_∞	Particle terminal velocity	m/s
$V_{\infty,s}$	Hindered particle settling velocity	m/s

V^*	Shear velocity	m/s
V_x	Velocity component in the X direction	m/s
$V_y^<$	Velocity component in the Y direction in the plug	m/s
$V_y^>$	Velocity component in the Y direction in the sheared zone	m/s
v_g	Grid velocity (Equation 2.64)	m/s
v_p	Particle velocity	m/s
$X(n)$	Deviation factor	-
x_0	Distance between the free surface and the yielding transition surface	m
Y_G	Static equilibrium parameter	-

Greek symbols

Symbol	Description	Units
α	Channel slope with respect of the horizontal	degrees
α	Rheogram shape factor (Equation 2.39)	-
α	Drag force constant (Equation 2.60)	-
α_B	Rheogram shape factor calculated from the Bingham model	-
$\dot{\gamma}$	Shear rate	s ⁻¹
$\bar{\gamma}_l(\phi)$	Average local shear rate (Equation 2.60)	s ⁻¹
η_r	Relative viscosity	-
η_s	Viscosity of the suspension	Pa.s
η_c	Viscosity of the carrier fluid	Pa.s
[η]	Krieger and Dougherty exponent	-
μ	Newtonian viscosity	Pa.s
μ_{app}	Apparent viscosity	Pa.s
μ_{eq}	Equivalent viscosity	Pa.s
μ_i	Dynamic viscosity of the i th phase	Pa.s
μ_0	Yielding viscosity	Pa.s
μ_p	Bingham plastic viscosity	Pa.s
ξ	Relative shear stress	-
ρ	Density	kg/m ³

ρ_i	Density of the i^{th} phase	kg/m^3
ρ_s	Particle density	kg/m^3
ρ_f	Fluid density	kg/m^3
τ	Shear Stress	Pa
$\bar{\tau}$	Mean surficial stress (Equation 2.36)	Pa
τ_i	Molecular stress (Equation 2.65)	Pa
τ_i^t	Turbulent stress (Equation 2.65)	Pa
τ_{ref}	Reference shear stress	Pa
τ_w	Wall shear stress	Pa
τ_{xy}	Shear stress at any point X on a surface parallel to Y-axis	Pa
τ_y	Yield stress	Pa
τ_y^B	Bingham yield stress	Pa
τ_y^H	Herschel-Bulkley yield stress	Pa
τ_{yr}	Relative yield stress	-
ϕ	Particle volume fraction	-
ϕ_{max}	Particle maximum packing volume fraction	-
χ	Yield stress to wall shear stress ratio	-
χ	Void fraction	-

1. Introduction

1.1 Oil sands overview

Every mining operation in the world produces tailings. This is particularly important in the process of mining oil sand and extracting bitumen for upgrading to synthetic crude oil, as significant volumes of fluid fine tailings are produced. For instance, historical production rates of 1 million barrels of oil per day^{1,2} result in approximately 0.3 million m³ tailings produced per day³. These mixtures are composed of water, clay, sand, and some residual bitumen. Without going into details of any specific mining operation, a generalized description can be given. Tailings are discharged in ponds in which, ideally, the mixture separates due to gravity into different layers: coarse sand settles first, then a mixture of fine solids remains which is transferred to another settling basin, where some of the water can be reclaimed back to the extraction process, as shown in Figure 1.1. However, while the coarse particles (i.e. particle size > 44 µm) settle quickly to the bottom of the pond, fine solids and clay particles suspended in water form a stable mixture which makes the fine solids very difficult to settle, and makes reclamation problematic. This raises environmental concerns such as water usage, land disruption, and dam failures⁴.

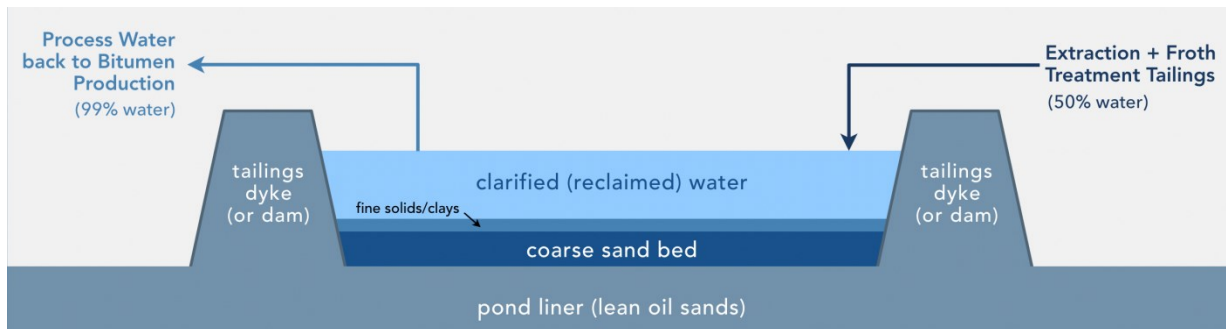


Figure 1.1: Tailings pond schematic⁵.

Alberta has proven reserves of 166 billion barrels, making it the third largest oil reserves in the world, as of 2014⁶. In 2015, the Government of Alberta released the Lower Athabasca Region: Tailings Management Framework for Mineable Athabasca Oil Sands (TMF)⁷, which provides the Alberta Energy Regulator (AER) and industry with strategies to manage properly new and existing tailings. The main objective of the TMF is to minimize fluid tailings accumulation by guaranteeing that tailings are treated and reclaimed throughout the project so that they are ready to reclaim ten years after the end of mine life of that project. Furthermore, in 2016, the AER released Directive 085: Fluid Tailings Managements for Oil Sands Mining Projects⁸ which holds operators accountable for the responsible treatment of their fluid tailings.

Since 2012, oil sand companies have spent more than \$1.3 billion in developing technologies to improve environmental performance and provide more sustainable operations focusing in 4 major areas: greenhouse gases, water, land, and tailings⁹. In the management of tailings, most projects are focused on accelerated dewatering as it leads to more efficient process water recycling (and thus reduced fresh water consumption) and greatly reduces tailings production rates and storage volumes³. Table 1.1 shows a summary of the tailings management technologies used in current projects.

Table 1.1: Tailings management technologies used in current oil sands mining projects

Operator	Mining project	Technology
Canadian Natural Resources Ltd ¹⁰⁻¹²	Horizon mine	Non-segregated Tailings (NST)
	Muskeg river mine	Thickened tailings, composite tailings (CT), atmospheric fines drying (AFD)
	Jackpine mine	
Imperial Oil Resources Limited ¹³	Kearl oil sands	Thickened tailings
Suncor ¹⁴	Millennium	Tailings reduction operations (TRO)
	Steepbank	
	Forth Hills	
Synchrude Canada Ltd ¹⁵	Aurora north	Composite tailings (CT)
	Mildred Lake	

1.2 Research context and objectives

This study is focused on the behaviour of clay-water and clay-water-sand mixtures once they have been discharged in a tailings dedicated disposal area (DDA), where the mixtures flow in sheets or naturally-formed open channels^{16,17}. When the tailings are dewatered, the solids concentration increases which significantly affects the rheological properties of the mixtures; they can exhibit non-Newtonian, viscoplastic, and in some cases time-dependent behaviour¹⁸. When the fine tailings exhibit non-Newtonian behaviour, it has been shown that an increase in the fines solid concentration will produce an increase in the mixture yield stress¹⁹.

Fluids can be classified as Newtonian or non-Newtonian, based on the relationship between the shear stress and the shear rate²⁰. Figure 1.2 shows a general classification: Newtonian

fluids are characterized by a linear relationship between shear stress and shear rate, where the slope of the line is defined as the Newtonian viscosity of the fluid. Non-Newtonian fluids usually show a non-linear relationship and can be further classified as dilatant, pseudo-plastic, or viscoplastic, the latter being characterized by the presence of a yield stress, defined as stress required for the material to flow. Below this threshold, the material will behave as an elastic solid. There are several mathematical models to describe the non-Newtonian flow behaviour and they will be explained in more detail in Chapter 2.

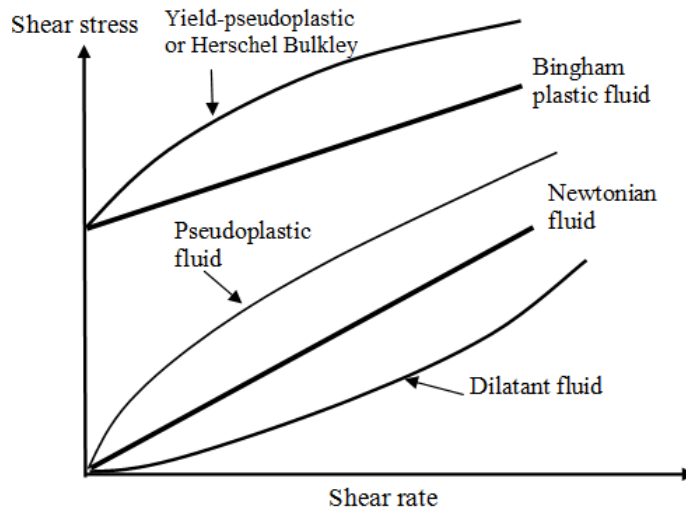


Figure 1.2: Types of fluid flow behaviour (reproduced)²⁰.

Typically, the design of the tailings disposal system begins with the design of a thickener, which provides an overflow that can be reused in the process. The underflow or dewatered tailings, exhibit non-Newtonian behaviour. Their high apparent viscosity makes it cost-prohibitive to operate under turbulent conditions, in most cases. Thus, most dewatered tailings lines operate under laminar flow conditions. As such, it becomes critical to understand the underlying mechanisms involved in coarse solids transport under these conditions¹⁷ because of the implications in the pump system design/power consumption. For example, consider the design sequence shown in Figure 1.3, which suggests that one should design the disposal system back-to-front; namely, selecting the disposal method first, then the designing the pumping system, and ending with the thickener design, or the method by which the tailings are dewatered. The rheological properties of the tailings are needed to predict consolidation, as well as for the design of the tailings line, and the suction side of the pump for the thickener⁴.

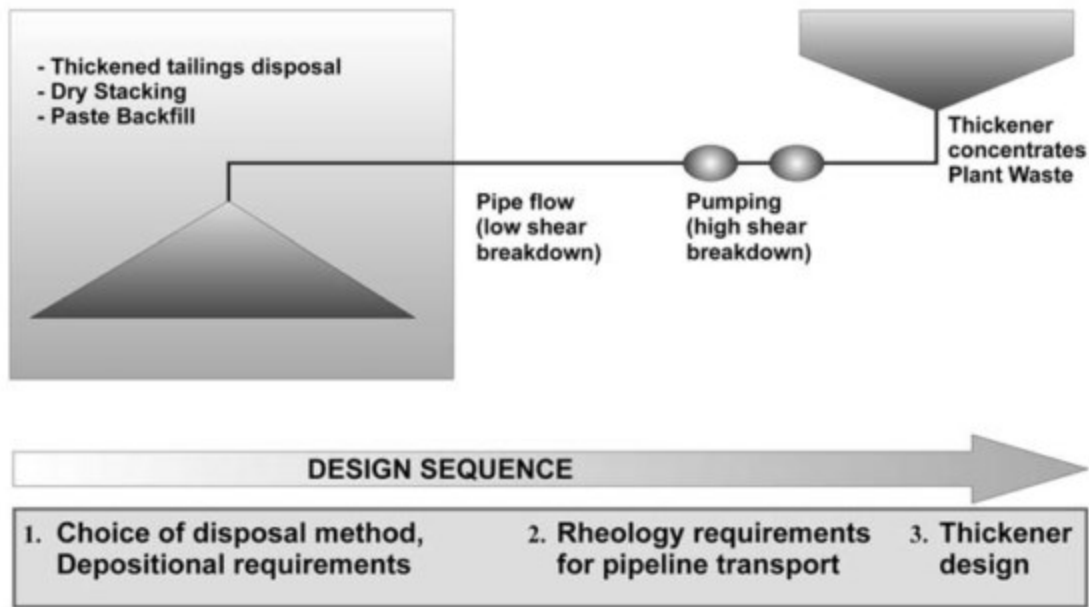


Figure 1.3: A high-level summary of a tailings disposal design strategy⁴

Advances in hardware and in Computational Fluids Dynamics (CFD) techniques have permitted the use of CFD in many areas, such as sports, automotive, chemical and mineral processing, civil and environmental engineering, heat transfer, power generation, among others. Simulations can complement experiments, providing a cost-effective way to study multiple scenarios that would be otherwise difficult, or even impossible, with experiments²¹. However, modelling tailings mixtures poses many challenges because they are non-Newtonian (usually viscoplastic), time-dependent, and contain coarse (settling) particles^{17,22}. One of the challenges in modelling yield stress fluid flows is to properly represent the region where the shear stress is below the yield stress²³. Methods have been developed to overcome this and will be explained in more detail in Chapter 2.

Solid particles suspended in a fluid are known to affect the resistance of the mixture to flow, or its suspension viscosity, which has been found to be an increasing function of the solid particle volume fraction²⁴. For concentrated suspensions, where the particle volume fraction is greater than 0.15, the suspension viscosity increases rapidly with particle volume fraction²⁴; semi-empirical correlations have been proposed to account for this effect²⁵⁻²⁷. Other phenomena that can be present when studying suspensions is the shear-induced migration of solid particles because of gradients in shear rate²⁸⁻³⁰, and hindered-settling when dealing with particles that are heavier than the suspending fluid^{31,32}.

Few numerical studies have been performed to study the open-channel flow of coarse particle, non-Newtonian suspensions. For example, Spelay¹⁷ studied the behaviour of tailings mixtures for a variety of conditions both experimentally and numerically. He attempted to use a commercial CFD package to model tailings mixtures, however, the CFD packages at the time were unable to incorporate the physics of the problem properly. Thus, he developed his own code that could predict the behaviour of laminar, open-channel flow of tailings. Despite the model being limited to one-dimensional flow of suspensions, he could validate the model for the laminar flow of thickened tailings successfully. Treinen and Jacobs³³ used commercial software to study particle settling and shear-induced migration in viscoplastics fluids. Their results were able to capture overall behaviour but their predictions differ from experimental results. Sittoni et al³⁴ proposed a 2DV (two dimensional vertical) numerical module, referred to as Delft3D slurry. The authors showed some promising preliminary results but their model requires further validation.

As shown above, most numerical models are limited to one or two-dimensional studies, and some of their results need further validation using experimental studies. Thus, the objective of this project is to develop a reliable, three-dimensional model that can predict the flow behaviour of non-Newtonian tailings mixtures, using a commercial CFD package. In addition, one of the overall objectives of this work is to study the main parameters that govern the transport of monodisperse coarse solids in these mixtures. To achieve this, the physics of the laminar, open-channel flow of coarse particles in non-Newtonian suspensions are broken down into smaller, less complex cases, to progressively validate the predictions of the CFD package. The modelling is divided in the following cases: laminar, open-channel flow non-Newtonian fluids; fluid-particle systems, which include shear-induced migration, single-particle settling, laminar pipeline transport of settling slurries, and laminar, heterogeneous, open-channel flow of coarse particles in non-Newtonian suspensions. Each modelling stage is validated using available experimental data and correlations from a variety of studies. In summary, to complete the project, the following activities were undertaken:

- Model and validate the laminar, homogeneous, open-channel flow of non-Newtonian fluids
- Model and validate the shear-induced migration of solid particles suspended in a Newtonian carrier fluid
- Model and validate the single-particle settling of a sphere through a viscoplastic fluid
- Model and validate the laminar pipeline transport of coarse particles suspended in a Newtonian fluid

- Model and validate the laminar, heterogeneous, open-channel flow of non-Newtonian fluids

1.3 Thesis contents

The thesis contains six chapters, including the current one. Chapter 2 provides a literature review of the main concepts and studies relevant to the project, including an overview of STAR-CCM+, the commercial CFD package used throughout this project.

In Chapter 3, the focus is on the open-channel flow of homogeneous, non-Newtonian fluids. The predictions of the CFD model are tested against experimental data, using parameters that fully describe these type of flows, i.e., depth of flow, fluid velocity and wall shear stress. Limitations, conclusions, and recommendations specific to the application of the CFD model to these types of flows are included at the end of the chapter.

In Chapter 4, a number of different fluid-particle systems are evaluated. Specifically, the chapter focuses on characteristic behavior of suspensions: shear-induced migration, single-particle settling and laminar pipeline transport of settling slurries. For this evaluation, the following studies were considered: Hampton et al.²⁹ studied the shear-induced migration of solid particles suspended in a Newtonian fluid using nuclear magnetic resonance (NMR); Shokrollahzadeh³⁵ studied the single-particle settling of spheres through viscoplastic fluids; and Gillies et al.³² studied the laminar pipeline transport of coarse particles suspended in a Newtonian fluid. Limitations, conclusions, and recommendations specific to these simulations are included at the end of the chapter.

In Chapter 5, the results from previous chapters are combined, and a model to characterize the flow behavior of non-Newtonian suspensions under laminar, open-channel flow is presented. This model is validated with the experimental data of Spelay¹⁷. In addition, a parametric study is performed to determine the suspension properties and flow parameters that have dominant effects on monodisperse coarse particle transport. At the end of the chapter, modelling limitations, conclusions, and recommendations are shown.

Finally, Chapter 6 contains a summary and extended discussion of the main findings of this project, an assessment of the extent to which the objectives of this project were accomplished, and recommendations for future work.

1.4 Contributions

There are currently few numerical models that can be used to study coarse particle transport in non-Newtonian fluids. This project presents a three-dimensional numerical

model, developed using a commercial CFD package, to study the behaviour of monodisperse non-Newtonian suspensions flowing under laminar, open-channel flow conditions.

The model uses rheological properties, volume fraction of the phases, carrier fluid and solid particle properties, as well as operating conditions as inputs. Although the model was validated successfully using data from previous studies, the available experimental data sets were limited to four conditions. The author therefore recommends that more experimental studies are needed to further validate the model.

Fluid dynamics researchers can benefit from the model presented in this project by using it to plan their experimental protocols and in identifying relevant conditions when time and resources might be limited. The model can also help visualize flow phenomena when flow visualization from experiments is difficult. CFD researchers can continue to expand the modelling capabilities as advances in software and hardware become available. Design engineers can use this model in the preliminary design of tailings disposal systems. In addition, design and operations engineers can use the model to assess multiple conditions and their effect on the transport of thickened tailings for their specific conditions.

2. Literature review

2.1 Introduction

This chapter contains a review of the most relevant literature to the primary objective of the project; namely, to apply a commercial CFD model that can predict the behaviour of non-Newtonian suspensions flowing under laminar, open-channel flow conditions.

First, a general summary fluid behaviour classification is presented. This will provide the reader with a basic understanding of rheology concepts and will highlight distinct characteristics of Newtonian and non-Newtonian fluids. In addition, the relevant constitutive equations that can describe the behaviour of different non-Newtonian fluids are shown, as these are critical to the mathematical modelling of the fluids and slurries described in the thesis.

Next, open-channel flows are discussed and a model to study laminar sheet flows is introduced, which is relevant to the results presented in Chapter 3. In addition, the friction losses on open channels are explained, along with the definition of the Reynolds number for non-Newtonian fluids, and how it relates to friction losses.

Subsequently, fluid-particle systems are discussed. This section is divided into single-particle and multi-particle systems, and provide the framework to understand characteristic phenomena of these systems. The results in Chapter 4 and 5 can be understood after this background has been presented.

Finally, an overview of STAR-CCM+, the CFD package used in this study is given, which provides with the terminology and models used throughout this project.

2.2 Fluid behaviour classification

A Newtonian fluid is characterized by a linear relationship between its viscous stresses and shear rate. Consider a fluid between two parallel plates separated by small distance (compared to lateral dimensions) dy apart, as shown in Figure 2.1. If a force F is applied to the top plate, the fluid is sheared, which will be balanced by an internal frictional force in the fluid. Under laminar flow, the resulting shear stress is equal to the product of the shear rate and the viscosity of the fluid, and can be expressed as follows:

$$\frac{F}{A} = \tau = \mu \left(-\frac{dV_x}{dy} \right) = \mu \dot{\gamma} \quad (2.1)$$

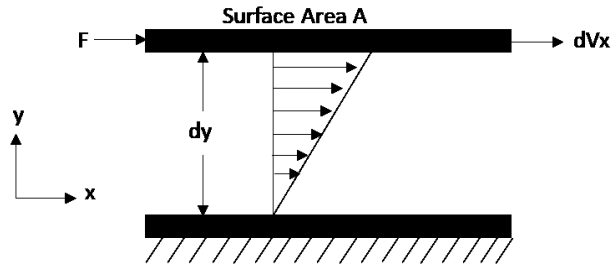


Figure 2.1: Schematic representation of unidirectional shearing flow (reproduced)²⁰.

The constant of proportionality, μ , also known as the Newtonian viscosity, is independent of shear rate ($\dot{\gamma}$) or shear stress (τ). The plot of shear stress against shear rate for a Newtonian is a straight line of slope μ , which passes through the origin (as shown in Figure 1.2)²⁰.

2.2.1 Non-Newtonian fluids

Most of the mixtures that are modelled in this study behave as non-Newtonian fluids. These types of fluids show a non-linear relationship between the shear rate and shear stress. While this feature is useful to differentiate them from Newtonian fluids, there are several subcategories for non-Newtonian fluids, which were summarized in the previous chapter, in Figure 1.2.

A dilatant, or shear-thickening fluid is characterized by an increase in the apparent viscosity with increasing shear rate; a mixture of corn starch and water is a good example of this type of fluid. Pseudo-plastic, or shear-thinning fluids are the most common type of non-Newtonian fluids observed²⁰. Their apparent viscosity decreases with increasing shear rate; quicksand is a natural example of a shear-thinning fluid. A viscoplastic, or yield stress fluid, will deform as an elastic body when the magnitude of an external stress is smaller than the yield stress. Once the applied stress exceeds the yield stress, the material will flow. As a consequence, the flow curve for this type of fluid may or may not be linear but it will not pass through the origin²⁰. Toothpaste, mayonnaise, cement, and drilling mud are examples of common viscoplastic fluids. It will be shown later in the thesis how the intrinsic differences between these model affects how they are modelled and studied.

i. Constitutive rheological equations for non-Newtonian fluids

Several empirical models have been proposed to account for the behaviour of viscoplastic fluids; only the ones relevant to this project, shown for one dimensional steady shear, are defined²⁰ here:

- The Power law model describes the behaviour of the behavior of shear-thinning and shear-thickening fluids.

$$\tau = k\dot{\gamma}^n \quad (2.2)$$

- The Bingham plastic model is the simplest model to describe flow behaviour of fluids with a yield stress

$$\tau = \tau_y^B + \mu_p \dot{\gamma} \quad \text{for } |\tau| > |\tau_y^B| \quad (2.3)$$

- The Herschel-Bulkley model is used for fluids that exhibit a non-linear behaviour between shear stress and shear rate. It is a three-parameters model, providing a better fit for experimental data.

$$\tau = \tau_y^H + k\dot{\gamma}^n \quad \text{for } |\tau| > |\tau_y^H| \quad (2.4)$$

2.3 Open-channel flow

As mentioned before, this project focuses mostly on the open-channel flow of non-Newtonian mixtures. Because this type of flow is not entirely bounded, it is characterized by a free surface which is highly deformable. Furthermore, in open channel flows, the pressure gradient is not the driving force that produces flow, rather, it is the balance between gravity and friction what governs the flow, which can sometimes make tailings transport via open-channel flow more economical than pipe flow, in some cases⁴. The open-channel flow of Newtonian fluids has been extensively studied^{36,37,38}. In contrast, until recently^{4,39,40} there has been few studies of open-channel flow applications of non-Newtonian fluids^{41,42}, which can be found in food processing, oil and gas, and mining industries.

In the subsequent sections, the sheet flow of viscoplastic fluids and the friction losses of non-Newtonian fluids under open-channel flow are described. This background is necessary to understand the results presented in Chapter 3.

2.3.1 Sheet flow of viscoplastic fluids

The one-dimensional case of open-channel flow, where the depth of flow is very small when compared to the channel lateral dimensions, is called sheet flow or film flow. Coussot⁴³ proposed a ratio of depth of flow to flume width ratio of 1:10 for the flume flow of non-Newtonian fluids to be considered sheet flow. This case is studied in Chapter 3 for the

validation of the CFD model to study the homogeneous, open-channel flow of non-Newtonian mixtures.

In 1990, De Kee et al⁴⁴. studied the steady, laminar, one dimensional, fully developed flow of viscoplastic fluids along an inclined plane. They used the Herschel-Bulkley model, defined in Equation (2.3), to describe the fluid behaviour, and proposed a laminar sheet model to fully describe this type of flow; a schematic of the flow configuration can be seen in Figure 2.2.

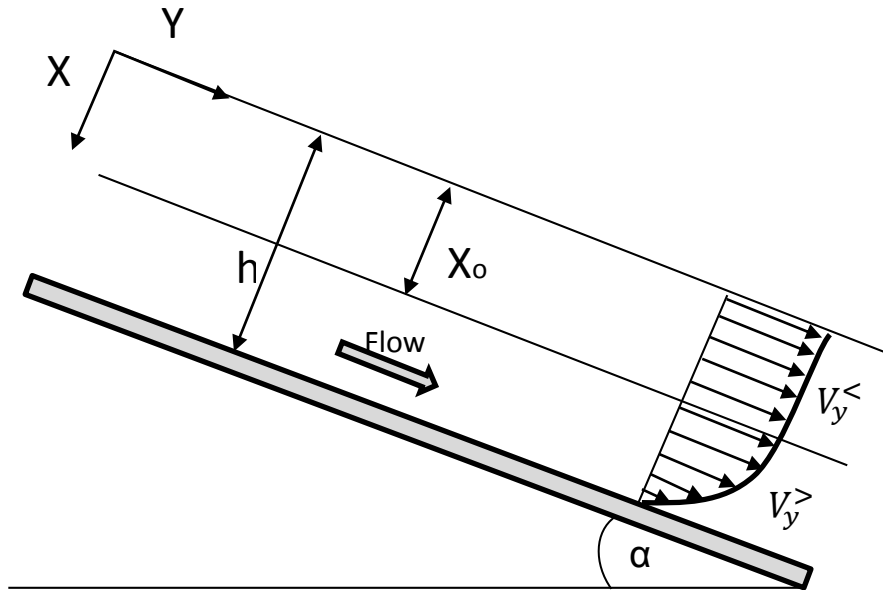


Figure 2.2: Flow configuration for sheet flow reproduced from De Kee et al.⁴⁴

By using the equations of continuity and motion, it was shown that:

$$\tau_{xy} = \rho g x \sin \alpha \quad (2.5)$$

At the wall, the maximum shear stress is determined by

$$\tau_w = \rho g h \sin \alpha \quad (2.6)$$

Figure 2.2 shows there is a plug-like region where the velocity will be constant, and hence, the shear rate is zero whereas the shear stress is equal to the yield stress. In the plug, described by, $0 \leq x \leq x_0$, the velocity is predicted using

$$V_y^< = \frac{nk}{(n+1)\rho g \sin \alpha} \left(\frac{\tau_w}{k}\right)^{\left(\frac{n+1}{n}\right)} \left(1 - \frac{\tau_y}{\tau_w}\right)^{\left(\frac{n+1}{n}\right)} \quad (2.7)$$

Below the plug, where $x_0 < x \leq h$, the point velocity is given by

$$V_y^> = \frac{nk}{(n+1)\rho g \sin \alpha} \left(\frac{\tau_w}{k}\right)^{\left(\frac{n+1}{n}\right)} \left(1 - \frac{\tau_y}{\tau_w}\right)^{\left(\frac{n+1}{n}\right)} \left(1 - \left(\frac{\frac{\tau_{xy}}{\tau_y} - 1}{\frac{\tau_w}{\tau_y} - 1}\right)^{\left(\frac{n+1}{n}\right)}\right) \quad (2.8)$$

The average velocity is given by

$$\bar{V} = \frac{nk}{(2n+1)\rho g \sin \alpha} \left(\frac{\tau_w}{k}\right)^{\left(\frac{n+1}{n}\right)} \left(1 - \frac{\tau_y}{\tau_w}\right)^{\left(\frac{n+1}{n}\right)} \left(1 + \left(\frac{n+1}{n}\right) \frac{\tau_y}{\tau_w}\right) \quad (2.9)$$

This model will be used in the simulation cases of Chapter 3. It was recently validated by Haldenwang et al⁴⁵, who performed experiments using Ultrasonic Velocity Profiling (UVP) to characterize the behaviour of non-Newtonian fluids in a rectangular flume.

2.3.2 Friction losses on laminar, open-channel, flow of non-Newtonian fluids

Predicting the friction losses is an important component in designing and characterizing open-channel flows. In this section, the different methods that have been proposed are reviewed. These methods are most often based on a reworking of the Reynolds number. Thus, a review of the Reynolds number definitions for non-Newtonian fluids is also provided.

Alderman and Haldenwang⁴⁶ performed a review of the available models to predict the open channel flow of non-Newtonian fluids in a rectangular channel using the experimental data from Haldenwang and Slatter⁴⁷. For laminar flow, the database consisted of experimental data for CMC solutions, kaolin suspensions, and bentonite suspensions. An in-line tube viscometer was used for rheological characterization. For each type of fluid, the comparison was made by calculating the non-Newtonian Reynolds number as defined by each author and the Fanning friction factor, for open-channel flow, defined as

$$f = \frac{2\tau_w}{\rho \bar{V}^2} = \frac{2R_n g \sin \theta}{\bar{V}^2} \quad (2.10)$$

The calculated results were then compared against the following equation for laminar flow:

$$f = \frac{16}{Re} \quad (2.11)$$

Multiple definitions for the non-Newtonian Reynolds number have been proposed. Kozicki and Tiu⁴⁸ proposed a method for modelling the steady, fully developed laminar flow of any

time-independent non-Newtonian fluid in a channel of arbitrary cross section. They based the method on a generalization of the Rabinowitsch-Mooney analysis for flow in circular tubes and derived expressions of the Reynolds number, for Power Law and Bingham Plastic fluids, Re_p^* and Re_B^* , respectively:

$$Re_p^* = \frac{\rho \bar{V}^{2-n} R_h^n}{2^{n-3} k \left(\frac{a + bn}{n} \right)^n} \quad (2.12)$$

$$Re_B^* = \frac{4R_h \bar{V} \rho}{\eta_B} \left[\frac{1}{a+b} - \frac{\chi}{b} + \frac{a}{b(a+b)} \chi^{\left(\frac{b}{a}\right)+1} \right] \quad (2.13)$$

where a and b are geometrical parameters, characteristic of the shape of the flow geometry, χ is the ratio of the Bingham yield stress to wall shear stress, and R_h is the hydraulic radius, defined as

$$R_h = \frac{\text{cross - sectional area to flow}}{\text{wetted perimeter of conduit}} \quad (2.14)$$

In addition, Zhang and Ren⁴⁹ proposed an expression for the Reynolds number of Bingham plastic fluids, based on their studies of river flow mud in a rectangular open-channel, defined as

$$Re_{Zhang} = \frac{8\rho \bar{V}^2}{\tau_y^B + \mu_P \left(\frac{2\bar{V}}{R_h} \right)} \quad (2.15)$$

Abulnaga⁵⁰ modified the Buckingham equation for pipe flow by expressing the Reynolds number for Bingham plastic fluids in terms of hydraulic radius of the channel:

$$Re_B = \frac{4R_h \bar{V} \rho}{\mu_P} \quad (2.16)$$

Haldenwang et al.⁵¹ also proposed a Reynolds number definition, representing the viscous stresses of the fluids using the Herschel-Bulkley model.

$$Re_H = \frac{8\rho \bar{V}^2}{\tau_y + k \left(\frac{2\bar{V}}{R_h} \right)^n} \quad (2.17)$$

This definition can be used for Power Law, Bingham plastic, and Herschel-Bulkley fluids by substituting the corresponding rheological parameters. During their experiments, they evaluated carboxymethylcellulose (CMC) solutions, kaolin suspensions, and bentonite suspensions.

As mentioned above, each Reynolds number definition was compared with the $f = 16/Re$ line. For Power Law fluids, the comparison was made between the definitions described by Equations (2.12) and (2.17), and it was determined that both definitions predicted the friction losses accurately, when compared with Equation (2.11). For Bingham plastic fluids, the comparison was made using the Reynolds number defined by Equations (2.13), (2.15), (2.16), and (2.17). Only the definitions given by Equations (2.15) and (2.17) collapsed on the $f = 16/Re$ line accurately. For Herschel-Bulkley fluids, only the Reynolds number defined by Equation 2.17 was available at the time and was found to predict the friction losses accurately, when compared with Equation (2.11).

Burger et al.⁵² later confirmed that for non-Newtonian, laminar open-channel flows the friction factor to Reynolds number relationship depends on channel shape, similar to the case of Newtonian, laminar, open-channel flow, where the laminar friction losses are defined by $f = K/Re$, where K is a numerical constant dependent on channel shape³⁶. Through their experiments using flumes with different cross-sectional shapes, they determined values of the constant K for rectangular, semi-circular, triangular, and trapezoidal flumes.

More recently, Burget et al.⁵³ expanded that approach to turbulent flow regimes by using a composite power law approach⁵⁴, given by

$$f = F_2 + \frac{(F_1 - F_2)}{\left(1 + \left(\frac{Re}{t}\right)^e\right)^j} \quad (2.18)$$

where e , t and j are fitting parameters; F_1 and F_2 are the power law relationships covering the laminar and turbulent flows respectively:

$$F_1 = aRe^b \quad (2.19)$$

$$F_2 = cRe^d \quad (2.20)$$

In Equation (2.19) a has same value of K , dependent of channel shape as mentioned above; and b has a numerical value of -1. In Equation (2.20) c and d are constants determined for a modified Blasius Equation.

Based on the approach by Burger et al. ⁵³, the Fanning friction factor for a Bingham plastic fluid in a semi-circular channel can be written as

$$f = 0.048Re_H^{-0.2049} + \frac{(16.2Re_H^{-1} - 0.048Re_H^{-0.2049})}{\left(1 + \left(\frac{Re_H}{1055}\right)^{230}\right)^{0.015}} \quad (2.21)$$

where the Reynolds number is defined by Equation (2.17). Equation (2.21) can be represented graphically as seen in Figure 2.3.

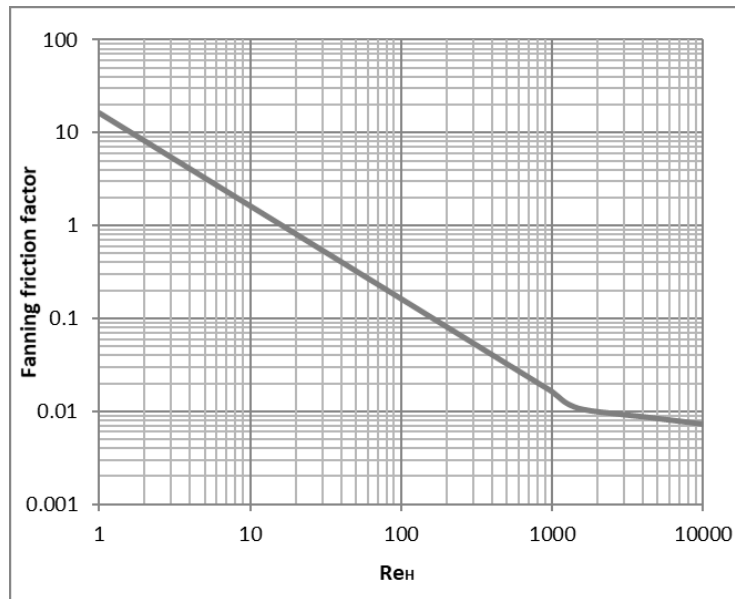


Figure 2.3: Moody diagram showing the relationship between the Fanning friction factor and the Reynold number defined by Equation (2.21), with Re_H defined by Equation (2.17)

2.4 Fluid-particle systems

Thickened tailings are complex clay-water-sand mixtures¹⁷. Ideally, we can divide these mixtures into a non-Newtonian carrier fluid composed of the clay and water and a particle phase composed of the sand particles. To model these mixtures, an understanding of how fluids interact with solid particles within a suspension is critical.

This section starts by describing how a single particle behaves in a fluid. Specifically, the settling under the effect of gravity of a particle through a Newtonian fluid is explained; followed by a summary on recent advances and correlations to describe single-particle settling through non-Newtonian fluids, as this is not fully understood yet. Understanding how a single particle settles through non-Newtonian media acts as a basis to understand

settling of particles in a suspension. This background will be useful in understanding some of the results presented in Chapter 4. Next, multi-particle systems are defined. The hydrodynamics effects for dilute, semi-dilute, and concentrated suspensions are shown, both for Newtonian and non-Newtonian fluids. Other phenomena such as particle migration and sedimentation are shown, as these are prevalent in concentrated suspensions, such as the ones that will be studied in Chapter 4 and 5

2.4.1 Single-particle systems

For a single spherical particle moving in a fluid. The Stokes' law⁵⁵ describes the total drag force resisting slow, steady motion of a particle of diameter d , in a fluid of viscosity, μ :

$$F_D = 3\pi d\mu U \quad (2.22)$$

where U is the relative velocity between the particle and the fluid.

In addition, a single particle Reynolds number, Re_p , and a drag coefficient, C_D , can be defined:

$$Re_p = \frac{U\rho_f d}{\mu_f} \quad (2.23)$$

$$C_D = \frac{\frac{4F_D}{\pi d^2}}{\frac{1}{2}\rho_f U^2} = \frac{24}{Re_p} \quad (2.24)$$

Stokes' law is only valid for $Re_p < 0.3$. At $Re_p > 0.3$ the fluid inertia begins to dominate the motion because of the higher relative velocities. Table 2.1 shows the proposed correlations for the calculation of the drag coefficient based on the particle's Reynolds number.

Table 2.1: Drag coefficient correlations based on the particle's Reynolds number

Region	C_D	Re_p range
Stokes ⁵⁵	$\frac{24}{Re_p}$	$Re_p < 0.3$
Intermediate ⁵⁶	$\frac{24}{Re_p} (1 + 0.15Re_p^{0.687})$	$0.3 < Re_p < 500$
Newton's Law ⁵⁷	~ 0.44	$500 < Re_p < 200000$

i. Drag on a sphere in Newtonian fluids

For a solid sphere falling under gravity through a Newtonian fluid, the force balance can be given as⁵⁷

$$\text{Gravity Force (F}_G\text{)} - \text{Buoyancy Force (F}_B\text{)} - \text{Drag Force (F}_D\text{)} = 0 \quad (2.25)$$

A schematic representation is given by Figure 2.4.

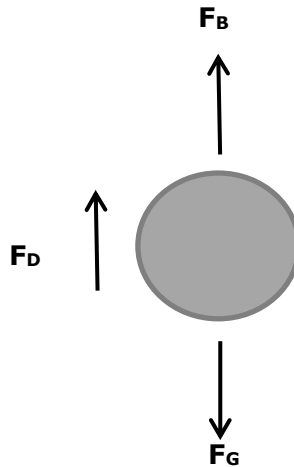


Figure 2.4: Schematic representation of forces acting on a falling solid sphere

For a spherical particle, Equation (2.25) becomes,

$$\frac{\pi d^3}{6} \rho_s g - \frac{\pi d^3}{6} \rho_f g - \frac{1}{2} C_D \rho_f V_\infty^2 \frac{\pi d^2}{4} = 0 \quad (2.26)$$

Thus, the particle settling velocity is given by

$$V_\infty = \sqrt{\frac{4dg(\rho_s - \rho_f)}{3C_D \rho_f}} \quad (2.27)$$

where C_D is the drag coefficient, and can be related to the particle's Reynolds number, Re_p , as shown in Table 2.1

ii. Drag on a sphere in non-Newtonian fluids

In power law fluids, the drag coefficient can be expressed in terms of the Reynolds number and the power law index. For the creeping flow region ($Re \ll 1$), the result can be expressed as a deviation factor $X(n)$, from Stokes' law:

$$C_D = \frac{24}{Re_{PL}} X(n) \quad (2.28)$$

where $X(n)^{58}$ and Re_{PL}^{59} are defined by

$$X(n) = 6^{(n-1)/2} \left(\frac{3}{n^2 + n + 1} \right)^{n+1} \quad (2.29)$$

$$Re_{PL} = \frac{\rho V^{2-n} d^n}{k} \quad (2.30)$$

For $Re_{PL} \leq 500$ the values of drag coefficient are represented by the following equation⁶⁰:

$$C_D = \frac{24}{Re_{PL}} \left(1 + 0.148 Re_{PL}^{\frac{2.35n}{2.42n+0.918}} \right) \quad (2.31)$$

In viscoplastic fluids, a parameter is introduced which describes, for a spherical particle, the static equilibrium between gravity and the yield stress of a fluid⁶¹:

$$Y_G = \frac{\tau_y}{gd(\rho_s - \rho_f)} \quad (2.32)$$

Although this parameter theoretically is intended to provide insight on the balance of forces around a sphere, several studies have reported different Y_G values. For example, Beris et al.⁶² reported $Y_G \sim 1/21$ from their simulation results by solving the equations of motion, which was later confirmed through experiments conducted by Tabuteau et al.⁶³. Other researchers have reported $Y_G \sim 0.2$ based on the assumption that the buoyant weight of a sphere is supported by the vertical component of the force due to the yield stress acting over the sphere surface^{64,65,66}. The discrepancies seem to be related to the yield stress measurement methods and the underlying differences surrounding the way the yield stress has been measured⁶¹.

Once the sphere starts to move the flow field will have a characteristic shape, referred to as a sheared envelope. As the shear stress decreases to a value below the fluid yield stress, the fluid will no longer flow and will behave as an elastic solid. The shape and size of the envelope is dependent on the carrier fluid yield stress, the size and density of the sphere and the relative velocity between the sphere and the fluid⁶¹. Figure 2.5 shows examples of the sheared envelope as depicted by various investigators^{62,67,68}.

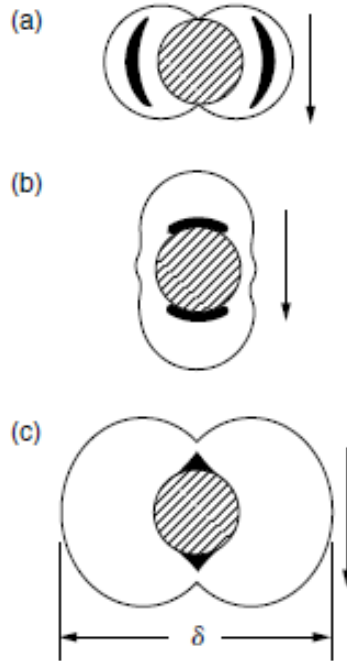


Figure 2.5: Shape of the sheared envelope surrounding a sphere in creeping motion through viscoplastic fluids: (a) Ansley and Smith⁶⁷, (b) Yoshioka et al⁶⁸., (c) Beris et al.⁶² from⁶¹.

For most applications of a settling sphere through a yield stress fluid, correlations are used to determine the drag coefficient (and hence, the terminal settling velocity). An extensive review of the available correlations can be found elsewhere⁶¹. Thus, only methods relevant to the modelling of Chapter 4 will be explained here.

Atapattu et al.⁶⁹ extended the analysis of Ansley and Smith⁶⁷, and developed a method for predicting the drag coefficient from their experimental data using

$$C_D = \frac{24}{Q^*} \quad (2.33)$$

where,

$$Q^* = \frac{Re_{PL}}{1 + \frac{7\pi}{24} Bi_{HB}} \quad (2.34)$$

$$Bi_{HB} = \frac{\tau_y^H}{k \left(\frac{V_\infty}{d}\right)^n} \quad (2.35)$$

While this correlation collapses the data to the Newtonian standard drag curve, it was limited to experiments using Herschel-Bulkley fluids where $0.43 \leq n \leq 0.84$, and $10^{-8} \leq Q^* \leq 0.3$. Consequently, for systems with $Q^* > 0.3$ the error in prediction increases dramatically³⁵.

Wilson et al.⁷⁰ proposed a direct method to calculate the terminal settling velocity of a sphere in a viscoplastic fluid by implementing the pipe flow analysis of Prandtl⁷¹ and Colebrook⁷². Since the shear stress distribution is not uniform around a particle, the characteristic shear stress was defined as the mean surficial stress ($\bar{\tau}$) of a falling particle, relating the immersed weight of the particle to its surface area:

$$\bar{\tau} = \frac{dg(\rho_s - \rho_f)}{6} \quad (2.36)$$

The particle shear velocity is defined as

$$V^* = \sqrt{\frac{\bar{\tau}}{\rho_f}} = \sqrt{\frac{dg(\rho_s - \rho_f)}{6\rho_f}} \quad (2.37)$$

In addition, the shear Reynolds number is defined by

$$Re^* = \frac{d\rho_f V^*}{\mu} \quad (2.38)$$

Wilson et al.⁷⁰ represented the Newtonian drag curve in a V_∞/V^* vs Re^* plot. An apparent viscosity is calculated from the fluid and particle properties and then the terminal settling velocity is calculated for an equivalent case in a Newtonian fluid using the apparent viscosity. A reference point of $0.3\bar{\tau}$ in the fluid rheogram was proposed to determine the proper apparent viscosity from the equivalent Newtonian viscosity. The results from this approach can be seen in Figure 2.6.

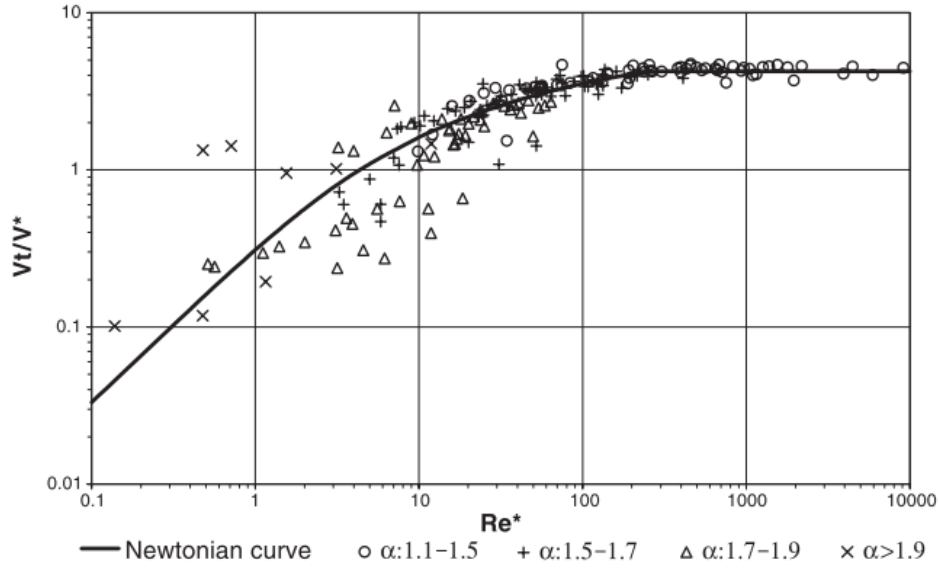


Figure 2.6: Relative fall velocity versus Reynolds number⁷⁰ with $\tau_{ref} = 0.3\bar{\tau}$

While this method works very well for $Re^* > 100$, its predictions seem to deviate noticeably when $Re^* < 100$. In addition, the method is limited for systems where $0.3\bar{\tau} > \tau_y$, since there are no points from the reogram when the reference point is below the yield stress.

In an effort to improve this method, Shokrollahzadeh³⁵ performed high-quality measurements of terminal settling velocities of single spheres in viscoplastic fluids and developed a correlation using the analogy of the Wilson-Thomas model for the turbulent pipe flow of Newtonian fluids⁷³ defined by:

$$\mu_{app} = \begin{cases} \mu_{eq}(4.586\alpha^{12.878}\xi^{1.612}), & \text{for } \alpha < 1.3 \\ \mu_{eq}(5.139\xi^{1.55}e^{(\alpha^{3.995})} + \xi^{2.747} + 0.731), & \text{for } \alpha \geq 1.3 \end{cases} \quad (2.39)$$

where α , for a Bingham Plastic fluid, is given by

$$\alpha_B = 1 + \frac{\tau_y^B}{\bar{\tau}} \quad (2.40)$$

$$\xi = \frac{\tau_y}{\bar{\tau}} \quad (2.41)$$

The results from this correlation can be seen in Figure 2.7. Later in Chapter 4, it will be shown that this correlation can be used in the modelling of a single-particle settling in a non-Newtonian fluid with better accuracy than other correlations.

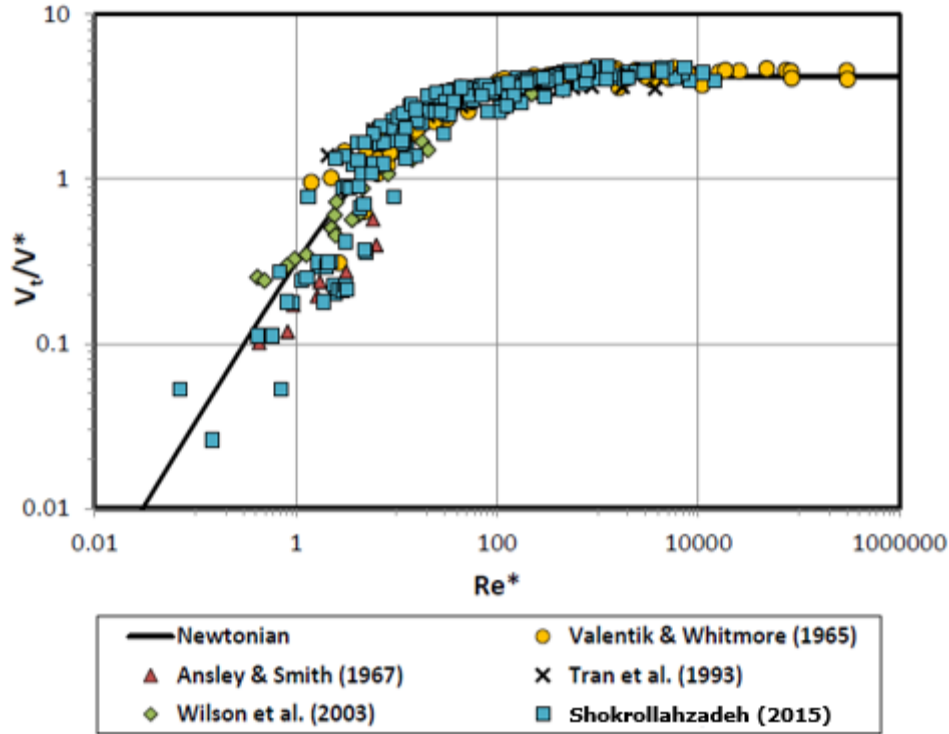


Figure 2.7: Equation (2.39) prediction using experimental data from Valentik and Whitmore⁷⁴, Ansley and Smith⁶⁷, Wilson et al.⁷⁰, Tran et al.⁷⁵, and Shokrollahzadeh³⁵.

2.4.2 Multi-particle systems

In this section, multi-particle systems are described. Specifically, the phenomena resulting from interactions between particles and carrier fluids are considered. These are of importance for the modelling results showed in Chapters 4 and 5.

First, the hydrodynamic effects in Newtonian suspensions are shown, followed by recent studies of non-Newtonian suspensions. Next, particle migration is introduced which is of concern primarily for concentrated suspensions. Finally, sedimentation of particles both in Newtonian and non-Newtonian suspensions is shown.

i. Hydrodynamic effects

When particles are added to a Newtonian fluid, its resistance to flow increases. This behaviour was seen experimentally by Rutgers⁷⁶. The relative viscosity, η_r , is defined by

$$\eta_r = \frac{\eta_s}{\eta_c} \quad (2.42)$$

where η_s is the viscosity of the suspension, and η_c is the viscosity of the carrier fluid. For monodisperse spheres, the relative viscosity is an increasing function of the particle volume fraction. From a physical point of view, solid particles can contribute to the viscosity in two ways: first, the distortion of the flow lines because of the volume occupied by a particle in the fluid and second, the surface roughness of the particle²⁴.

For dilute systems, where the interactions between the particles can be neglected, Einstein proposed the following expression for the relative viscosity⁷⁷

$$\eta_r = 1 + 2.5\phi \quad (2.43)$$

where ϕ is the particle volume fraction.

In semi-dilute systems, where $\phi \sim 0.1$, the distance between the particles cannot be neglected, since the presence of a second particle alters the flow field significantly, which changes the viscosity. The interaction between pairs of particles will be proportional to the square of the volume fraction²⁴:

$$\eta_r = 1 + 2.5\phi + C_2\phi^2 + \dots \quad (2.44)$$

The quadratic coefficient, C_2 , can have different values depending on the particle shape, particle size distribution, and particle surface roughness²⁴.

In concentrated systems, the average distance between particles becomes sufficiently small for lubrication hydrodynamic interactions to dominate the stresses²⁴. Under shear flow, experimental studies of the microstructure has shown the flow field to be anisotropic⁷⁸. In contrast to semi-dilute and dilute systems, the maximum packing concentration, ϕ_{max} , must be taken into account in any calculation involving concentrated suspensions, as flow will cease once this limit is met (i.e. when particles are closely packed). The value of ϕ_{max} depends on particle shape and particle size distribution; for a spherical particle²⁴ $\phi_{max} \sim 0.6$.

Exact predictions of the suspension viscosity do not exist; thus, a number of semi-empirical relations have been proposed, most of which will be used in the modelling of multi-particle systems. For example, Krieger and Dougherty proposed^{25,26}

$$\eta_r = \left(1 - \frac{\phi}{\phi_{max}}\right)^{-[\eta]\phi_{max}} \quad (2.45)$$

where $[\eta]$ is equal to 2.5 for spherical particles. Thomas⁷⁹ proposed the following expression based on experimental data:

$$\eta_r = 1 + 2.5\phi + 10.05\phi^2 + 0.00273e^{(16.6\phi)} \quad (2.46)$$

Morris and Boulay²⁷ proposed the following expression for monodispersed spheres,

$$\eta_r = 1 + 2.5\phi \left(1 - \frac{\phi}{\phi_{max}}\right)^{-1} + K_s \left(\frac{\phi}{\phi_{max}}\right)^2 \left(1 - \frac{\phi}{\phi_{max}}\right)^{-2} \quad (2.47)$$

where K_s is the contact contribution and has a value of 0.1.

In addition, Gillies et al.³² proposed

$$\eta_r = 1 + 2.5\phi + 10\phi^2 + 0.0019e^{(20\phi)} \quad (2.48)$$

based on their experiments of sand particles suspended in a Newtonian fluid.

The effect of particle concentration on the apparent viscosity for non-Newtonian fluids has also been studied. Chakrabandhu and Singh⁸⁰ determined, from their experiments using green peas suspended in a CMC solution, expressions for the relative viscosity, and consistency coefficient for their conditions: specifically, temperatures from 85 to 135 °C, and shear rates from 33 to 247 s⁻¹.

$$\eta_r = 1 + 2.5\phi + 10.05\phi^2 + 20.84\phi^3 \quad (2.49)$$

$$k_r = \frac{k(\phi)}{k(0)} = (1 + 2.5\phi)n_r^{-2} \quad (2.50)$$

where K_r and n_r are the relative consistency coefficient and flow index, respectively.

More recently, Mahaut et al⁸¹., Chateau et al⁸²., and Ovarlez et al⁸³., have studied the effects of coarse, monodispersed, spherical particle concentration on the suspension yield stress and consistency, and have represented the effect as follows:

$$\tau_{yr} = \frac{\tau_y(\phi)}{\tau_y(0)} = \sqrt{\left(1 - \phi\right) \left(1 - \frac{\phi}{\phi_{max}}\right)^{-2.5\phi_{max}}} \quad (2.51)$$

$$k_r = \frac{k(\phi)}{k(0)} = \sqrt{\left(\left(1 - \frac{\phi}{\phi_{max}}\right)^{-2.5(n+1)\phi_{max}}\right) (1 - \phi)^{1-n}} \quad (2.52)$$

Equations 2.51 and 2.52 were developed for 250 μm polystyrene particles suspended in a concentrated emulsion, which was characterized as a Herschel-Bulkley fluid. The flow behaviour of the suspension was evaluated in Couette geometry at shear rates from 0.01 to 80 s^{-1} , with bulk particle volume fractions from 0.1 to 0.5. The equations above provided good agreement when compared with their experiments; however, Ovarlez et al.⁸³ made no comments on their applicability to Bingham plastic fluids or in tube geometries. Despite this, an attempt to use their equations in the modelling conditions of Chapter 5 will be made.

ii. Particle migration

Non-hydrodynamic effects such as interparticle forces can break the particle trajectories causing diffusion and migration²⁴. Furthermore, in concentrated suspensions, the interactions between the particles result in chaotic motion⁸⁴, which generates displacements in various directions. Flow-induced self-diffusion, described as the random motion of a particle in a flow field, was first reported by Eckstein et al⁸⁵.

Shear-induced migration occurs when there are gradients in shear rate. This was shown by Leighton and Acrivos²⁸, where neutrally buoyant particles migrated to toward the cup (outer cylinder) of a coaxial cylinder device during their experiments.

In the work of Phillips et al.³⁰, the migration has been modelled using a local diffusion with a diffusion flux model, and the significant driving forces for particle transport have been reduced into two partial fluxes. The first flux is due to spatially varying interaction frequency; i.e, particles moving from regions of high shear rate to regions of low shear rate:

$$N_c = -K_c \phi a^2 \nabla(\dot{\gamma} \phi) \quad (2.53)$$

The second flux is due to spatially varying viscosity:

$$N_\eta = -K_\eta a^2 \frac{\dot{\gamma} \phi^2}{\eta(\phi)} \nabla(\eta(\phi)) \quad (2.54)$$

where K_c and K_η are proportionality constants and have values of 0.43 and 0.65, respectively³⁰.

Another approach to model migration is to relate the normal stresses or a "normal viscosity" caused by the presence of particles as follows²⁷:

$$\eta_n = K_n \left(\frac{\phi}{\phi_{max}} \right)^2 \left(1 - \frac{\phi}{\phi_{max}} \right)^{-2} \quad (2.55)$$

where K_n is the normal contact contribution and has a value of 0.75.

Shear-induced migration in non-Newtonian fluids has not been studied extensively. Rao et al⁸⁶ extended the Phillips model characterized by equations (2.53) and (2.54), to shear-thinning fluids, which captured many of the trends from their experiments but failed to agree quantitatively.

Ovarlez et al⁸³. were able to predict theoretically shear-induced migration by relating it to the normal stress differences in a concentric-cylinder Couette flow for yield stress fluids. Moreover, the expression they derived is the same as for particles suspended in a Newtonian fluid²⁷, provided the carrier fluids have similar microstructure and the yield stress suspension is sheared in the whole gap of the Couette geometry.

iii. Sedimentation

In concentrated suspensions, the settling of the particles is hindered when compared to the single-particle settling process described in Section 2.4.1. The sedimentation can be described by the empirical expression by Richardson and Zaki³¹.

$$\frac{V_{\infty,s}}{V_{\infty}} = (1 - \phi)^n \quad (2.56)$$

where $V_{\infty,s}$ is the hindered settling rate of the particles, and n is an empirical constant, which is known to be influenced experimentally by wall effects⁸⁷, particle size distribution⁸⁸, and flow regime.

For shear flow, Spelay¹⁷ extended the Phillips model, described by Equations (2.53) and (2.54), to include a sedimentation flux as follows

$$N_s = K_s a^2 \phi f(\phi) \vec{g} \quad (2.57)$$

where

$$K_s = \frac{2(\rho_s - \rho_f)}{9} \quad (2.58)$$

$$f(\phi) = \frac{(1 - \phi)}{\eta_s} \quad (2.59)$$

In addition, Ovarlez et al.⁸⁹ studied the shear-induced sedimentation of monodispersed, glass particles in two yield stress fluids: a concentrated emulsion and Carbopol solution;

using a Couette cell. They determined that shear induces sedimentation in all the studied systems, even in those stable at rest as per Y_G values (defined by Equation 2.32), and it can be modelled by considering that the interstitial fluid behaves like a viscous fluid in the direction orthogonal to the shear. An increase in particle concentration was found to play two roles: hinders settling and, at the same time, it decreases the viscous resistance of the interstitial fluid because of shear concentration between the particles. At the plastic regime (i.e. $Bi_{HB}^{-1} \ll 1$, as defined by Equation 2.35), they proposed a method to predict particle sedimentation, defined by:

$$V(\phi) = \alpha \frac{\Delta \rho g d^2}{\eta[\dot{\gamma}_l(\phi)]} f_{Newtonian}(\phi) \quad (2.60)$$

While Equation (2.60) agrees well with their experimental observations, Ovarlez et al.⁸⁹ pointed out that it would be difficult to compare their experimental results with analytical or numerical studies, because of the poor reproducibility of the concentrated emulsion, and shear rate heterogeneities within the gap of the Couette cell. However, a qualitative analysis, to summarize their results, can be made from Equation (2.60): the sedimentation velocity increases with shear rate and for a given particle diameter and shear rate, the sedimentation velocity is a decreasing function of the fluid yield stress. For a viscoplastic fluid with given rheological properties, the sedimentation velocity is an increasing function of particle diameter. These statements will be useful in testing the model in Chapter 5.

2.5 Numerical modelling

This section provides relevant background for the modelling of viscoplastic fluids, where two main approaches are described, one of which is used during this project. In regard to modelling suspensions, the main challenges are described, along with a review of relevant numerical studies.

2.5.1 Numerical modelling of viscoplastic fluids

The challenge in modelling yield stress fluid flow is to properly represent the plug-like region, where the shear stress is below the yield stress, and to track the surfaces that separate the plug zones from the sheared zones²³. Two approaches have been developed to overcome these challenges. One approach relies on augmented Lagrangian methods to solve the Navier-Stokes equations via an optimization algorithm⁹⁰. The other method regularizes the constitutive law for viscoplastic fluids. For an ideal viscoplastic fluid, the apparent viscosity becomes infinite at the plug region; the method replaces this with a very

viscous fluid. Regularization methods are often the preferred approach because of their simplicity of implementation in commercial CFD packages through user-defined functions⁹¹.

2.5.2 Numerical modelling of coarse particle suspensions

Modelling concentrated suspensions poses numerous challenges as many-body hydrodynamic interactions must be calculated, while also resolving the spatial distribution of the particles in the fluid. Since there is no exact method to predict how the viscosity varies with the presence of particles²⁴, various methods have been applied for approximation of the many-body hydrodynamic interactions. Examples include Stokesian⁹² dynamics, the Lattice Boltzmann⁹³ method, and dissipative particle⁹⁴ dynamics. However, these methods become very limited when the concentration tends towards the maximum packing concentration, since the particles all nearly touch, the time-step required to accurately resolve motion tends to zero⁹⁵. This is usually resolved by adding fictitious surface forces or limitations on the forces acting between the particles²⁴.

Spelay¹⁷ developed a code to model the laminar open-channel flow of negatively-buoyant particles suspended in a viscoplastic fluid, by using the model defined by Equations (2.53), (2.54), and (2.57), and successfully compared it with his experimental data. However, the model is limited to laminar one-dimensional flow of suspensions, and it is not able to predict the sliding bed moving en-bloc.

Most commercial CFD packages rely on the Granular Kinetic Theory (GKT) to account for the behaviour of concentrated coarse particle suspensions. Ekambara et al⁹⁶ studied the horizontal slurry transport under turbulent regime using ANSYS-CFX as the CFD solver, and the GKT model. Their model is able to predict coarse particle concentration profiles in turbulent pipe flow, which they found to be primarily dependent upon the in-situ solids volume fraction. In addition, the model was validated successfully against available experimental data.

Eesa and Barigou⁹⁷ studied the horizontal and vertical flow of coarse nearly-neutrally buoyant particles in power law carrier fluids using ANSYS-CFX and the GKT model. Their model was able to predict the particle phase velocity profile and pressure drop, which were compared against experimental data and available correlations.

Treinen and Jacobs³³ used Ansys Fluent and the GKT model to study particle settling and shear migration in viscoplastics fluids. Three modelling scenarios were considered: quasi-static settling, shear particle migration, and shear settling of particles. Their CFD model predicted quasi-static settling in Newtonian fluids but it was not able to predict the

suspension of particles in viscoplastic fluids. In addition, it was not able to predict the particle migration because of simple shear in Newtonian fluids. However, the model was able to capture the overall behaviour of shear-induced particle settling, but the predictions differ from experimental results; thus, further investigation is needed.

In addition, Sittoni et al³⁴ proposed a 2DV (two dimensional vertical) numerical module, Delft3D slurry, which solves the horizontal momentum equations of an incompressible fluid flowing with a mobile air-water surface; they considered the water-mud-sand mixture as a quasi-single phase fluid of which their summed or total momentum equations are solved rather than the momentum equations per sediment fraction. The authors showed some promising preliminary results but their model requires further validation.

2.6 STAR-CCM+: Overview

STAR-CCM+ is the commercial CFD package used in this study. This section provides an overview of its meshing capabilities, multiphase models, suspensions modelling, non-Newtonian fluids modelling, and other terminology necessary to understand the results shown in the following Chapters. The software is used for solving multidisciplinary problems in fluid and solid continuum mechanics, with a current version of v12.04 released in 2017. It employs a client-server architecture which allows the users to solve problems using a regular computer while all the costly calculation is done in a remote server⁹⁸. As commercial software, the source code is closed and proprietary; thus, users cannot modify or see the code.

2.6.1 Meshing capabilities

For three-dimensional cases, STAR-CCM+ offers a variety of built-in approaches for mesh generation:

- Core meshers: trimmer, polyhedral, tetrahedral, and prism layer mesher.
- Specialized meshers: thin part mesher, generalized cylinder mesher, extruder mesher, and offset mesher.
- Directed mesher for swept CAD geometries

The prism layer and directed mesher will be explained in more detailed as these are the ones used in this project.

i. Prism layer mesher

The prism layer mesher is used in conjunction with other meshing techniques to generate cells that are orthogonal to the wall surfaces or boundaries, which allows the CFD solver to resolve near-wall flow more accurately, as well as flow features such as separation which can affect drag or pressure drop results. The layers are characterized by their thickness, number of cell layers, and size distribution; these features can be modified accordingly to the needs of the user⁹⁸, as shown in Figure 2.8.

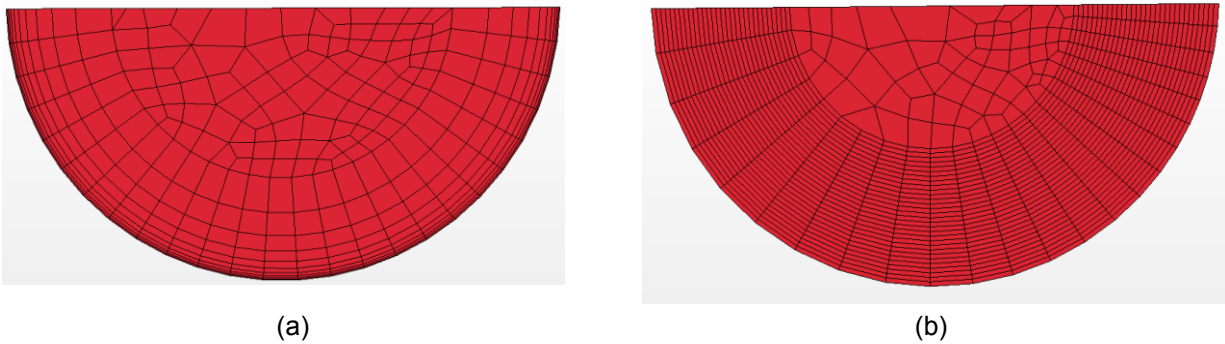


Figure 2.8: Prism layer mesher example, with (a) Progressive layer stretching and (b) Constant stretching

ii. Directed Meshing

The directed meshing technique is used to create a surface mesh and sweep it in a given direction of the CAD geometry through its volume. This allows for stretching and control over the mesh resolution in the direction where large gradients of the flow variables are not expected⁹⁸.

The surfaces of the geometry can be divided in the following categories for direct meshing:

- Source surface, where the surface mesh is initially generated
- Target surface, where the meshing ends
- Guide surface, alongside which the surface mesh is swept from the source surface to the target surface

A graphical representation of the categories can be seen in Figure 2.9.

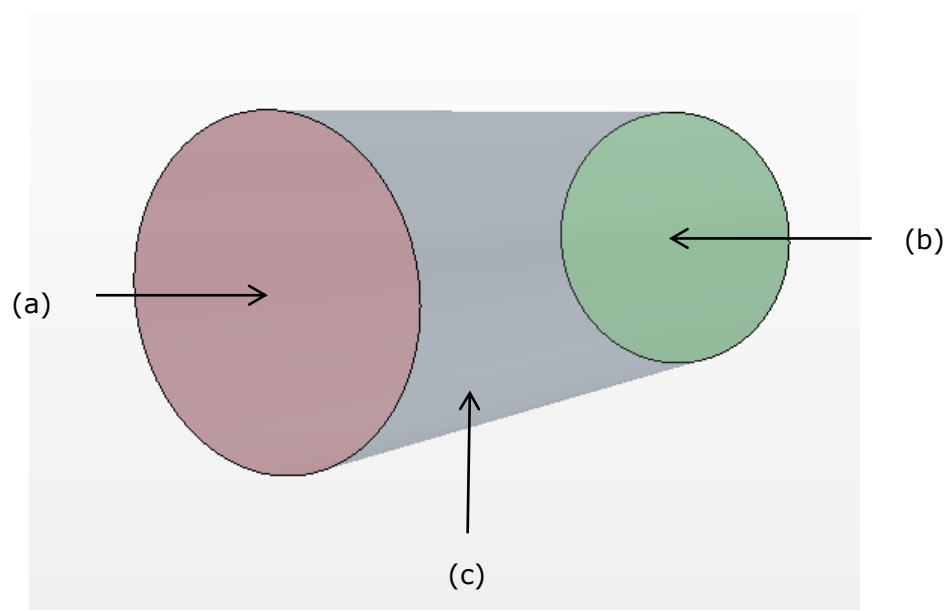


Figure 2.9: (a) Source, (b) target, and (c) guide surfaces for directed meshing

The source surface mesh is related with a volume mesh distribution which is used to generate the final volume mesh, which can be seen in Figure 2.10.

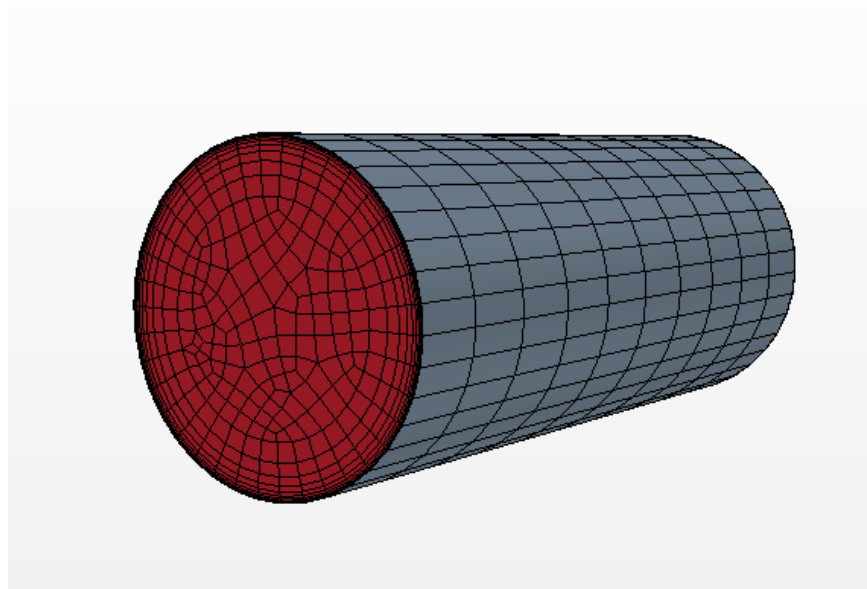


Figure 2.10: Directed mesh example

2.6.2 Multiphase flow modelling

STAR-CCM+ provides the following modelling approaches for multiphase flows. Only the following approaches used in this project are explained in more detail:

- Volume of Fluid model (VOF)
- Multiphase Segregated Flow model (also referred to as Eulerian-Eulerian, Euler-Euler, EMP)
- Lagrangian Multiphase model
- Fluid Film model
- Discrete Element Model (DEM)
- Eulerian Multiphase Mixture model
- Dispersed Multiphase model (DMP)

The Volume of Fluid, Multiphase Segregated Flow, and the Eulerian Multiphase Mixture models share a common Eulerian framework; in other words, they are all defined as Eulerian multiphase models within STAR-CCM+.

i. Volume of Fluid (VOF) Model

This model is suited for simulations of two immiscible fluids with a distinct interface, or free surface flows. The spatial distribution of each phase is given by the volume fraction. The model assumes that all phases share velocity, pressure and temperature fields, meaning that the same set of governing transport equations for energy, mass, and momentum of a single-phase flow can be solved. The interface is tracked using the High-Resolution Interface Capturing (HRIC) which is designed to mimic the convective transport of the fluids. The physical properties of the phases as well as their volume fractions are used to solve the equations for an equivalent fluid⁹⁸, as follows:

$$\rho = \sum_i \rho_i \phi_i \quad (2.61)$$

$$\mu = \sum_i \mu_i \phi_i \quad (2.62)$$

Where

$$\phi_i = \frac{V_i}{V} \quad (2.63)$$

is the volume fraction and ρ_i , μ_i are the density and dynamic viscosity of the i^{th} phase.

Thus, the conservation equation for the transport of volume fraction ϕ_i is:

$$\frac{d}{dt} \int_V \phi_i dV + \int_S \phi_i (\mathbf{v} - \mathbf{v}_g) \cdot d\mathbf{a} = \int_V \left(S_{\phi_i} - \frac{\phi_i D\rho_i}{\rho_i Dt} \right) dV \quad (2.64)$$

ii. *Multiphase Segregated Flow model*

This model is based on an Eulerian-Eulerian formulation where the conservation equations are solved for each distinct phase; the pressure equation is shared by all phases, while the volume fraction gives the share of the flow domain each phase occupies. The model uses a SIMPLE-type (Semi-Implicit Method for Pressure Linked Equations) approach as a solution algorithm, which has separate pressure and velocity solvers⁹⁸.

The conservation of momentum is given by

$$\begin{aligned} \frac{\partial}{\partial t} \int_V \phi_i \rho_i \chi \mathbf{V}_i dV + \oint_A \phi_i \rho_i \chi \mathbf{V}_i \otimes (\mathbf{V}_i - \mathbf{V}_g) \cdot d\mathbf{a} \\ = - \int_V \phi_i \chi \nabla p dV + \int_V \phi_i \rho_i \chi \mathbf{g} dV + \oint_A [\phi_i (\tau_i + \tau_i^t)] \chi \cdot d\mathbf{a} + \int_V \mathbf{M}_i \chi dV \\ + \int_V (\mathbf{F}_{int})_i \chi dV + \int_V s_i^V dV + \int_V \sum_{j \neq i} (m_{ij} \mathbf{V}_j - m_{ji} \mathbf{V}_i) \chi dV \end{aligned} \quad (2.65)$$

And, the conservation of mass is given by

$$\frac{\partial}{\partial t} \int_V \phi_i \rho_i \chi dV + \oint_A \phi_i \rho_i \chi (\mathbf{V}_i - \mathbf{V}_g) \cdot d\mathbf{a} = \int_V \sum_{j \neq i} (m_{ij} - m_{ji}) \chi dV + \int_V s_i^\alpha dV \quad (2.66)$$

The topology and physics of the interface between two phases are defined by phase interactions in STAR-CCM+, each one identifies which phases interact, the interface topology, models for the interface length, and interphase transfers⁹⁸.

For multiphase segregated flows, these phase interactions are available:

- Granular Particle Pair, used to define the interaction between two particle phases.
- Continuous-Dispersed, used to define a phase that is dispersed in a continuous phase.
- Large Scale Interface (LSI), used for stratified two-phase flow with a dispersed two-phase flow.

The Continuous-Dispersed phase interactions are of interest for this investigation. When selecting the Continuous-Dispersed phase interaction the following models are automatically selected:

- Drag force, modelled as a linear multiplier of the relative velocity between two phases
- Interaction Length Scale, defined as the mean particle size, is used to calculate Reynolds number and interaction area density
- Interaction Area Density, specifies the interfacial area available for drag, and mass transfers between phases

Also, when the continuous phase is a liquid and the dispersed phase is a bubble or a solid particle, the suspension rheology model can be activated as additional modelling for the phase interactions. As pointed out earlier, the presence of particles suspended in a liquid has a strong effect on the mixture viscosity. STAR-CCM+ provides the following built-in models for the relative viscosity: Krieger-Dougherty Model, defined by Equation (2.45); and the Morris and Boulay model, defined by Equation (2.47). The normal viscosity can be modelled using Equation (2.55). Also, the following interface transfer models available:

- Lift force, used to model the perpendicular lift force that a particle can experience in a non-uniform flow field
- Wall lubrication force, used to model the force that a rising bubble experiences that prevents it from touching the wall
- Turbulent dispersion force, used to model the interaction between the dispersed phase and the turbulent eddies
- Virtual mass force, used to model an additional resistance that a particle experiences accelerating through a fluid

iii. Lagrangian multiphase model

The Lagrangian model is designed to track the path of particles dispersed in a continuous phase. In a Lagrangian frame, the conservation equations are solved for each individual particle, which allows the user to calculate the trajectory of each particle. On the other hand, the governing equations for the continuous phase are solved in an Eulerian frame taking into account the dispersed phase⁹⁸.

The interaction between the dispersed phase and the continuous phase can be modelled as one-way coupling or two-way-coupling. In one-way coupling, the continuous phase

influences the dispersed phase but not the other way around. In two-way coupling the continuous phase and the dispersed phase influence each other⁹⁸.

The momentum conservation equation for a particle in a Lagrangian framework is given by

$$m_p \frac{d\mathbf{v}_p}{dt} = \mathbf{F}_s + \mathbf{F}_b \quad (2.67)$$

where \mathbf{F}_s denotes the surface forces action on the particle and \mathbf{F}_b represents the body forces. Particles are introduced to the flow domain through discrete injectors, which define the size and velocity of the particles.

2.6.3 Non-Newtonian flow modelling

Non-Newtonian fluids can be modelled in STAR-CCM+ using built-in models or user-defined functions. Specifically, the non-Newtonian Generalized Power Law model uses the regularization method, described in Section 2.5.1: at the plug region, the viscosity of the mixture is modelled as a very high viscosity fluid; at the sheared region, the viscosity of the mixture varies with shear rate. The formulation of the model is described by

$$\mu(\dot{\gamma}) = \begin{cases} a_T * \mu_0 & , \dot{\gamma} < \frac{\tau_y}{\mu_0} \\ a_T * \frac{\tau_y + k \left[a_T \left(\dot{\gamma} - \frac{\tau_y}{\mu_0} \right) \right]^n}{a_T \dot{\gamma}} & , \dot{\gamma} > \frac{\tau_y}{\mu_0} \end{cases} \quad (2.68)$$

where a_T is a temperature factor and μ_0 is the yielding viscosity, which is the value of dynamic viscosity the solver uses at the plug region.

2.6.4 Solution Analysis

Simulation data can be accessed through field functions in STAR-CCM+, while the simulation is running and when it is completed. The following strategies can be used to analyze the data:

- Reports, which can be created for specific quantities and can be monitored while the simulation is running.
- Scenes, which allow for dynamic viewing of a running simulation or converged solution
- Plots, which can be created using sets of data from the solution

Regardless of the chosen strategy, the parts that represent the actual size and shape of the physical space from which the solution is extracted must be selected:

- Regions, which represent a volume in 3D that is based on the geometry and where the CFD simulation is conducted
- Boundaries, which represent the exterior of regions. They could be a physical boundary or a connection between faces
- Derived parts, which are additional lines and surfaces additional to geometry parts and regions. For example, Figure 2.11 shows a plane that represents a cross section of the geometry and a vertical centerline; these parts can be used to visualize and study the solution inside the cylindrical geometry

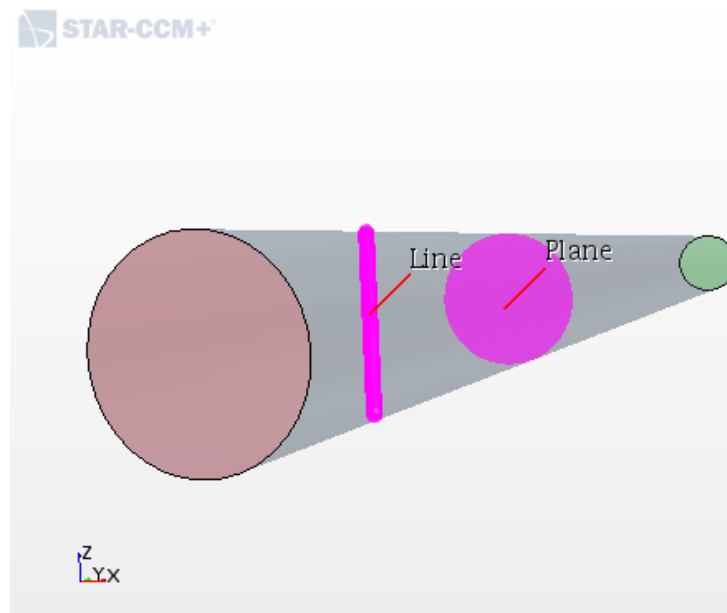


Figure 2.11: Example of derived parts created using STAR-CCM+: a plane and a vertical centerline inside a cylinder

3. Homogeneous, laminar, open-channel flow of non-Newtonian fluids

This study relates to the discharge of the tailings into a dedicated disposal area (DDA) where tailings flow in sheets or in open channels^{16,17}, with different shapes. The geometries, semi-circular and rectangular, are idealized with respect how these mixtures might flow once they have been disposed. As mentioned in Chapter 2, thickened tailings can be divided into a suspension with two main components or phases: a carrier fluid, represented by the clay-water, considered to be homogeneous, and sand particles as the coarse solid phase. The focus of this chapter is on the behaviour of homogeneous clay-water mixtures to establish the foundations for subsequent modelling. To characterize this type of flow, the ability of the model to predict depth of flow, velocity profile, and wall shear stress of homogeneous non-Newtonian fluids is tested.

First, relevant details of the experimental setup, with which the experimental data was obtained. Next, details about modelling with the STAR-CCM+ commercial software, such as meshing, models, solver parameters, and boundary conditions are shown. The model is validated using published data, with a total of 16 experimental conditions considered.

3.1 Semi-circular channel

For the semi-circular channel simulations, the experimental data from Splay¹⁷ were used for validation of the CFD model. His experimental study involved various clay-water and clay-water-sand mixtures tested in a semi-circular flume, whose radius was 78 mm and was 18.5 m in length. Flume angles from 2 to 6°, mixture flow rates from 0.24 to 6.40 L/s, and mixture Bingham yield stress values from 0 to 40 Pa were tested experimentally. A schematic of the flume and recirculating loop used during the experiments is shown as Figure 3.1

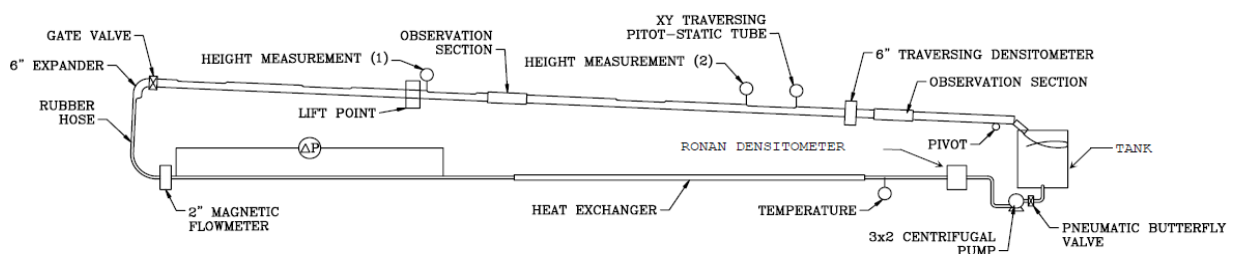


Figure 3.1: Saskatchewan Research Council's 156.7 mm flume circuit used by Splay¹⁷

i. Geometry and meshing

The geometry was designed to match the setup by Spelay¹⁷ shown in Figure 3.1. The semi-circular channel has a diameter of 105.7 mm and is 18.5 m in length. Preliminary simulations using trimmed, polyhedral, and directed meshing techniques showed a variation of less than 10% for the depth of flow prediction. However, as mentioned in Section 2.6.1 directed meshing is recommended for cases where the flow variables do not change significantly in the direction of the flow⁹⁸. This allowed for a mesh structure that had half the numbers of cells, resulting in faster computation times, when compared with other techniques. The mesh structure for the semi-circular channel, shown as Figure 3.2, has 22000 cells. The mesh is finer for cells orthogonal to the channel walls for better resolution of flow variables near the wall, the bottom portion of the channel inlet represents where the mixture is introduced to the flow domain and its size depends on the calculated depth of flow using the experimental flow rate for each case.

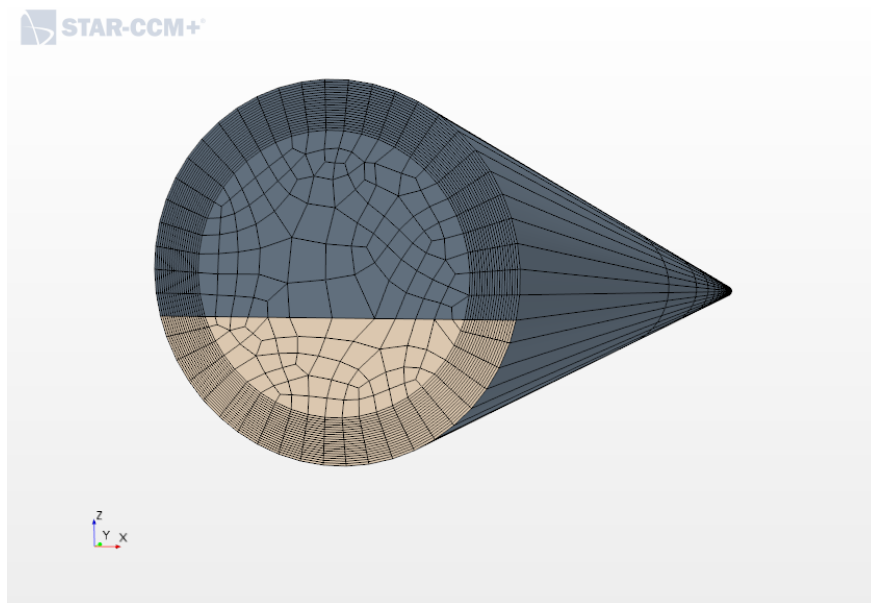


Figure 3.2: Mesh structure for the semi-circular channel simulations

ii. Physics models

The main STAR-CCM+ models (as defined in Section 2.6.2) used to describe the physics of the problem are shown in Table 3.1

Table 3.1: STAR-CCM+ models used on the semi-circular channel simulations

Category	STAR-CCM+ model
Space	Three dimensional
Time	Implicit Unsteady (1 st -order upwind)
Material	Eulerian Multiphase
Eulerian Multiphase Model	Volume of Fluid (VOF) (2 nd -order upwind)
	Multiphase Equation of State
	Multiphase Interaction
Viscous regime	Laminar
Temperature	Isothermal
Density	Constant
Liquid phase viscosity	Non-Newtonian Generalized Power Law
Drag force	Schiller-Neumann
Other	Gravity

iii. Solver parameters, stability and convergence

The convective Courant-Friedrichs-Lewy (CFL) number is defined as the ratio of the physical time-step to the mesh convection time scale:

$$\sigma = \frac{V\Delta t}{\Delta x} \quad (3.1)$$

For free surface flow applications, the convective CFL number is recommended to be less than 0.5 in all cells⁹⁸. If the free surface moves more than half a cell per time-step, it can lead to divergence of the solver. Thus, the time-step was chosen to satisfy this requirement in all simulation cases. Figure 3.3 shows how the maximum CLF number varied with time for Case 1A during the simulations in this case, the time-step was set to 0.001 s to maintain the CFL number between 0.3 and 0.5 for up to 50 s of solution time throughout the flow domain.

The under-relaxation factor, a parameter that governs the extent to which the new solution supplants the old solution at each iteration, was set to 0.7 by default for the velocity and volume fraction solvers, and 0.2 for the Pressure solver.

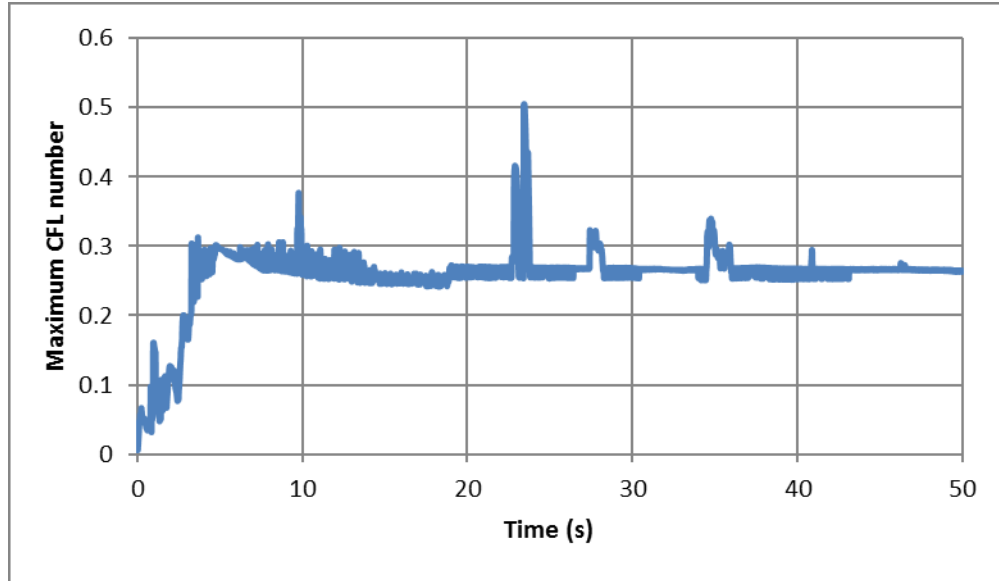


Figure 3.3: Maximum CFL number monitor extracted from STAR-CCM+ for Case 1A

iv. Boundary conditions and solution analysis

Three types of flow boundaries were used for the simulations:

- Mass flow inlet: specifies mass flow rate or mass flux per phase
- Flow-split outlet: specifies a split ratio or mass flux
- Wall: specifies the no-slip condition

During the simulations, the maximum convective CFL number and maximum velocity of the free surface were monitored. The solution was visualized using scalar scenes and plots of the volume fraction of the mixture, wall shear stress, and velocity magnitude. In addition to the monitored quantities mentioned above, the residuals were monitored as another way of ensuring a converged solution. In general, a good indication of convergence is when the residuals drop by about three orders of magnitude⁹⁸, Figure 3.4 shows a typical example of the residuals (for Case 4A), where the residuals dropped by three orders of magnitude in about 1000 iterations. Also, after 20,000 iterations the residuals do not change significantly, which is another indication of convergence.

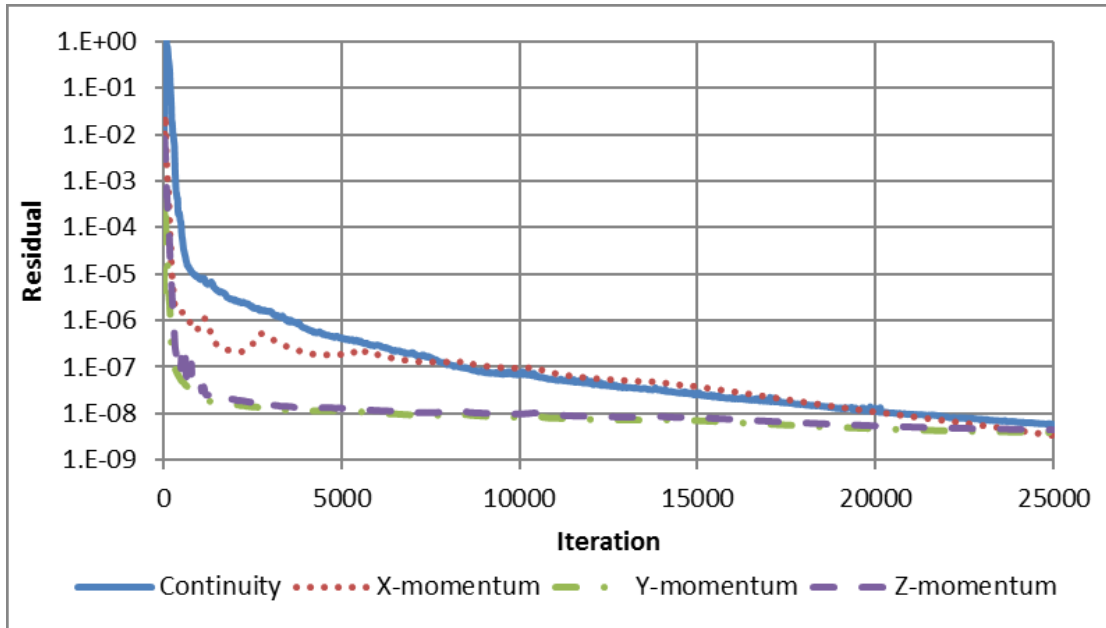


Figure 3.4: Example of residuals plot for Case 4A

3.1.1 Model validation

The results are presented in three main categories: depth of flow prediction, wall shear stress prediction, and velocity profile prediction. The properties of two of the non-Newtonian, homogeneous mixtures evaluated by Spelay¹⁷ are shown in Table 3.2. These mixtures were tested over a wide range of experimental conditions. For the modelling, a representative data set, based on the Reynolds number for non-Newtonian fluids, (proposed by Haldenwang et al.⁵¹ and presented here as Equation 2.15) was selected; these conditions are shown in Table 3.3, the flow rate values were used as boundary conditions. Each simulation was run for at least for two residence times to ensure development of the flow solution.

Table 3.2: Rheological properties of the mixtures modelled in this study¹⁷

Mixture	Density (kg/m ³)	τ_y (Pa)	k (Pa.s ⁿ)	Power Law Exponent, n
1	1375	34.1	0.0305	1.0
2	1384	7	0.0125	1.0

Table 3.3: Experimental conditions considered for modelling in the semi-circular channel reported by Spelay¹⁷

Case*	Q (L/s)	\bar{v} (m/s)	Slope (°)	h ₁ (m)	h ₂ (m)	τ_w (Pa)	Re _H (Eq. 2.17)
1A	5.96	0.71	4.5	0.0709	0.0700	39.2	156
1B	3.03	0.40	4.5	0.0647	0.0655	36.1	50
1C	1.27	0.19	4.5	0.0586	0.0592	33.6	12
1D	3.95	0.57	5	0.0607	0.0608	38.4	104
1E	2.02	0.42	6	0.0467	0.0461	37.7	57
2A	2.04	1.67	6	0.0186	0.0172	16.2	2835
2B	3.00	2.12	6	0.0234	0.0207	16.7	4481
2C	2.50	1.08	3	0.0307	0.0255	13.1	1582
2D	2.48	0.78	2	0.038	0.0319	11.1	916
2E	1.54	0.82	3	0.0257	0.0226	11.4	935
2F	2.00	0.66	2	0.0364	0.0310	10.8	669
2G	3.01	1.23	3	0.0322	0.0264	13.3	1984

*Numbers 1 and 2 represent the mixture that was used

i. Depth of flow prediction

For the semi-circular channel, Spelay¹⁷ reported depth of flow measurements 7.5 and 13.3 m away from the channel inlet. Consequently, planes were created at these positions for the simulations; the value for the depth of flow was selected as the position where the volume fraction of the mixture was 0.5 at the centerline. An example of a scalar scene is shown as Figure 3.5, which shows the volume fraction distribution of the mixture on a plane perpendicular to the flow direction; the color blue, occupying most of the upper part of the channel, represents a mixture volume fraction of 0, whereas the color red, occupying the bottom part of the channel, represents a mixture volume fraction of 1.0. In addition, a parity plot between the simulation results and the experiments for the mixtures can be seen in Figure 3.6.

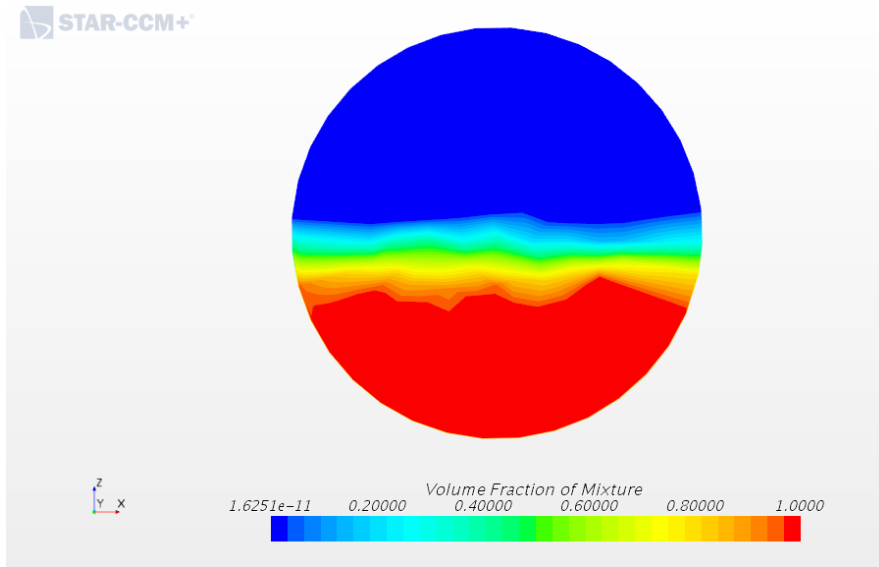


Figure 3.5: Contour plot of the volume fraction of mixture for case 1A in a plane perpendicular to the flow direction

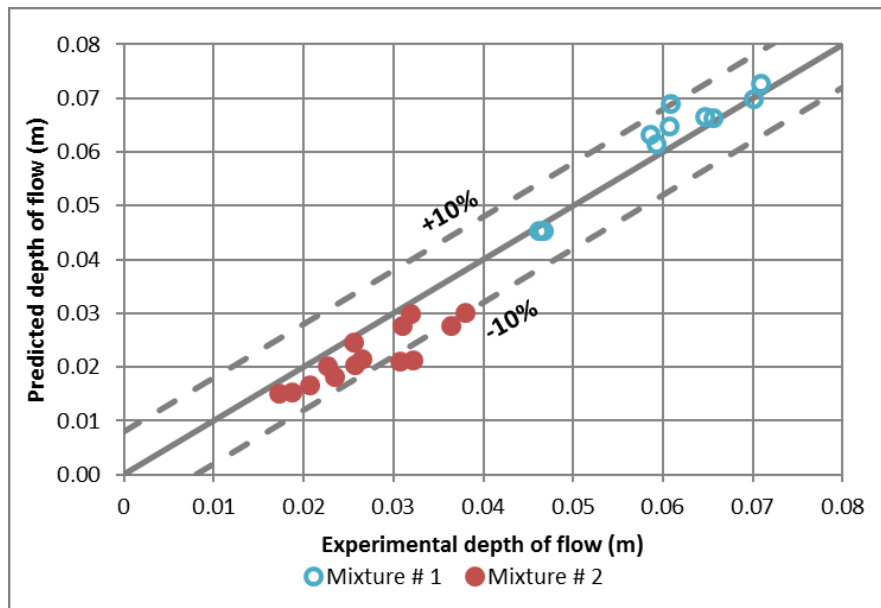


Figure 3.6: Parity plot for experimental and predicted depth of flow for the conditions shown in Table 3.3.

In Figure 3.6, the parity line (solid line) represents a perfect match between experiments and simulations, while the dashed lines represent $\pm 10\%$ of deviation from the parity line as this was the error percentage reported by Spelay¹⁷ for the depth of flow measurements in his study. Only 3 out of 24 data points are outside this limit, which indicates good

agreement between experiments and simulations results. However, there is a trend towards the prediction of lower depths of flow than what experimentally measured for Mixture # 2. This is associated with the higher average velocities, with $669 < Re_H < 4481$, which contribute to the differences between experiments and predictions for that mixture, because inertial effects can play a dominant role, causing rippled or wavy surfaces, which were not considered for the modelling.

In addition, if the data of Figure 3.6 were redistributed using the plane on which they were measured, as shown in Figure 3.7, it can be seen that there is more scatter when the measurement was taken 7.5 m (Plane 1) away from the channel inlet when compared to the measurements made 13.3 m (Plane 2) away from the inlet, regardless of the mixture properties. This suggests the flow length of 7.5 m is not sufficient to achieve a steady value of depth of flow for the range of conditions that were tested experimentally. Thus, subsequent analysis will be made 13.3 m away from the channel inlet.

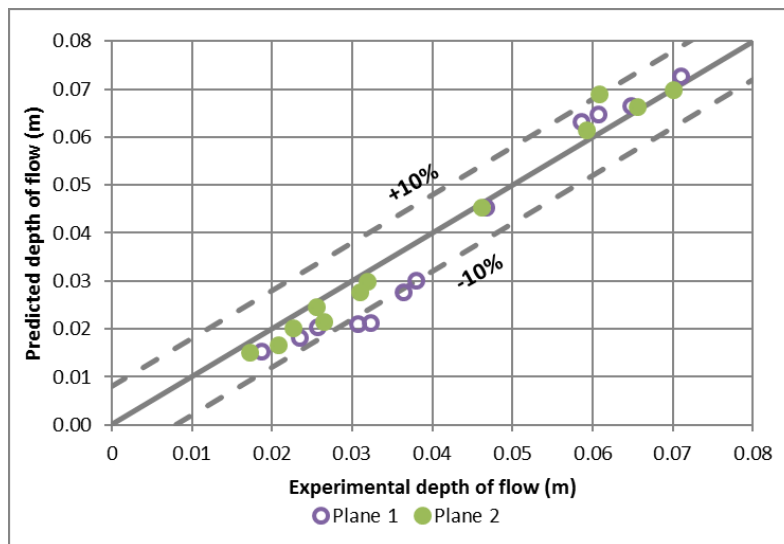


Figure 3.7: Parity plot for experimental and predicted depth of flow for the conditions shown in Table 3.3.

While experimental uncertainties can influence the discrepancies between experiments and simulation results, the modelling assumptions must be considered as well. Because there was no information of the inlet depth of flow required for modelling, it was calculated for these simulations using the experimental flow rate for each case in Table 3.3. Another modelling assumption is the fact that, as mentioned in Chapter 2, all phases share the velocity field when using the VOF model, namely, it does not allow for a no-shear specification at the interface between the gas phase and liquid phase.

ii. Wall shear stress and friction losses prediction

The wall shear stress was visualized through scalar scenes, Figure 3.8 shows an example for the conditions of Case 2B, where the highest wall shear stress, of around 51.4 Pa, is found close to the inlet of the channel, suggesting entry effects. As the distance from the inlet increases, the distribution of the wall shear stress at the bottom of the channel becomes more uniform, suggesting a developed flow. The simulation results for the average wall shear stress, when the flow was fully developed, were compared to those reported by Spelay¹⁷ in a parity plot, shown as Figure 3.9

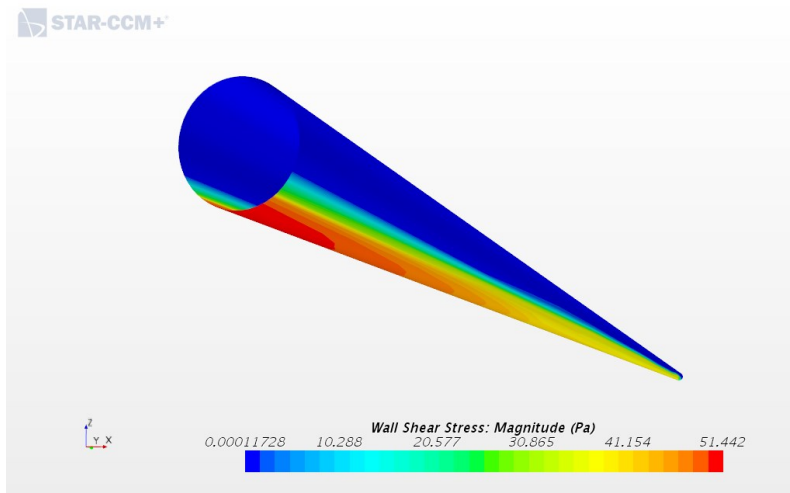


Figure 3.8: Wall stress distribution for Case 2B (experimental conditions shown in Table 3.3)

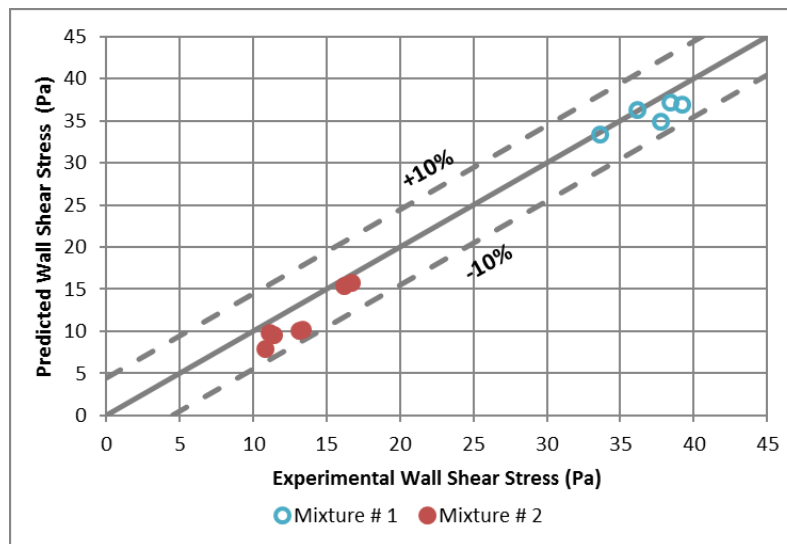


Figure 3.9: Parity plot for experimental and predicted wall shear stress for the conditions shown in Table 3.3.

From Figure 3.9, it can be seen that all points corresponding to predicted and experimental wall shear stress are within $\pm 10\%$ of the parity line, which is the error reported by Spelay¹⁷ for the wall shear stress calculations in his study. In contrast with the results in Figure 3.6, there is no over-prediction of the values for the wall shear stress and there are no clear distinctions between the mixtures.

iii. Average velocity and velocity profiles prediction

The comparison of predicted and measured average velocity values for the cases in Table 3.3 is shown as Figure 3.10. The predicted average velocity was extracted from a plane 13.3 m away from the channel inlet. Only the cells where the mixture volume fraction was between 0.5 and 1.0 were considered.

The prediction of the average velocity at a given location is tied to the depth of flow prediction through the conservation of mass equation. Thus, as expected, the predicted values for Mixture # 2 seem to deviate more from the parity line compared to those of Mixture # 1. Spelay¹⁷ reported a 4% error in the measurements of the average velocity, using this criterion, 3 data points can be rejected from Figure 3.10, while the rest shows good agreement between experiments and simulation results.

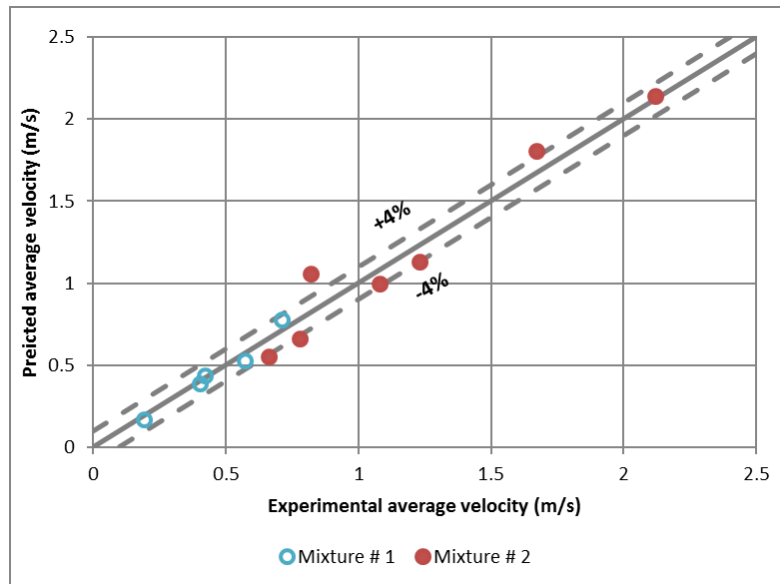


Figure 3.10: Parity plot for experimental and predicted average velocity for the conditions shown in Table 3.3.

Spelay¹⁷ also measured local mixture velocities with a Pitot tube. From the cases in Table 3.3, there were data available for local velocities only for cases 2A, 2B, and 2B, because the

high apparent mixture viscosity for some of the conditions made it difficult to obtain meaningful Pitot tube measurements¹⁷. The comparison of measured velocity profiles and those obtained from simulations is shown in Figures 3.11 to 3.13.

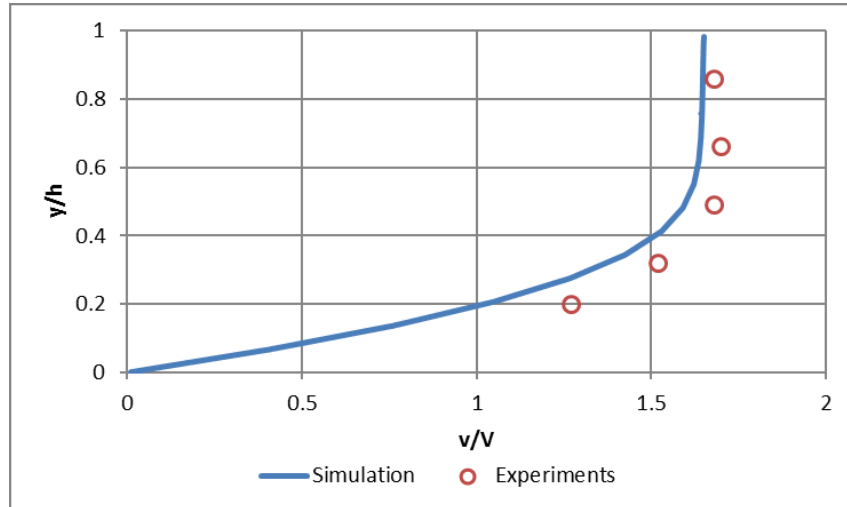


Figure 3.11: Normalized centerline velocity profile comparison between experiments by Splay and simulation results for Case 2A.

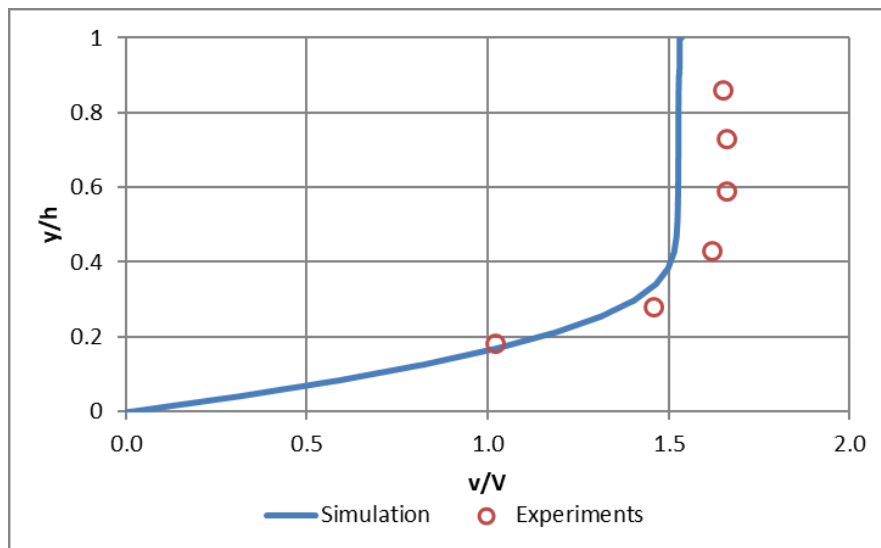


Figure 3.12: Normalized centerline velocity profile comparison between experiments by Splay and simulation results for Case 2B.

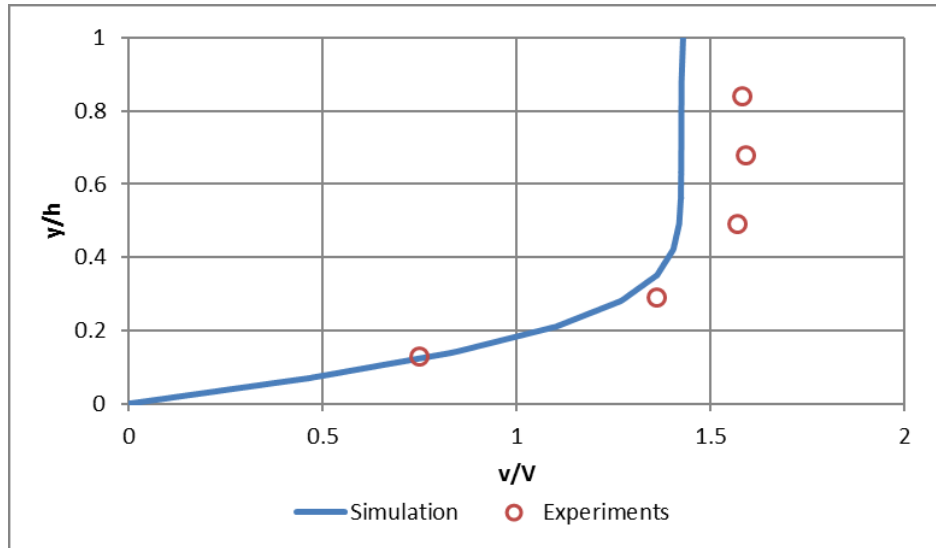


Figure 3.13: Normalized centerline velocity profile comparison between experiments by Spelay and simulation results for Case 2G.

Figures 3.11 to 3.13 represent normalized plots of the velocity profiles. On the Y-axis, the vertical position is normalized using the depth of flow; thus, a value of $y/h = 1.0$ represents the location of the free surface. On the X-axis, the local velocity is normalized using the average velocity. It can be seen that the CFD model can predict the expected trend of the velocity profiles for a viscoplastic fluid; namely, the velocity is zero at the wall and increases until it reaches a plug zone, where the shear stress is equal to the yield stress, and the velocity becomes constant. The prediction for the conditions from Case 2A was in good agreement with the experimental results. However, while more discrepancies were observed for the conditions in Cases 2B and 2G, they are less than 10% of difference with respect of the experiments. These discrepancies can be associated to various reasons: experimental uncertainties, such as depth of flow measurements; Reynolds numbers near transition-turbulence, as shown in Table 3.3 Cases 2A, 2B and 2G were evaluated under $Re_H > 1984$ conditions, while only laminar effects were considered in the modelling; and the absence of a correlation in the literature that could account for the yield stress effect on the Pitot tube measurements, for low Reynolds numbers. Spelay et al.⁹⁹ assumed a Newtonian fluid of equivalent apparent viscosity to account for this effect. To further analyze the velocity field predictions, experiments from other researchers who measured the local mixtures velocities using a different method are modelled in Section 3.2. This could provide more clarity on the roots of the discrepancies between the experiments and simulations.

iv. Friction losses

As described in Section 2.3.1, Burger et al.⁵³ proposed a correlation to predict the Fanning friction factor using the Reynolds number for non-Newtonian fluids, and different channel geometries. Specifically, for a semi-circular channel, the correlation is presented here as Equation 2.20

$$f = 0.048Re^{-0.2049} + \frac{(16.2Re^{-1} - 0.048Re^{-0.2049})}{\left(1 + \left(\frac{Re}{1055}\right)^{230}\right)^{0.015}} \quad (2.20)$$

In addition, as a reminder, the Fanning friction factor and the non-Newtonian Reynolds number are given by

$$f = \frac{2\tau_w}{\rho\bar{V}^2} = \frac{2R_h g \sin \theta}{\bar{V}^2} \quad (2.16)$$

$$Re_H = \frac{8\rho V^2}{\tau_y + k\left(\frac{2V}{R_h}\right)^n} \quad (2.15)$$

The simulation results were used to calculate the Reynolds numbers and the friction factors, described by Equations 2.15 and 2.16, and then compared against Equation 2.20, shown as a Moody diagram in Figure 3.14.

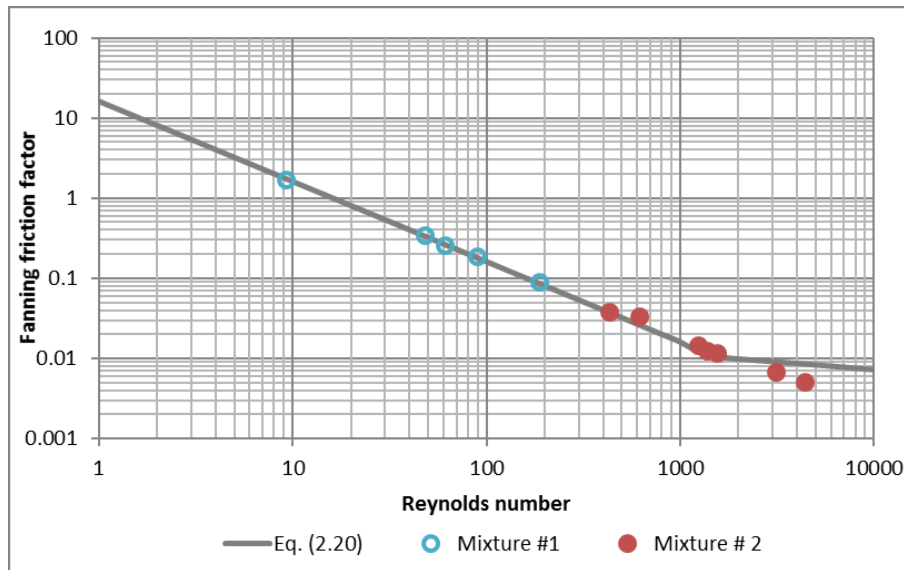


Figure 3.14: Comparison of the simulation results and Fanning friction factor correlation by Burger et al.⁵³

From Figure 3.14, it can be seen that when $Re_H < 2000$, there is close agreement between simulations and the predictions of Eq. (2.20). This range covers the laminar flow regime ($Re_H \leq 1000$), and transition regimes ($1000 < Re_H \leq 2000$). For $Re_H > 2000$, there is poorer agreement between the simulation results and the predictions of Eq. (2.20), because inertial effects were not considered during the modelling. This comparison helps to further validate the model for $Re_H < 2000$ values.

3.2 Rectangular channel

As discussed before, the purpose of these simulations is to study the uncertainties seen in the velocity profile predictions for Cases 2A, 2B, and 2G. Specifically, the role of inertial effects at high Reynolds numbers and the assumptions made to measure the local velocity using a Pitot tube, are studied. To address this, the laminar experimental conditions of Haldenwang et al.⁴⁵ were modelled. They used an Ultrasonic Velocity Profiling (UVP) system to measure the local mixture velocity and the laminar sheet flow model proposed by De Kee et al.⁴⁴ to study the flow of Power Law and Bingham Plastic fluids in a rectangular flume, which was 300 mm in width and 10 m in length. A schematic representation of their setup is shown as Figure 3.15.

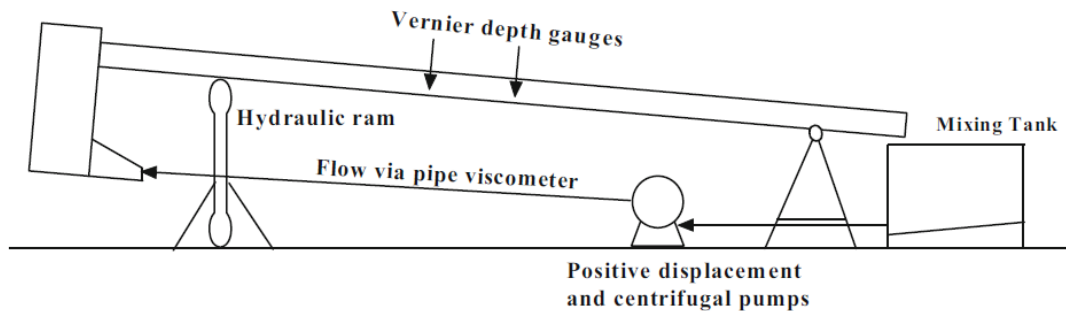


Figure 3.15: Schematic of rectangular flume used by Haldenwang et al.⁴⁵ available under a Creative Commons Attribution Licence

The meshing technique was directed meshing, which resulted in a mesh structure of 46780 cells, shown as Figure 3.16. With respect to the physics of the problem, the same STAR-CCM+ models, shown in Table 3.1, were used with the distinction that the temporal discretization was steady.

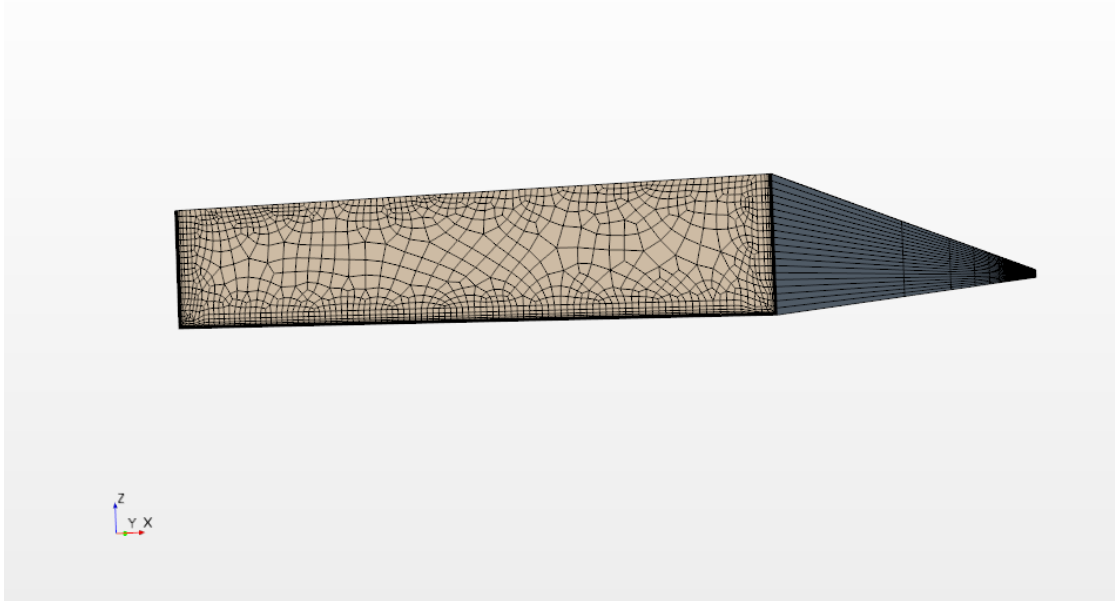


Figure 3.16: Mesh structure for the rectangular channel simulations

3.2.1 Model validation

The rheological properties of the non-Newtonian fluids as well as the experimental conditions used for modelling can be seen in Table 3.4 and 3.5, respectively.

Table 3.4: Rheological properties of the fluids evaluated by Haldenwang et al.⁴⁵

Mixture	Density (kg/m ³)	τ_y (Pa)	k (Pa.s ⁿ)	Power Law Exponent, n
3	1030	0	0.92	0.69
4	1032	2.8	0.008	1.0

Table 3.5: Experimental conditions considered for modelling in the rectangular channel reported by Haldenwang et al.⁴⁵

Case	Q (L/s)	Slope	h (m)	Re _H
3A	2.78	1	0.0438	64
3B	6.79	1	0.0587	164
4A	3.12	1	0.0226	438
4B	4.36	1	0.0243	723

The experiments by Haldenwang et al.⁴⁵ were designed to achieve a steady state depth of flow. Consequently, the simulations were performed with a constant depth of flow. To achieve this, a symmetry plane boundary, which specifies a zero gradient for all flow

variables through the boundary, was used at the free surface, and as mentioned previously, the velocity profile prediction is of interest for these cases. The simulations were stopped when the maximum velocity in the flow domain remained constant for a wide range of iterations. The results, extracted at a position 5 m away from the inlet, are shown of the following Figure 3.17 to 3.20.

From Figures 3.17 and 3.18, it can be seen the simulation results are in excellent agreement with the model of De Kee et al.⁴⁴, for the Power Law fluid described in Table 3.4, and flow parameters for Cases 3A and 3B. It is also evident that both figures are identical because the axes are normalized with the depth of flow and average velocity, meaning the flow behavior will be the same as long as the rheological properties of the fluid remain the same.

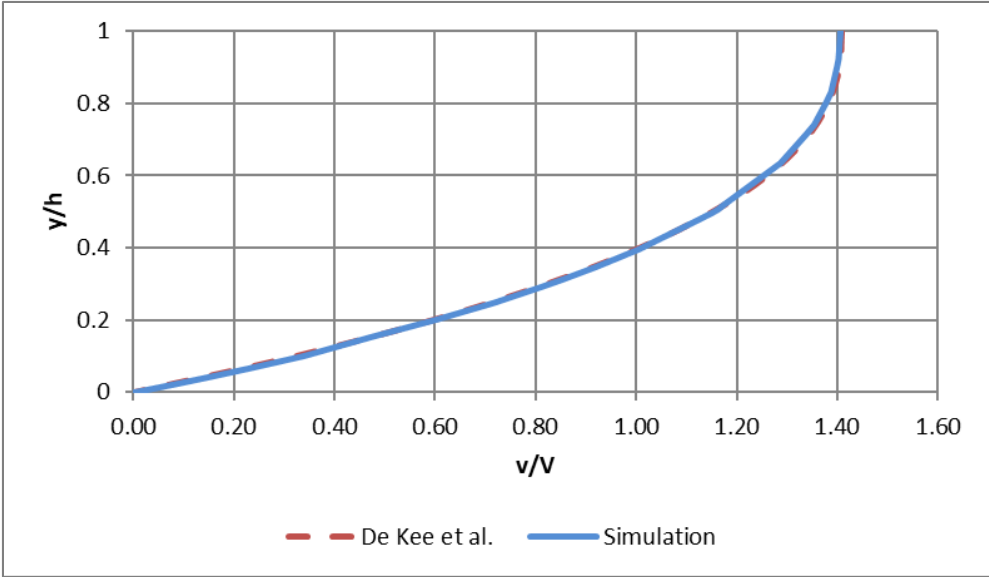


Figure 3.17: Comparison of the normalized centerline velocity profile between simulations and the laminar sheet flow model⁴⁴ for Case 3A

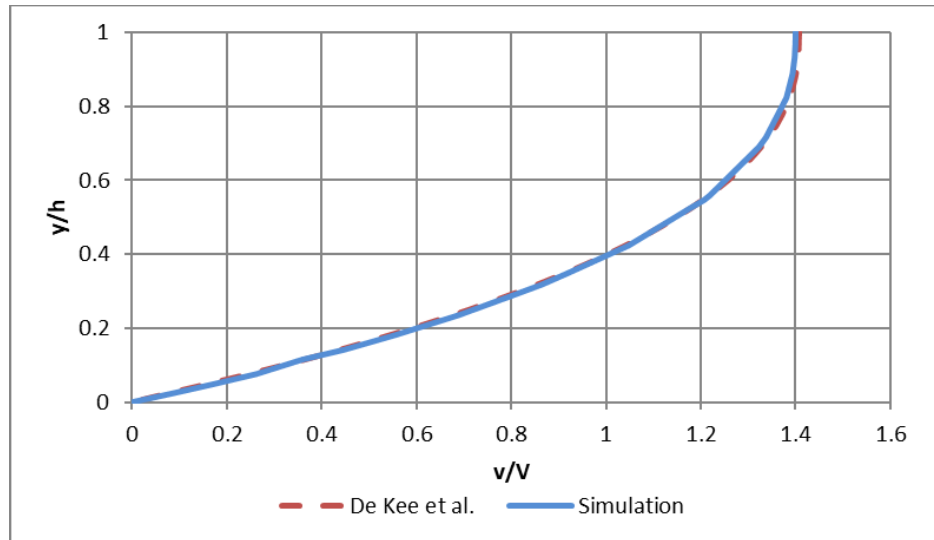


Figure 3.18: Comparison of the normalized centerline velocity profile between simulations and the laminar sheet flow model⁴⁴ for Case 3B

Likewise, Figures 3.19 and 3.20 show that the simulation results for the viscoplastic fluid are consistent with the predictions from the model of De Kee et al.⁴⁴ for the normalized centerline velocity profiles. However, contrary to what was seen with Power Law fluids, the normalized plots do not necessarily collapse on one single curve. This is because increasing the flow rate changes the location of the surface that separates the sheared and the plug regions; the sheared region increases while the plug region decreases with increasing flow rate. This surface is located at y/h values of 0.3 and 0.35, for cases 4A and 4B, respectively.

Given these results, a comparison between the predicted velocity profiles for the semi-circular and the rectangular channel can be made. For the conditions evaluated by Haldenwang et al.⁴⁵ the v/V values at the core range from 1.11 to 1.13, whereas for Cases 2A, 2B, and 2G (from Spelay¹⁷) the v/V values range from 1.37 to 1.68. These remarkable differences can be attributed to wall effects, and higher flow rates leading to transition or turbulence. However, it is difficult to make a direct comparison between both sets of experimental data because the mixtures properties (as shown in Tables 3.1 and 3.5), the geometries of the channels, and the purpose of the studies were different. More studies on this matter are needed to confirm the root of the differences.

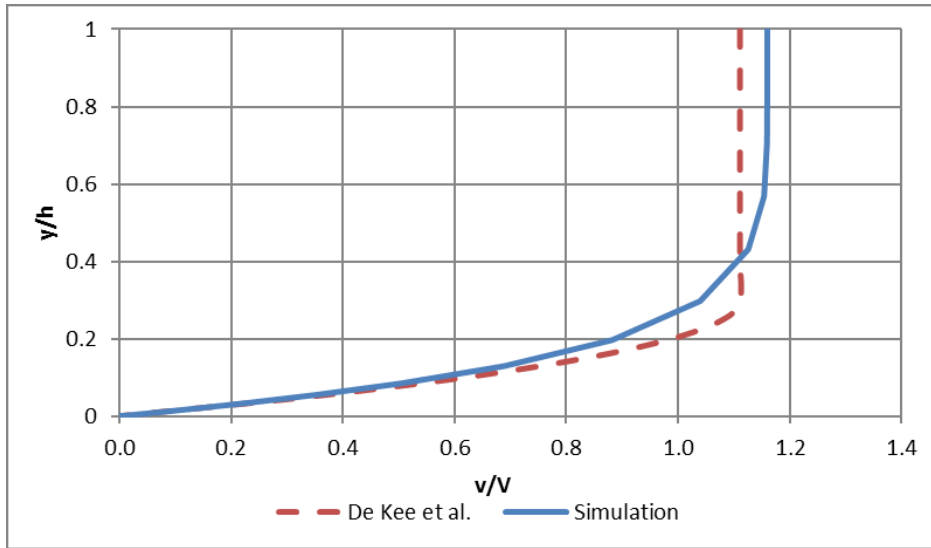


Figure 3.19: Comparison of the normalized centerline velocity profile between simulations and the laminar sheet flow model⁴⁴ for Case 4A

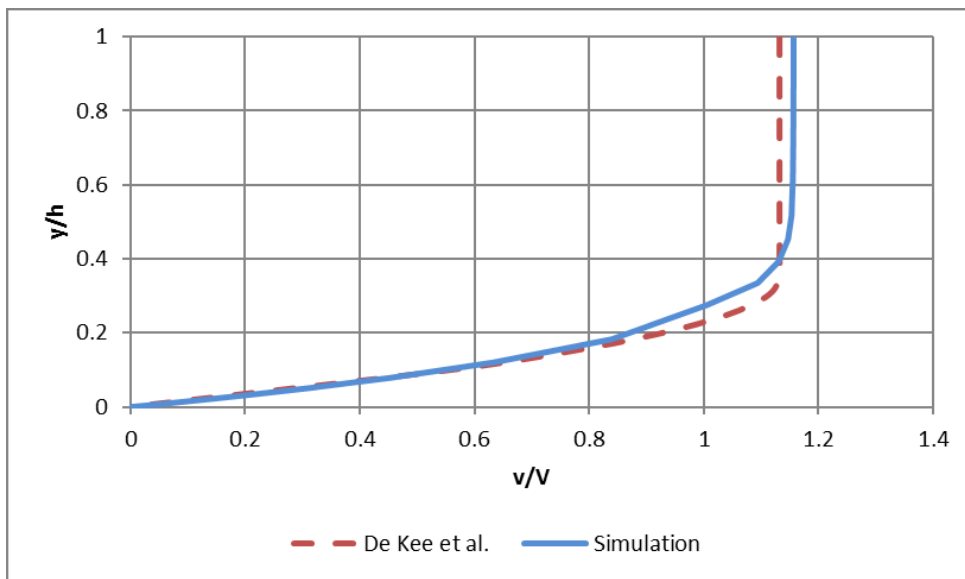


Figure 3.20: Comparison of the normalized centerline velocity profile between simulations and the laminar sheet flow model⁴⁴ for Case 4B.

3.3 Modelling limitations

- The models are limited to laminar flow regime. It was shown that including conditions in the transition or turbulent regime can lead to discrepancies between experiments and simulations
- The VOF model in STAR-CCM+ assumes a shared velocity, temperature, and pressure fields for all phases which has implications on how the data is extracted

from the solution; the volume fraction of the mixture from 0.5 to 1.0 is used as a condition to extract the velocity field corresponding to the mixture.

- The model is restricted to homogeneous mixtures. The VOF model can be coupled with LMP to include particle phases. However, this approach cannot be used for concentrated suspensions as those shown in Chapter 4 and 5. In order to study those suspensions, the Multiphase Segregated Flow, also known Eulerian Multiphase will be used

3.4 Conclusions

- A numerical model was developed using STAR-CCM+ to predict the behavior of non-Newtonian mixtures flowing in a semi-circular flume under laminar flow. The model can predict depth of flow, and wall shear stress within 10% of difference, and average velocity within 4% of difference, when compared with the experimental data from Spelay¹⁷
- The Fanning friction factor was calculated from the simulation results, and then was compared along with the Reynolds number in a Moody diagram using the correlation by Burger et al.⁵³ with excellent agreement
- The simulated velocity profiles were compared with those measured by Spelay¹⁷. While the expected trend for a viscoplastic fluid was seen, there were some discrepancies between prediction and experiments. This could be attributed to experimental uncertainties on the Pitot tube measurements, transition-to-turbulent flow regimes, and VOF modelling assumptions
- To further study the discrepancies surrounding the velocity profile predictions, the experimental conditions by Haldenwang et al.⁴⁵ were considered. These consisted of non-Newtonian mixtures flowing in a rectangular flume under laminar flow. In contrast to Spelay¹⁷, they used UVP as the method to measure local velocity which was validated using the laminar sheet flow model⁴⁴. The simulation results were in close agreement with the prediction of the model by De Kee et al.⁴⁴. Furthermore, a comparison between the simulation results of the semi-circular and rectangular channel showed that the normalized velocity distribution at the core for the cases in the semi-circular channel were up to 48% higher than those in the rectangular channel, suggesting inertial or wall effects were present. However, it is difficult to make a direct comparison given that the mixture properties, geometries, and purpose of the studies were different.

3.5 Recommendations

In order to improve the consistency, accuracy, and the stability of the model the following activities are recommended:

- Perform reliable, high-quality measurements of local velocities of viscoplastic fluids flowing through an open channel. A comparison with additional experimental data, maintaining $Re_H < 1000$ and using mixtures with a wide range of yield stresses, for example 2-40 Pa, could help to address some of the discrepancies observed in some of the modelling results. In addition, if a Pitot tube is used in conjunction with another measurement method, such as UVP, one could validate or disprove the assumptions made for the Pitot tube local velocity measurements for viscoplastic fluids
- Study the ability of the Multiphase segregated model, described in Section 2.6.2, to model the homogeneous, laminar, open-channel flow of non-Newtonian fluids. This will allow to study the air and mixture phases separately and make it easier for the user to extract the desired results
- Although an informal grid refinement study was performed, it is recommended to study the grid dependence of the results in more depth

4. Fluid-particle systems – preliminary studies

The purpose of this chapter is to present the results of a preliminary modelling study of fluid-particle systems using STAR-CCM+ to test its ability to predict characteristic phenomena of suspensions: shear-induced migration, quasi-static settling, and the laminar transport of settling slurries. Three modeling scenarios are considered, as each provides the opportunity to focus on a different mechanism.

4.1 Shear-induced migration

As mentioned in Chapter 2, particles tend to travel from high shear rate to lower shear rate zones, causing heterogeneities in the particle volume fraction distribution²⁸. For this case, the experimental conditions described by Hampton et al.²⁹ were modelled. They studied the shear-induced migration of neutrally-buoyant particles in a tube by measuring the local particle volume fraction and axial velocity using nuclear magnetic resonance (NMR) as shown in Figure 4.1.

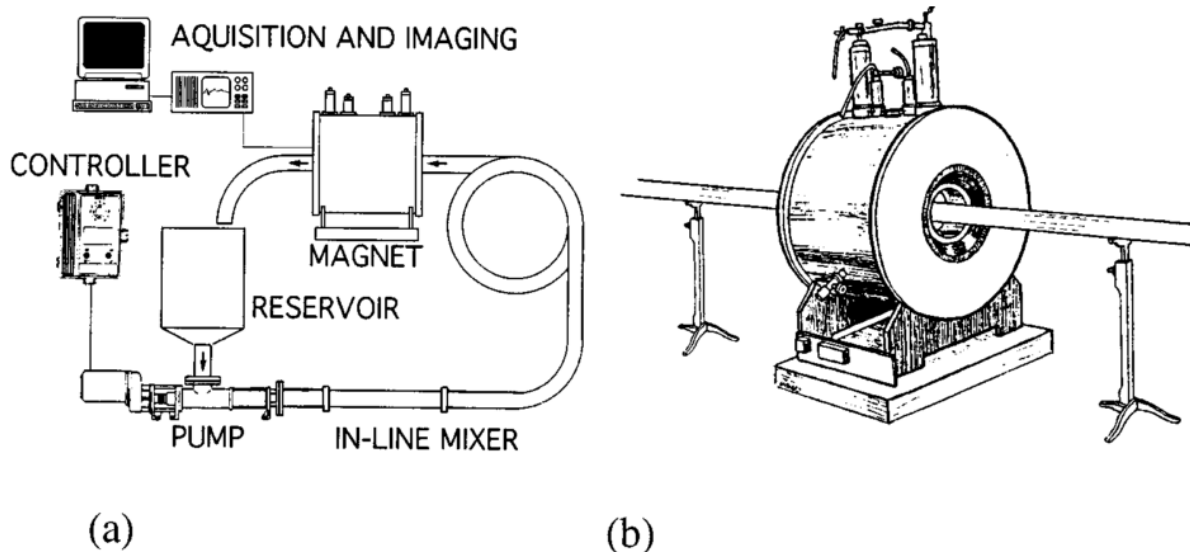


Figure 4.1: (a) Schematic of the experimental setup (b) Superconducting 1.9 T magnet²⁹

i. Geometry and meshing

The flow domain consisted of a circular tube that was 50.8 mm of diameter and was up to 40 m in length to match the experiments of Hampton et al.²⁹. The meshing approach was directed meshing and the cell count ranged from 6500 to 9000, with a base cell size of 4 mm, bigger than the smallest particle in the flow domain. The mesh structure is shown in Figure 4.2.

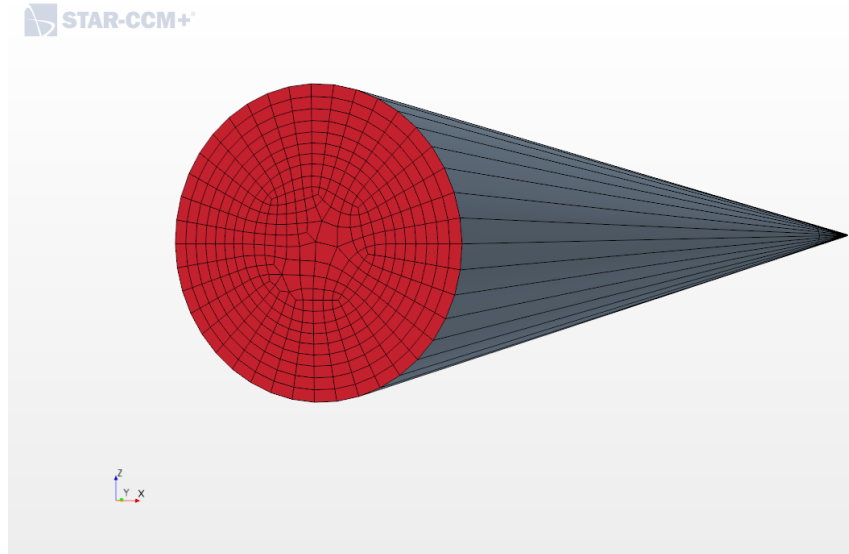


Figure 4.2: Mesh structure for the shear-induced migration simulations

ii. Physics models, solver parameters, stability, and convergence

The STAR-CCM+ models that govern the physics of shear-induced migration are shown in Table 4.1. Particle migration was modelled using the normal viscosity approach described by Equation (2.55).

Table 4.1: STAR-CCM+ models used in the modelling of shear-induced migration

Category	STAR-CCM+ model
Space	Three dimensional
Time	Implicit unsteady (1 st -order upwind)
Material	Eulerian multiphase
Eulerian Multiphase Model	Multiphase segregated flow
	Multiphase equation of state
	Multiphase interaction
Viscous regime	Laminar
Temperature	Isothermal
Density	Constant
Liquid phase viscosity	Newtonian
Drag force	Suspension
Liquid-particle interactions	Suspension rheology (Morris and Boulay)
Other	Solid pressure

The time-step varied from 0.1 ms to 1 s, using the CFL number as the controlling parameter for stability purposes. The under-relaxation factor was set to 0.45 for the velocity solver, 0.3 for the pressure solver, and 0.3 for the volume fraction solver. For the velocity convection, the discretization scheme was 2nd-order upwind; and for the volume fraction convection a 1st-order upwind scheme was used.

iii. Boundary conditions and solution analysis

The following boundary conditions were used in the preliminary simulations involving fluid-particle systems:

- Velocity inlet: specifies the average inlet velocity per phase
- Flow-split outlet: specifies a split ratio or mass flux
- Wall: specifies the no-slip condition at the wall

During the simulations, the maximum CFL number, maximum particle volume fraction, and minimum particle volume fraction were monitored as the engineering quantities of interest. The solution was visualized in real time through scalar scenes and plots. Simulations were stopped when the minimum particle volume fraction did not change significantly with time, which indicates a developed volume fraction profile for a given flow length. An example of how minimum particle volume fraction changes with time for Case 5B is shown as Figure 4.3, where the minimum volume fraction does not change significantly with time after 200 s of solution time.

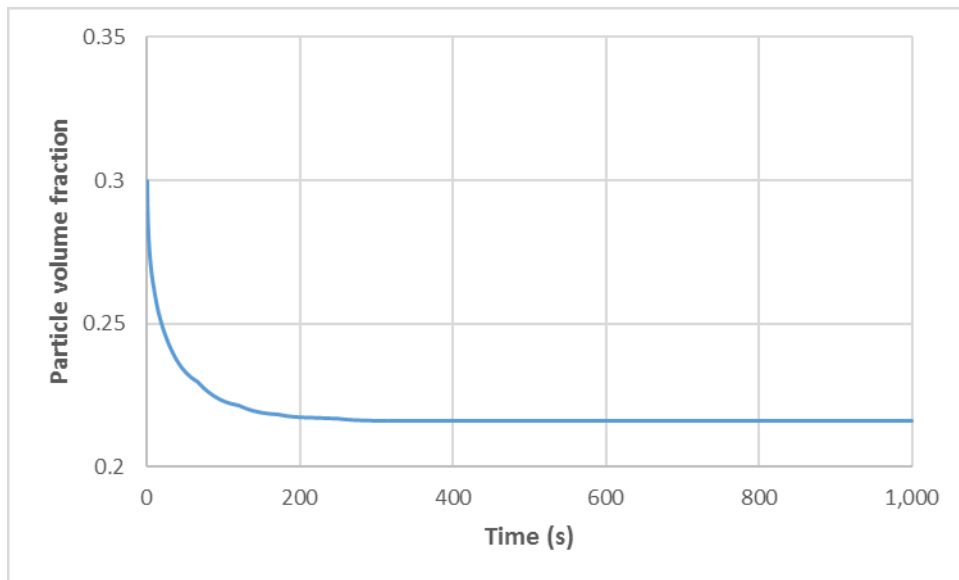


Figure 4.3: Minimum particle volume fraction monitor with respect of time for Case 5B

4.1.1 Model validation

The experimental conditions modelled in this study are shown in Table 4.2, the average velocity and the bulk particle volume fraction were used as boundary conditions. The solid particle phase was modelled as monodisperse.

Table 4.2: Experimental conditions modelled for shear-induced migration²⁹

Case	\bar{v} (m/s)	d (mm)	μ_r (Pa.s)	ρ_f (kg/m ³)	$\phi_{s,bulk}$
5A	0.1	3.175	2.1	1180.7	0.2
5B	0.1	3.175	2.1	1180.7	0.3
5C	0.1	3.175	2.1	1180.7	0.45

The scalar scenes of the developed particle volume fraction and velocity profiles for case 5B are shown as Figure 4.4 and 4.5. They show the model can predict shear-induced particle migration in a tube, namely, particles migrate towards the center of the tube because of the gradients in velocity. The particle volume fraction and velocity profiles from the cases in Table 4.2. are compared with experimental data from Hampton et al.²⁹, shown in Figures 4.6 to 4.11. The solution time was around 2000 s for Case 5A, 1000 s for Case 5B, and 3500 s for Case 5C. Each simulation was completed in 1 to 4 hours.

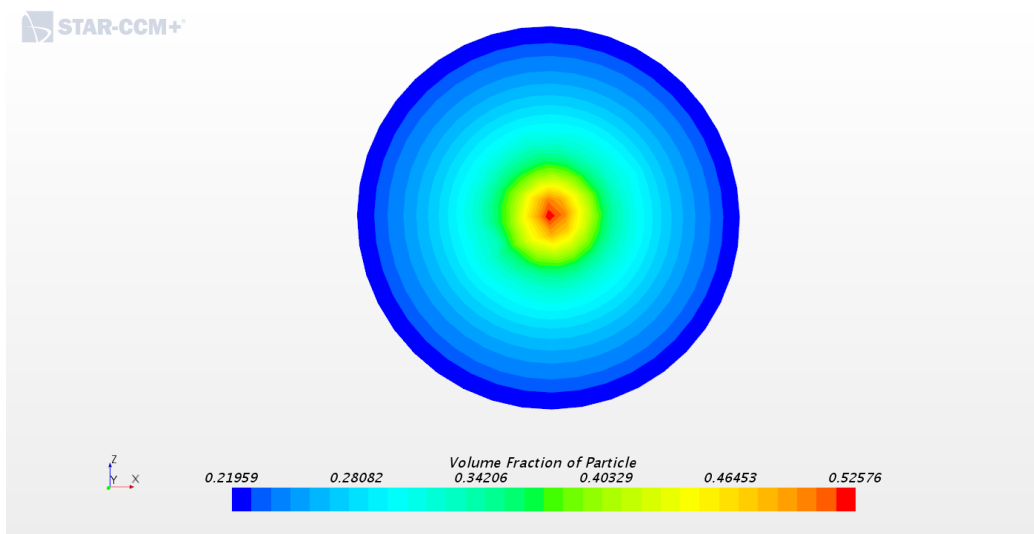


Figure 4.4: Contour plot of the particle volume fraction for Case 5B in a plane perpendicular to the flow direction

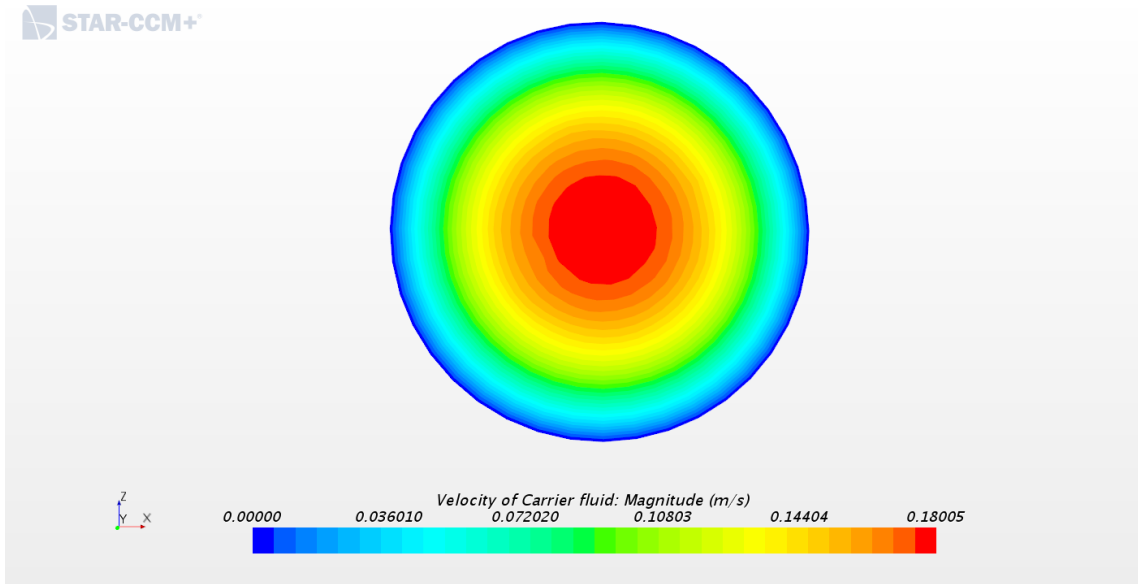


Figure 4.5: Contour plot of the carrier fluid velocity for Case 5B in a plane perpendicular to the flow direction

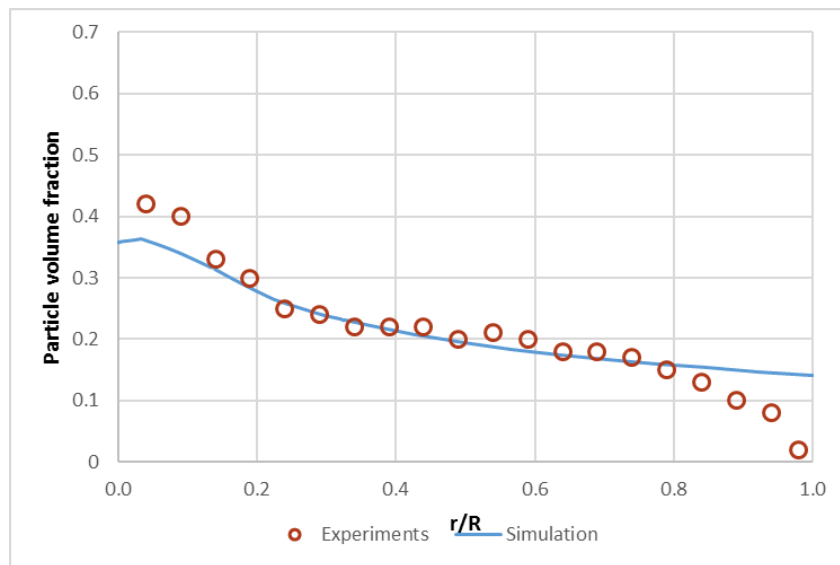


Figure 4.6: Developed particle volume fraction comparison between simulation results and experiments by Hampton et al.²⁹ for Case 5A

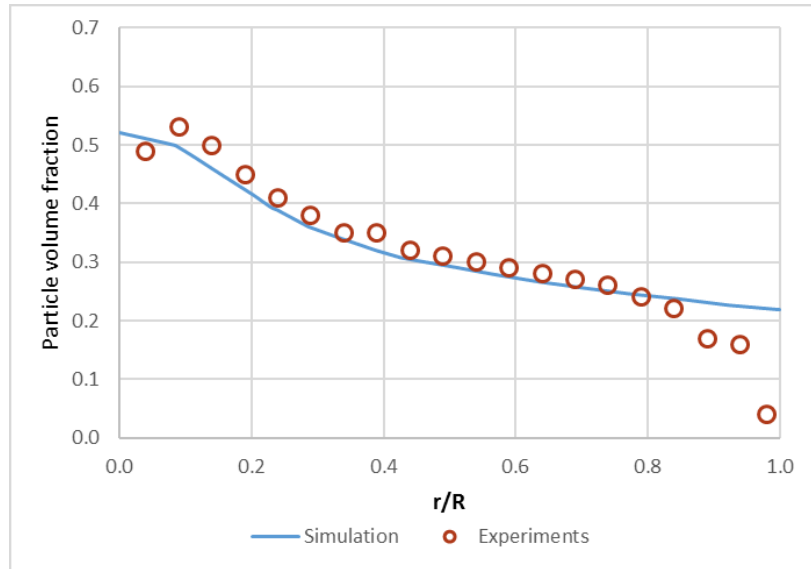


Figure 4.7: Developed particle volume fraction comparison between simulation results and experiments by Hampton et al.²⁹ for Case 5B

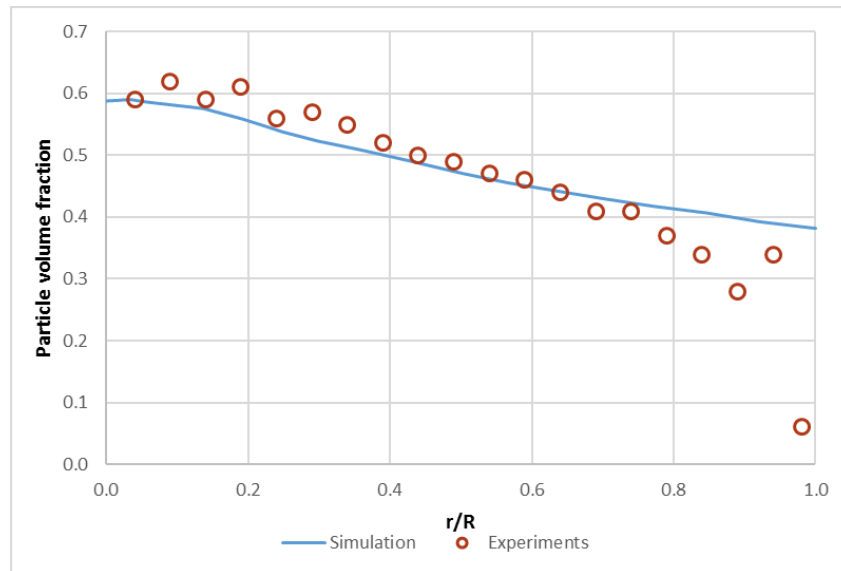


Figure 4.8: Developed particle volume fraction comparison between simulation results and experiments by Hampton et al.²⁹ for Case 5C

Figures 4.6 to 4.8 show the particle volume fraction plotted against the normalized radial direction r/R , where a value of 0 represents the tube center and a value of 1.0 represents the tube walls. The profiles show that shear-induced migration becomes more prevalent as the bulk particle volume fraction increases, because the frequency of the particle-particle interactions increases rapidly for concentrated suspensions²⁴. In general, there is close

agreement between simulations and experiments for $0.2 \leq r/R \leq 0.8$. However, the model is unable to predict a decrease in volume fraction near the wall as was found in the experiments. To further analyze these discrepancies, additional evaluations were performed: the resolution of the mesh was improved at the wall to study a potential effect on the numerical solution; the length of the tube was increased to up to 110 m, in case the simulated flow length was not sufficient to fully develop the particle volume fraction profiles; the time-step was decreased to evaluate its effect on the numerical solution; the lift force, which is experienced by particles and is perpendicular to the relative velocity field, was added as additional physics to the modelling. Also, the wall lubrication force model was added. As described in Section 2.6.2, this model is used to prevent bubbles from touching the walls¹⁰⁰, STAR-CCM+ does not provide a similar built-in model to study wall collision for solid spheres in an Eulerian or continuum framework. None of the approaches mentioned above had a significant effect on the developed particle volume fraction profiles shown in Figures 4.6 to 4.8. Also, Hampton et al.²⁹ compared their experimental results with the model of Phillips et al.³⁰, described in Section 2.4.2, and noticed the same limitations; in fact, the predicted values obtained using the Phillips et al.³⁰ model at the wall for the cases shown in Figures 4.6 to 4.8 are very similar to those predicted by the model presented here. Thus, it is recommended that additional particle-level studies, such as with the use of DEM, be conducted to study wall collisions in more detail and improve the suspension rheology model. Although this is beyond the scope of this project, for a recent study on this subject the reader is referred to the work of Tomac and Gutierrez¹⁰¹.

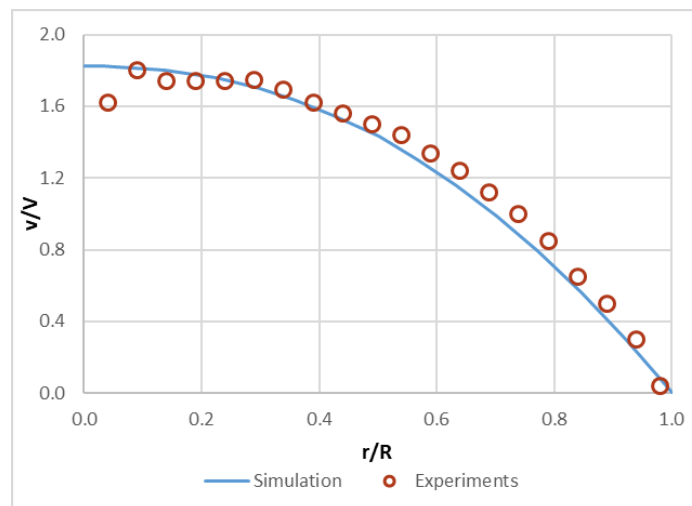


Figure 4.9: Developed velocity profile comparison between simulation results and experiments by Hampton et al.²⁹ for Case 5A

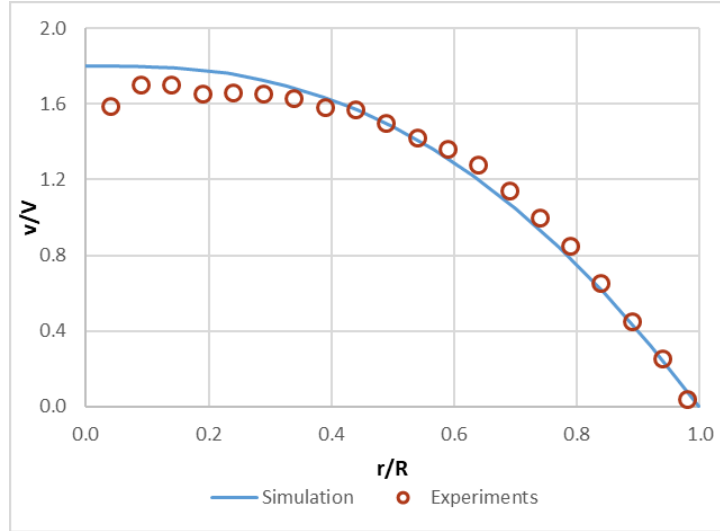


Figure 4.10: Developed velocity profile comparison between simulation results and experiments by Hampton et al.²⁹ for Case 5B

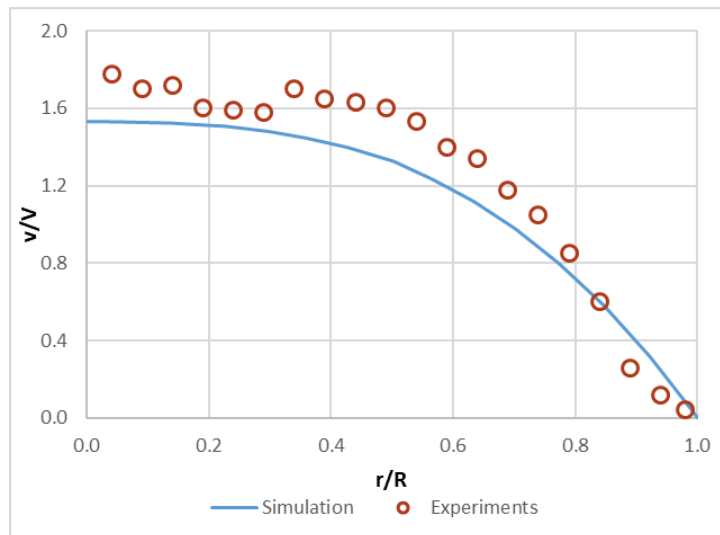


Figure 4.11: Developed velocity profile comparison between simulation results and experiments by Hampton et al.²⁹ for Case 5C

Figures 4.9 to 4.11 show a comparison between the simulated and experimental velocity profiles. In these plots, the local velocity was normalized using the average velocity and plotted against the normalized radial distance, r/R . There is close agreement between experiments and simulation results for cases 5A and 5B. For case 5C, where the bulk particle volume fraction is 0.45, there is more scatter in the experimental data because the higher particle concentration causes an increase in particle-particle interactions, such as collisions, which causes more (and stronger) fluctuations in the local velocity

measurements. It is also shown that the velocity profiles become blunter, i.e. v/V values at the center of the tube start to decrease as the bulk particle concentration increases. This effect is a consequence of the mixture viscosity increase with increasing particle volume fraction.

As the particle volume fraction increases, the entrance length (L/D), necessary to achieve fully developed profiles for the velocity and particle volume fraction, decreases rapidly, which is consistent with the results reported by Hampton et al.²⁹, shown in Table 4.3. In addition, the simulated average wall shear stress is shown in Table 4.3; even though these were not reported by Hampton et al.²⁹, it can be seen that an increase in the particle bulk volume fraction from 0.3 to 0.45 increases the average wall shear stress by 130 % which has implications on the energy requirements to transport these suspensions.

Furthermore, it should be noted that STAR-CCM+ struggled with stability in the simulations where the particle volume fraction anywhere in the flow domain approached the maximum packing volume fraction. As mentioned in Chapter 2, most numerical methods become limited when maximum packing is approached.

Table 4.3: Experimental entrance length and simulated average wall shear stress for cases in Table 4.2

$\phi_{s,bulk}$	Entrance length (L/D) ²⁹	Average wall shear stress (Pa)
0.2	785	46
0.3	183	60
0.45	42	139

4.2 Single-particle settling in viscoplastic fluids

The settling of a falling sphere through a viscoplastic fluid³⁵ is modelled. The experimental study consisted on spheres being thrown from the top of a settling column. Several viscoplastic mixtures were used with yield stress values ranging from 1.3 to 30 Pa. Different types of spheres (ceramic, steel, and aluminum) with diameters ranging from 12.7 to 19 mm and densities from 2710 to 7841 kg/m³ were used. The settling velocities of the spheres were measured using Electrical Impedance Tomography (EIT). With that information, a correlation was developed to predict the terminal velocity of spheres as described in Chapter 2. A schematic representation of the settling column is shown as Figure 4.12.

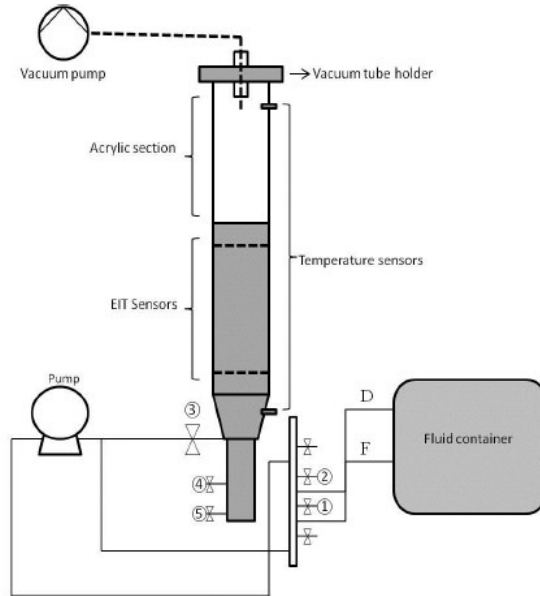


Figure 4.12: Schematic representation of the settling column used by Shokrollahzadeh³⁵

i. Geometry and meshing

The geometry was created to be two dimensional and was 101.6 in width and 1.5 in height. This resulted in a mesh structure with 1120 quadrilateral cells, as shown in Figure 4.13.

ii. Physics models, solver parameters, stability, and convergence

The main STAR-CCM+ models used for the description of the physics of single-particle settling in viscoplastic fluids are shown in Table 4.3. The Lagrangian Multiphase model (LMP) was used to model the solid particle phase, for better visualization and tracking of the particle phase.

Table 4.4: STAR-CCM+ models used in the single-particle settling simulations

Category	STAR-CCM+ model
Space	Two dimensional
Time	Implicit unsteady (1 st -order upwind)
Material	Lagrangian multiphase
	Eulerian multiphase (2 nd -order upwind)
Viscous regime	Laminar
Temperature	Isothermal
Density	Constant
Other	Gravity

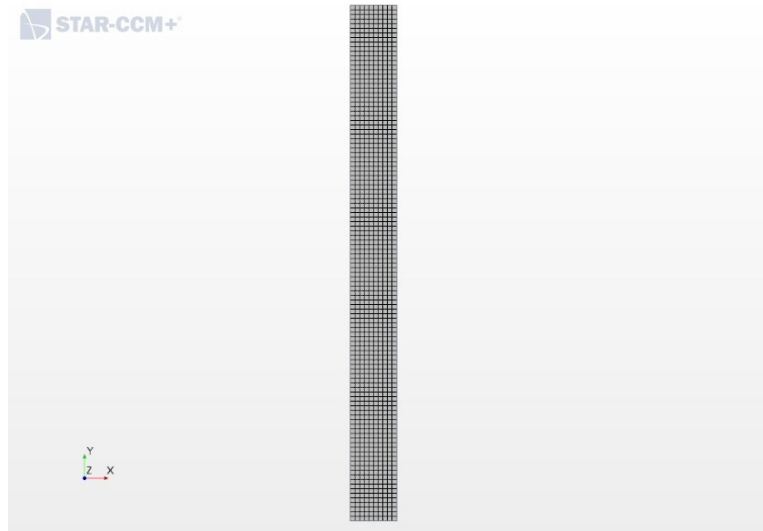


Figure 4.13: Mesh representation for single-particle settling simulations.

The time-step was set at 0.5 ms to ensure proper visualization of particle settling. The under-relaxation factor values for velocity and pressure solvers were 0.8 and 0.2 respectively. To avoid wall effects, the particle was injected at the midpoint located at the top of the column. The particle was injected to the viscoplastic fluid from rest; it then starts to settle because of gravity effects. The value of settling velocity was selected as the maximum velocity of the particle in the column once it did not change significantly with time. Figure 4.14 shows the variation of the particle settling velocity with time during the simulations, where a steady value is achieved after approximately 0.3 seconds. Simulations were typically run for 15 to 30 min.

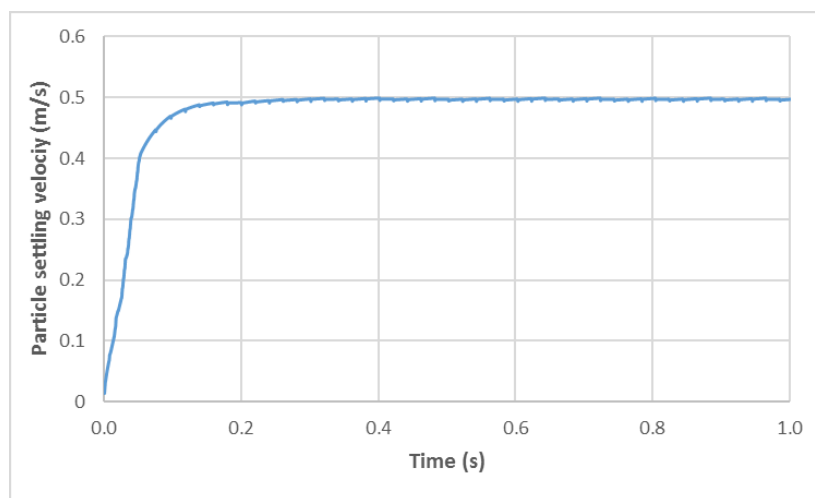


Figure 4.14: Maximum particle velocity monitor plot using STAR-CCM+ for Case 10B

4.2.1 Model validation

The rheological properties of the viscoplastic mixtures and particle properties used for the simulations are shown in Table 4.5.

Table 4.5: Experimental conditions used in the particle settling simulations of the present study³⁵

Case	τ_y (Pa)	μ_p (Pa.s)	ρ_f (kg/m ³)	ρ_s (kg/m ³)	d (mm)
6A	14.5	0.054	1287	7697	19.0
6B	14.5	0.054	1287	7684	14.3
7A	27.3	0.145	1331	7684	14.3
7B	27.3	0.145	1331	7722	15.9
8	30	0.98	1357	3940	19.0
9	16.2	0.33	1314	3940	19.0
10A	12.2	0.45	1320	7864	14.3
10B	12.2	0.45	1320	3940	19.0
10C	12.2	0.45	1320	7841	12.7

As described in Section 2.4.1, there are multiple correlations available to calculate the drag coefficient of a solid sphere settling in a viscoplastic fluid, only the ones by Atapattu et al.⁶⁹, and Shokrollahzadeh³⁵ are considered in this study. In an Eulerian framework, STAR-CCM+ includes the correlation by Atapattu et al.⁶⁹ when using non-Newtonian fluids. However, in a Lagrangian framework, it is not included in the calculation. Thus, this correlation was added as a user-defined function. Also, since the correlation by Shokrollahzadeh³⁵ uses an equivalent Newtonian viscosity approach, a combination of methods to solve for the dynamic viscosity and the drag coefficient can be made, as summarized in Table 4.6.

Table 4.6: Modelling approaches for a solid sphere settling in a viscoplastic fluid.

Method	Dynamic viscosity calculation	Drag coefficient calculation
1	Non-Newtonian Generalized Power Law, Equation (2.68)	Drag coefficient for viscoplastic fluids, Equation (2.30)
2	Equivalent viscosity method, Equation (2.37)	Drag coefficient for viscoplastic fluids, Equation (2.30)
3	Equivalent viscosity method, Equation (2.37)	Newtonian Method, see Table 2.1

A comparison between simulation results, using the approaches in Table 4.6, and the experiments is shown as a parity plot in Figure 4.15. Of the three methods shown in Table 4.6, Method 3 was more accurate in all conditions shown in Table 4.5. In general, Methods 1 and 2 underpredicted the particle settling velocity by as much as a factor of 2, except for Cases 8 and 9; also, it can be seen the predicted values for Methods 1 and 2 tend to be the same for a set of given conditions, implying that the drag coefficient calculation is the predominant factor in modelling these conditions. As for Method 3, the results from 6 out of 9 conditions are within $\pm 10\%$ of difference with the parity line. In addition, the results from Method 3 are shown in a standard Newtonian drag curve in Figure 4.16.

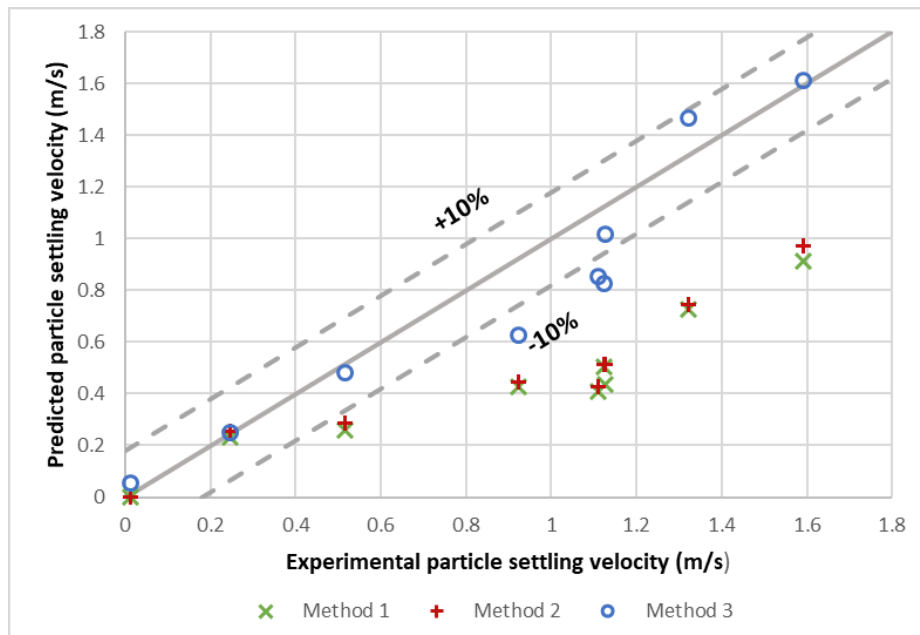


Figure 4.15: Comparison between simulation results and experiments for a particle settling in a viscoplastic fluid. Conditions listed in Table 4.5

Figure 4.16, shows there is significant scatter of the simulation results from the Newtonian drag curve when $Re^* < 50$, which was also the case for the experiments³⁵ as shown in Figure 2.7. More studies are needed for low Re^* numbers, where other mechanisms are possibly at play; it seems assuming an equivalent Newtonian viscosity can be problematic when the characteristic shear stress on the sphere approaches the value of the yield stress of the fluid. Because of this, a proper visualization of the shear field (or shear envelope) was not possible. Nevertheless, the model can be used to evaluate multiple settling conditions in a timely manner.

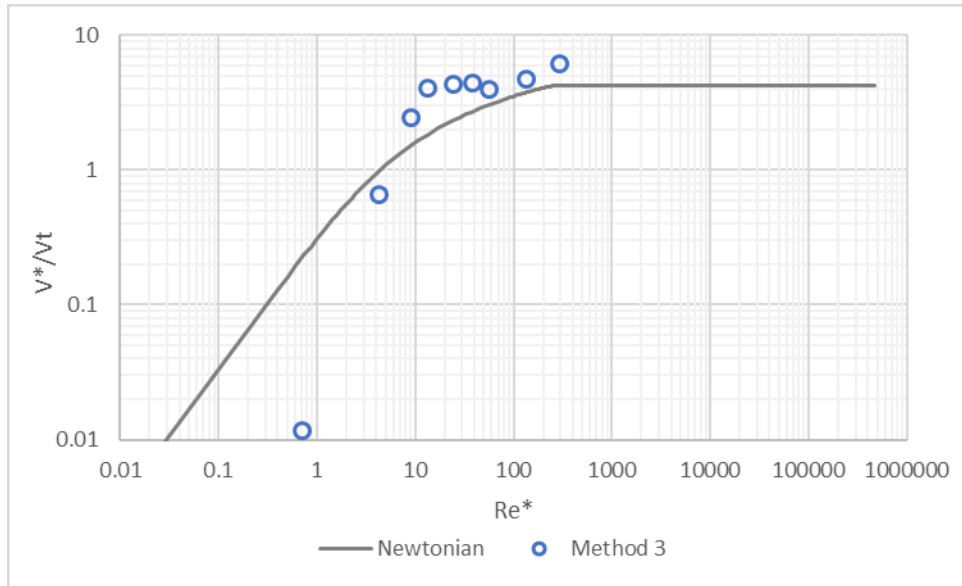


Figure 4.16: Comparison between simulation results and the Newtonian drag curve

4.3 Laminar transport of coarse particles

The transport of negatively-buoyant particles was also studied. This combines the effects of shear-induced migration and hindered-particle settling. The experimental studies by Gillies et al.³² were modelled. Their setup consisted of a 50 mm (diameter) loop where sand suspended in a Newtonian oil was circulated, shown here as Figure 4.17. They measured solid concentration distribution, using a gamma ray densitometer; velocity distribution, using a constant-temperature hot-film anemometer; as well as pressure gradients.

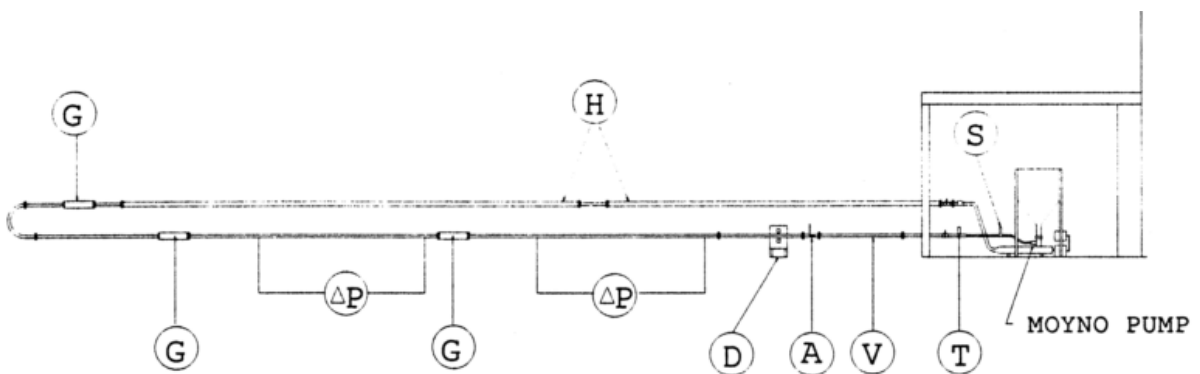


Figure 4.17: The 50 mm pipeflow loop used in the experiments by Gillies et al.³² where: d) Gamma ray densitometer, g) Glass observation section, h) Heat Exchanger, a) Hot film anemometer, s) Sampler, T) Temperature sensor, V) Acrylic observation section

i. Geometry and meshing

The pipe was 52.5 mm in diameter and was 30 and 60 m in length for Cases shown in Table 4.7. The meshing approach was direct meshing, resulting in mesh structures with 6500 and 19000 cells for Cases 11A and 11B, respectively. The mesh structure for Case 11A is shown as Figure 4.18.

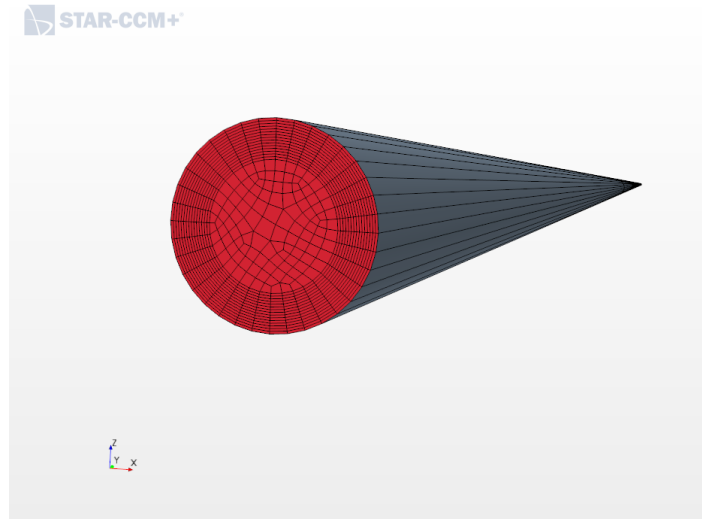


Figure 4.18: Mesh structure used in the laminar transport of coarse particles simulations

ii. Physics models, solver parameters, stability, and convergence

The STAR-CCM+ models used to describe the physics involved in the laminar transport of coarse particles are the same as those shown in Table 4.1, with the addition of the gravity force model for negatively-buoyant particles.

The time-step varied from 0.01 ms to 0.5 s, and was determined by monitoring the CFL number in the fluid domain. The under-relaxation factors were 0.27 for the velocity solver, 0.1 for the pressure solver, and 0.1 for the volume fraction solver. The simulations were stopped when the maximum particle volume fraction and the particle volume fraction profile did not change significantly with time.

4.3.1 Model validation

The experimental conditions that were modelled are shown in Table 4.7. Preliminary simulations were performed to choose the expression of relative viscosity that best represented the experimental behaviour. As mentioned before, Equations (2.45) and (2.47) are built-in within STAR-CCM+, whereas Equation (2.48) was introduced as a user-defined function. The results showed that Equation (2.47), proposed by Morris and Boulay²⁷,

described the experimental behaviour more accurately in comparison with the other two. The average velocity and particle bulk volume fraction were used as boundary conditions. The particle phase was modelled as monodisperse

Table 4.7: Experimental conditions modelled for the laminar transport of settling slurries

Case	\bar{v} (m/s)	d (mm)	μ_f (Pa.s)	ρ_f (kg/m ³)	ρ_s (kg/m ³)	$\phi_{s,bulk}$
11A	0.014	0.43	1.44	876	2650	0.2
11B	0.061	0.43	1.44	876	2650	0.2

The simulation results were compared with the chord-average volume fraction profiles reported by Gillies et al.³² and are shown in Figures 4.19 and 4.20. The solution times were around 1000 and 2000 s for cases 11A and 11B, respectively.

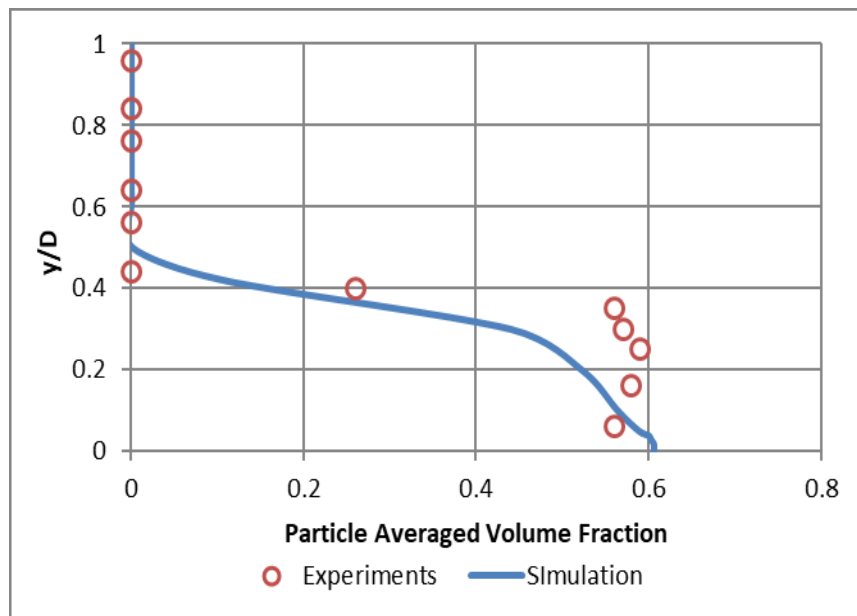


Figure 4.19: Particle volume fraction profile between simulation results and experiments by Gillies et al.³² for Case 11A

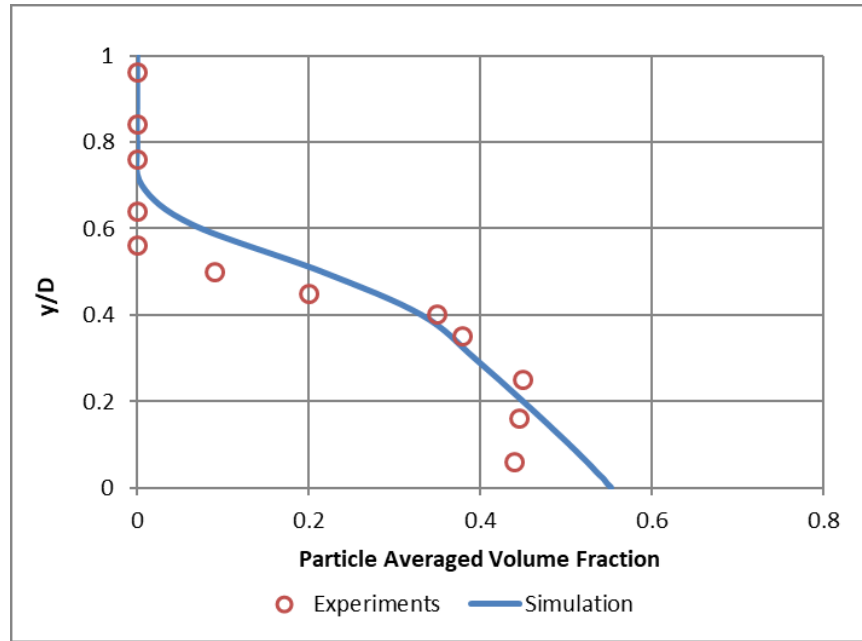


Figure 4.20: Particle volume fraction profile between simulation results and experiments by Gillies et al.³² for Case 11B

In Figures 4.19 and 4.20, the vertical chord-averaged volume fraction is plotted against y/D , which is the normalized vertical position using the pipe diameter. It is shown that STAR-CCM+ can predict the overall behaviour of the transport of settling slurries when compared with the data gathered by Gillies et al.³² during their experiments. A comparison between the volume fraction profiles also suggests that increasing the bulk velocity, while maintaining the rheological properties improves particle transport. However, there are discrepancies between experiments and simulation results by as much as 40% for Case 11A and 20% for Case 11B; it was unclear whether the simulations needed more time or additional flow length to improve the results. Also, as mentioned before when the volume fraction approaches the maximum packing concentration, the solver struggles. When this happened, the time-step had to be reduced significantly, limiting the amount of time the simulations could be run.

In addition, Figure 4.21 shows a comparison between the carrier fluid velocity profiles of Cases 11A and 11B. Gillies et al.³² were unable to obtain meaningful measurements of the velocity distribution when the sand concentration was high; however, they pointed out an asymmetry of the velocity distribution in the carrier fluid due to settling. For Case 11A, the velocity profile suggests the formation of a settled bed of about 3 particle diameters at the bottom of the pipe. In contrast, increasing the bulk velocity from 0.014 to 0.061 m/s

increases the particle transport to the extent that there is no formation of a settled bed, as shown by the velocity profile for case 11B. The simulated pressure drops were 650 Pa and 3000 Pa, whereas the ones reported by Gillies et al.³² were 800 Pa and 2900 Pa for the conditions simulated in cases 11A and 11B.

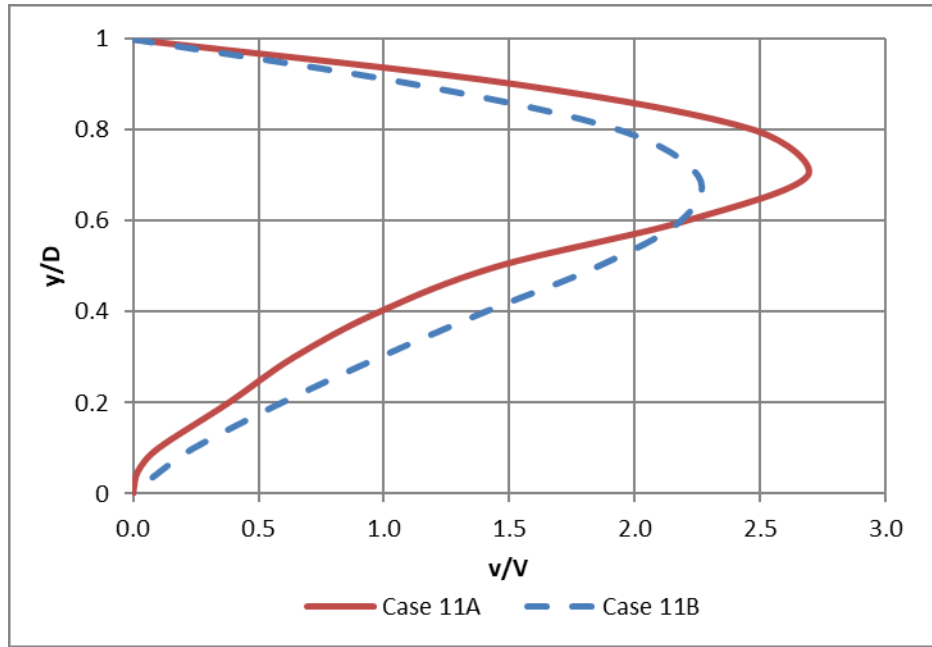


Figure 4.21: Simulated velocity profiles for Cases 11A and 11B

The goal of the studies presented in this chapter was to model characteristic phenomena of suspensions involved in the subsequent modelling stages of the present study; i.e. shear-induced migration, single-particle settling in viscoplastic fluids, and the laminar pipeline transport of settling slurries. Experimental studies where each mechanism could be studied separately were chosen. For the shear-induced migration modelling, it was shown that by using the “normal viscosity” approach, proposed by Morris and Boulay²⁷, the model captures the overall behaviour of particles migrating towards the center of a tube due to shear rate gradients. However, the model is unable to account for particle-wall collisions. The extent to which this lack of particle-wall interaction can affect particle settling modelling is unknown; numerical, particle-level studies can be done to improve the predictions of the model. Single-particle settling of a sphere in a viscoplastic fluid was modelled using experimental conditions from Shokrollahzadeh’s³⁵ study. Two correlations for the calculation of the drag coefficient were considered^{35,69}, it was determined that the one proposed by Atapattu et al.⁶⁹ underpredicted the experimental results in all cases; the correlation proposed by Shokrollahzadeh³⁵ produced better simulation results when compared with the

experimental data. However, care should be taken when using this correlation as it assumes an equivalent Newtonian viscosity to account for the viscosity of the viscoplastic fluid, and its results deviate considerably from a Newtonian drag curve when $Re^* < 50$. For the laminar pipeline transport of settling slurries, the studies by Gillies et al³² were modelled. While the model predicts the overall behaviour of particle settling, there were discrepancies between simulations and experiments of up to 40%, it is unclear if more time or longer pipes were needed to refine the results. The simulated pressure gradients were within 20% of difference for Case 11A and 4% for Case 11B.

4.4 Modelling limitations

- The suspension rheology model is unable to predict a decrease in the particle volume fraction at the wall to the extent the experiments by Hampton et al.²⁹ showed for the shear-induced migration of neutrally buoyant particles suspended in a Newtonian fluid
- The STAR-CCM+ solver struggled with stability of the simulation when the volume fraction within the flow domain approached the maximum packing concentration, requiring a significant decrease in time-step, limiting the amount of time each simulation could be run
- The built-in mesh generation models in STAR-CCM+ only allowed for tube lengths up to 115 m
- The drag force calculation in a Lagrangian framework within STAR-CCM+ does not allow to introduce non-Newtonian behaviour on its calculation, which requires the use of UDFs to account for this effect
- The model developed for the study of single-particle settling in viscoplastic fluids uses Shokrollahzadeh's³⁵ approach to calculate for an equivalent Newtonian viscosity. Thus, it suffers from the same limitations as the correlation and deviates significantly from the Newtonian drag curve when $Re^* < 50$

4.5 Conclusions

- A numerical model was developed to study the shear-induced migration of neutrally buoyant particles suspended in a Newtonian Fluid, which was successfully compared with experimental data by Hampton et al.²⁹
- There was good agreement between the simulated velocity profiles and the experiments, for all cases
- There were discrepancies on the particle volume fraction predictions as $r/R > 0.8$, for all cases

- A numerical model to study particle settling of a sphere in viscoplastic fluids was developed and compared successfully with available experimental data by Shokrollahzadeh³⁵
- There is significant scatter of the particle settling velocity results and the Newtonian drag curve for $Re^* < 50$
- A numerical model was developed to study the laminar transport of settling slurries and compared successfully with experimental data
- This model was able to capture the overall behaviour as seen in the experiments by Gillies et al.³². However, there were discrepancies between simulation results and experiments. This is related with the instability of the model when solving the flow when maximum packing is reached in the flow domain
- The simulated velocity profiles showed the formation of a settled bed at the bottom of the pipe and asymmetry between the upper and lower half because of the effect of particle settling. Increasing the bulk velocity improves particle transport under laminar flow conditions to the extent that the settled bed disappears
- For two different cases, the simulated pressure gradients were within 20% and 4% of difference when compared with the experiments

4.6 Recommendations

The following studies are recommended to expand the reliability of the model and improve our understanding of the physics:

- Study in more detail the wall effects on particle volume fraction profiles of neutrally buoyant particle in a tube. DEM studies can be done to account for particle wall collisions. This could aid in the development of models that account accurately for particle-wall collisions.
- Validate the single-particle settling model using data from studies with Power Law fluids and Herschel-Bulkley fluids to further study the effect of the yield stress in particle settling
- Study the mechanism(s) that govern particle settling in viscoplastic fluids at $Re^* < 50$

5. Laminar, open-channel flow of non-Newtonian suspensions

Recall that the main goal of this project is to model the settling behaviour of monodisperse coarse particles, suspended in a non-Newtonian fluid flowing under laminar, open-channel flow conditions. The experimental data from Spelay¹⁷ were used for validation of the CFD model; a description of his experimental setup is shown in Chapter 3.

Preliminary modelling studies with three Eulerian phases (i.e. carrier fluid-coarse particle-air phases) proved to be more challenging than expected. A single simulation could take weeks or months because of the small time-steps required to archive stability of the solver. Thus, the focus was shifted to the study of particle settling only; in other words, the simulations were set up using a constant depth of flow. This allowed for faster simulations because the air phase was not considered into the calculations.

i. Geometry and meshing

The same semi-circular channel as described in Section 3.1 was modelled, with the distinction that the channel was truncated to match a constant depth of flow throughout the channel for each condition. Likewise, the meshing technique was directed meshing, resulting in approximately 27000 cells. A schematic of the mesh is shown as Figure 5.1.

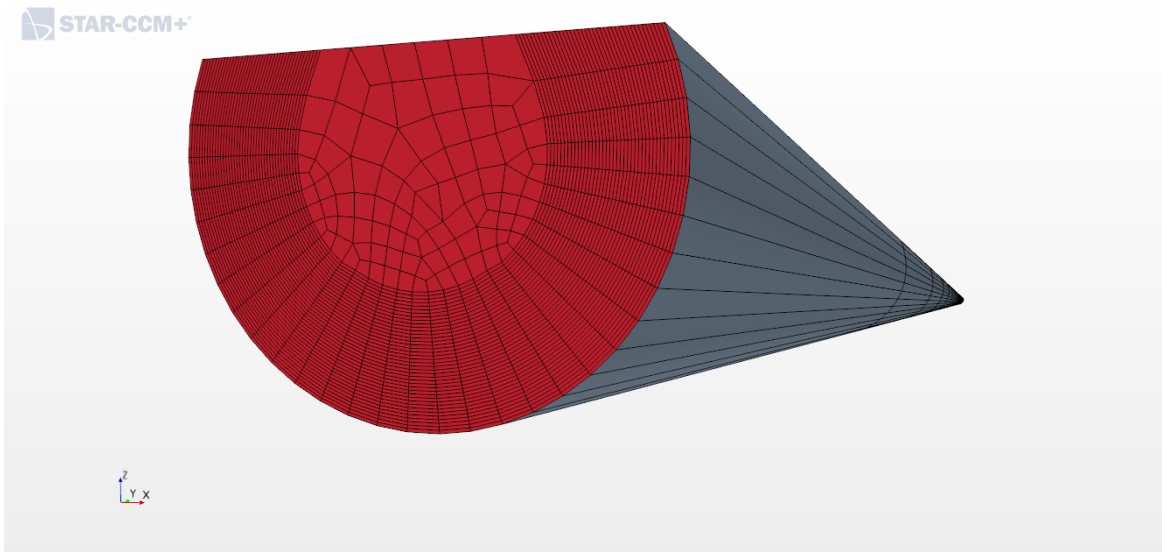


Figure 5.1: Mesh structure used for non-Newtonian suspension simulations

ii. *Physic models, solver parameters, stability, and convergence*

The STAR-CCM+ models used to describe the physics of the problem are shown in Table 5.1.

Table 5.1: STAR-CCM+ models used to model non-Newtonian suspensions

Category	STAR-CCM+ model
Space	Three dimensional
Time	Implicit unsteady (1 st -order upwind)
Material	Eulerian multiphase
Eulerian Multiphase Model	Multiphase segregated flow
	Multiphase equation of state
	Multiphase interaction
Viscous regime	Laminar
Temperature	Isothermal
Density	Constant
Liquid phase viscosity	Newtonian
Drag force	Suspension
Liquid-particle interactions	Suspension rheology (Morris and Boulay)
Other	Solid pressure
	Gravity

As before, the CFL number was maintained at a value less than 1 to ensure stability, with the time-step constrained by that condition. In addition, the maximum carrier fluid velocity, and maximum particle concentration were monitored as engineering quantities of interest, and the residuals were monitored for convergence purposes. The under-relaxation factors for velocity, pressure, and volume fraction were kept at 0.27, 0.1, and 0.1, respectively. The convention discretization scheme was 2nd-order upwind for the velocity and 1st-order upwind for the volume fraction.

iii. *Boundary conditions and solution analysis*

The flow boundaries were:

- Velocity inlet: specifies the average velocity at the inlet, per phase (this boundary can be used interchangeably with mass flow inlets for incompressible fluids)
- Flow-split outlet: specifies a split ratio or mass flux

- Wall: specifies the no-slip condition
- Symmetry plan: at this boundary slip can occur, and there are no gradients of any flow variable through the boundary

Since the goal is to study particle settling first, the solution was initialized with the boundary conditions throughout the flow domain which allowed for faster simulation times. For stability purposes, the initial time-step was 10 μs ; after the residuals dropped by multiple orders of magnitude for the continuity equation, the time-step was gradually increased as high as the CFL constraint would allow. The solution was visualized through scalar scenes and plots for the carrier fluid velocity, particle volume fraction, dynamic viscosity, and wall shear stress. Simulations were run for 10,000 s.

5.1 Model validation

The idealized tailings mixture and particle properties from the studies of Spelay¹⁷ are shown in Table 5.2 whereas the experimental conditions used as input parameters of the simulations are shown in Table 5.3, the average velocity and bulk particle volume fraction were used as boundary conditions. Figures 5.2 and 5.3 show the particle volume distribution and velocity distribution as contour plots, respectively. The simulation results were then compared with the chord-averaged sand volume fraction profiles measured by Spelay¹⁷ plotted against the normalized vertical position y/D . These are shown in Figures 5.4 to 5.7. As mentioned earlier, there were limitations which prevented accurate measurements of local mixture velocities when the yield stress was high; thus, only the simulated velocity profile is shown (with no experimental measurements) as Figure 5.8.

Table 5.2: Mixture and particle properties used in the modelling of the laminar, open-channel flow of non-Newtonian suspensions¹⁷

ρ_m (kg/m ³)	τ_y (Pa)	k (Pa.s ⁿ)	Power Law Exponent, n	d (mm)	ρ_s (kg/m ³)
1510	40	0.04	1.0	0.18	2650

Table 5.3: Experimental conditions modelled in the transport of coarse particle suspended in a viscoplastic fluid.

Case	Q (L/s)	V (m/s)	Slope (°)	h (m)	ϕ_s	Re _H
12A	5.0	0.41	4	0.1039	0.125	55
12B	2.5	0.19	4.5	0.1077	0.1	48
12C	5.0	0.44	4.5	0.0968	0.11	59
12D	5.0	0.5	5.4	0.0861	0.11	8

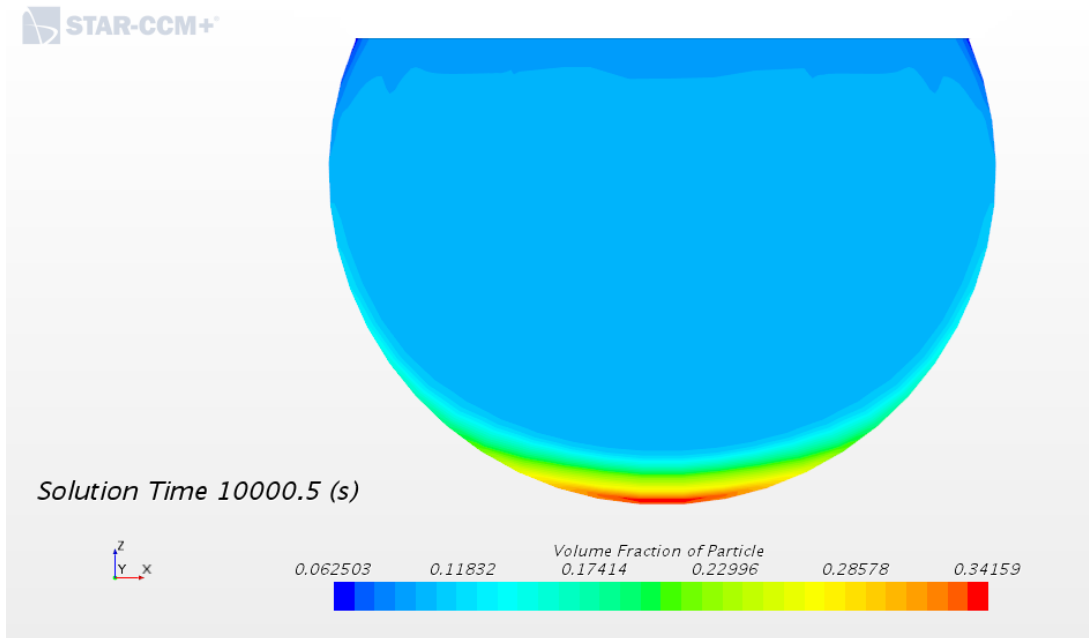


Figure 5.2: Contour plot for particle volume fraction, 14.5 m away from the channel inlet, perpendicular to the flow, for Case 12B

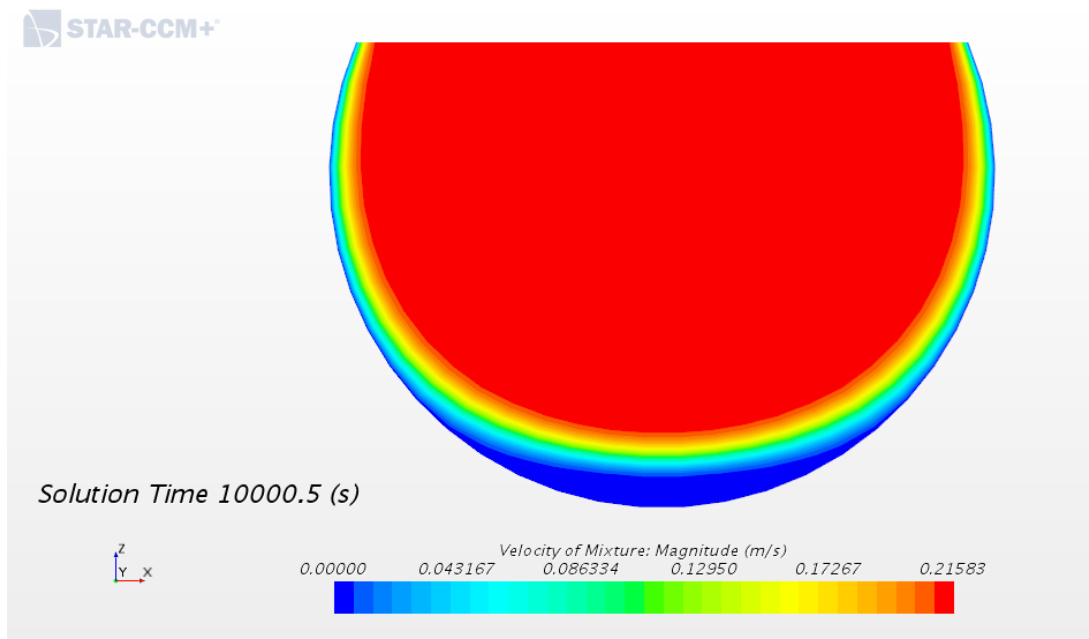


Figure 5.3: Contour plot for mixture velocity magnitude 14.5 m away from the channel inlet, perpendicular to the flow, for Case 12B

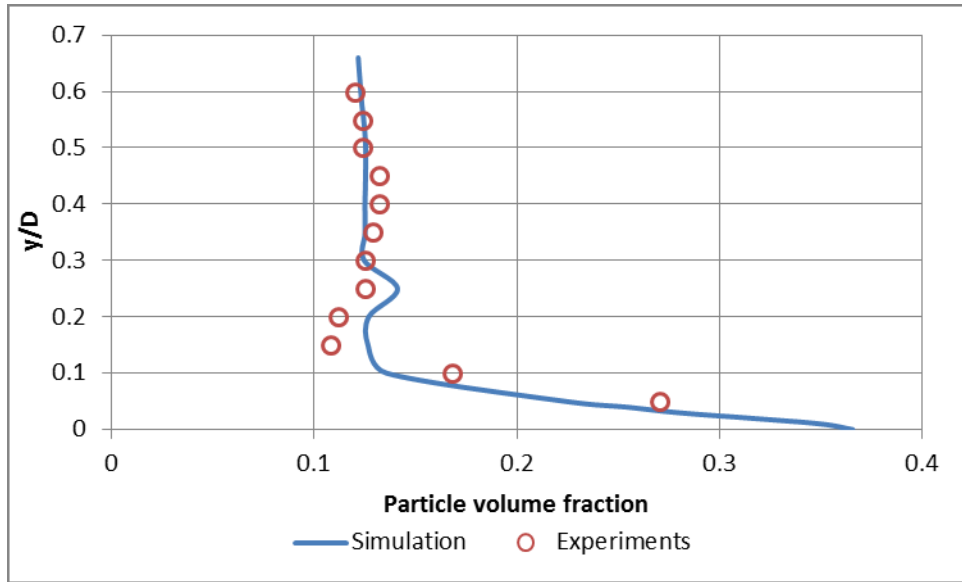


Figure 5.4: Chord-averaged particle volume fraction comparison between simulation results and experiments by Spelay¹⁷ for Case 12A

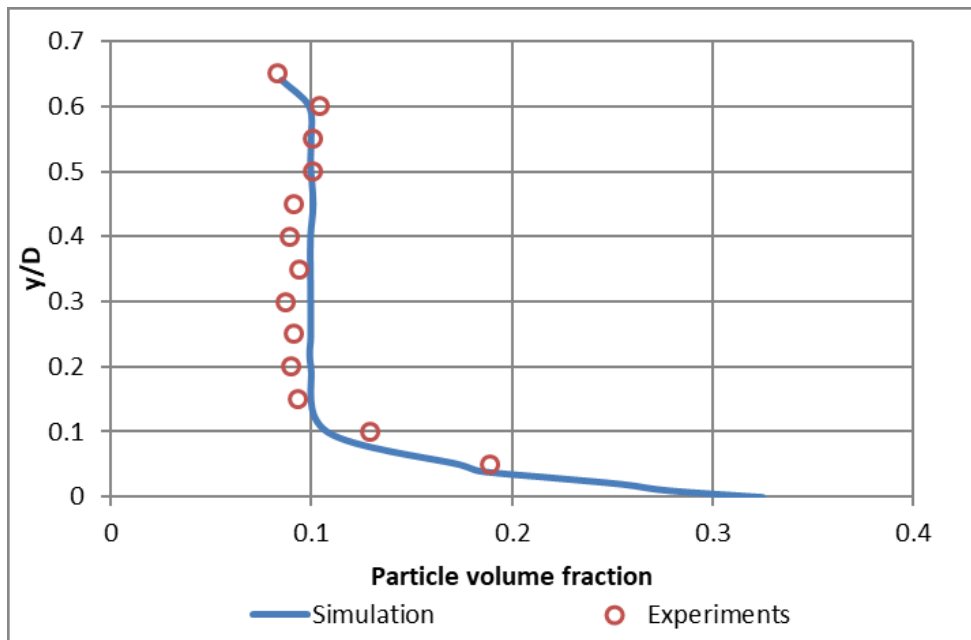


Figure 5.5: Chord-averaged particle volume fraction comparison between simulation results and experiments by Spelay¹⁷ for Case 12B

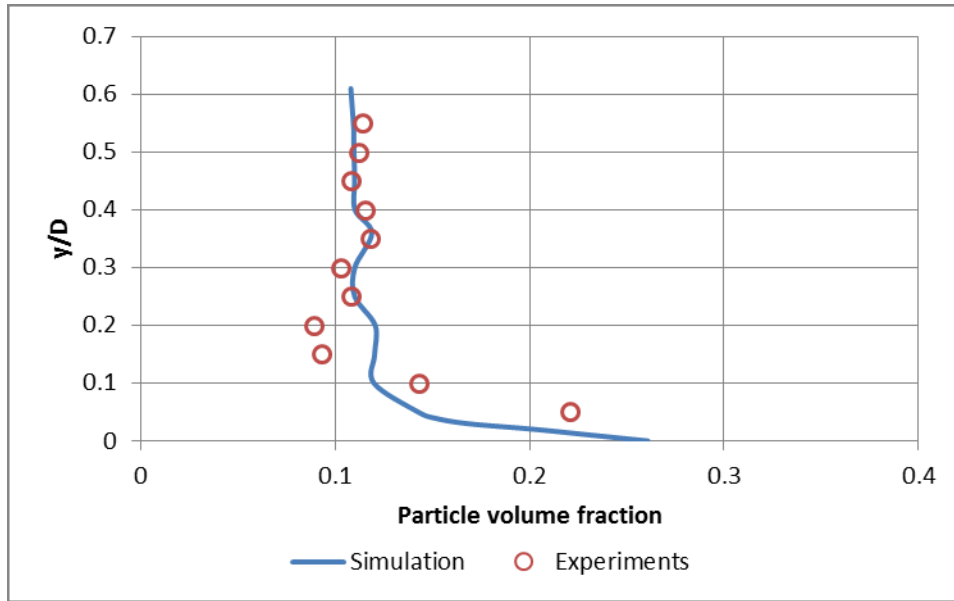


Figure 5.6: Chord-averaged particle volume fraction comparison between simulation results and experiments by Spelay¹⁷ for Case 12C

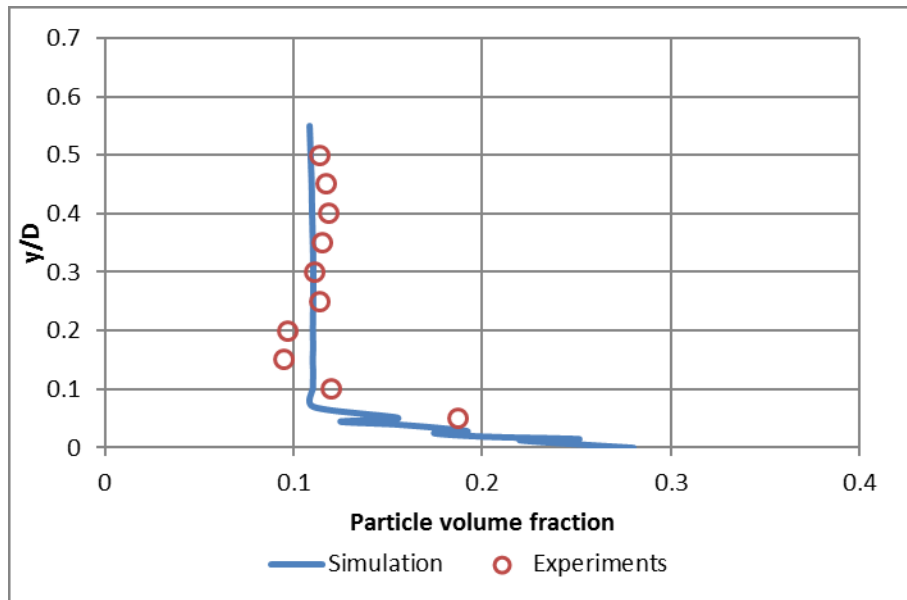


Figure 5.7: Chord-averaged particle volume fraction comparison between simulation results and experiments by Spelay¹⁷ for Case 12D

Figures 5.4 to 5.7 show good agreement between experiments and simulation data for the conditions in Table 5.2. However, in all cases there is a tendency for more scatter for $y/D < 0.2$ values, which can be associated with experimental uncertainties in the volume fraction de profiles and the fact the relative viscosity expressions proposed by Morris and Boulay²⁷

were developed for Newtonian carrier fluids. In addition, it should be noted that the particle surface roughness was not considered in the modelling conditions; the extent to which this could affect the simulation results is unknown.

An evaluation of the velocity field, shown in Figures 5.3 and 5.8, suggests the formation of a settled bed 14.5 m away from the channel inlet, where the apparent height of bed is approximately 7 mm or 40 particle diameters. The formation of a settled bed was seen by Spelay¹⁷ in his numerical results but it was not seen during experiments.

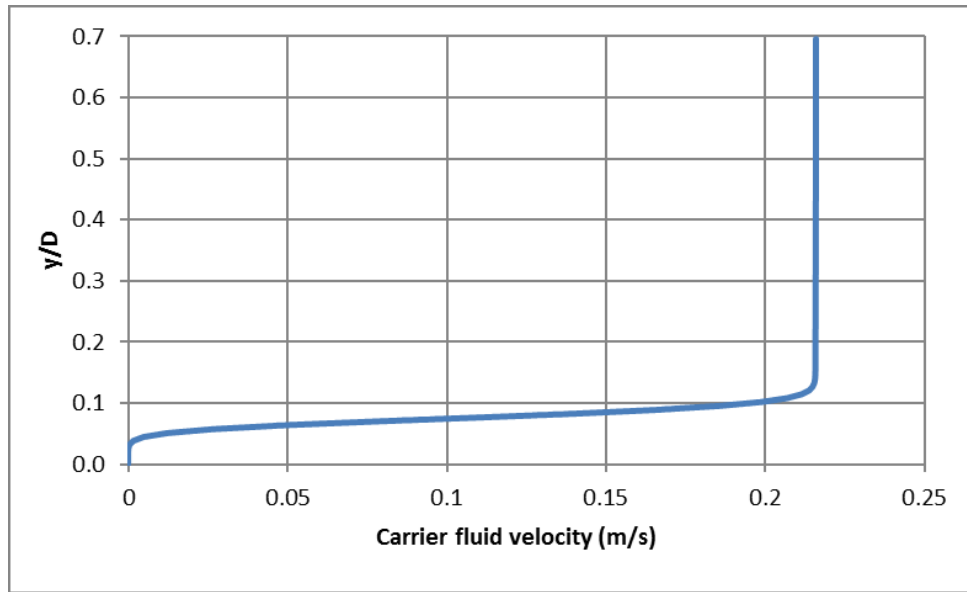


Figure 5.8: Simulated centerline velocity profile for the carrier fluid, 14.5 m away from the channel inlet, for Case 12B

The particle volume profile variation with time for Case 12B is shown in Figure 5.9. Because particles are added constantly to the flow domain, a steady-state particle volume fraction distribution could not be achieved during the simulations for up to 20,000 secs of solution time. Thus, the solution time was chosen as 10,000 s as the reference for further analysis. In addition, the particle volume fraction profiles shown in Figure 5.9 can be divided into regions: in the $0.6 < y/D \leq 0.7$ region, the particle volume fraction decreases with respect to $\phi_{s,bulk} = 0.1$, meaning there is particle depletion near the free surface; for $0.13 < y/D \leq 0.6$ values, the particle volume fraction stays constant to 0.1; at $y/D \leq 0.13$ is where the particle settling occurs, also, as seen in Figure 5.8, $y/D \sim 0.13$ is where the transition between the plug and sheared regions is located. This confirms that particle settling mostly occurs in the sheared region. However, the numerical results by Spelay¹⁷ showed a different behaviour, where the sheared region was divided into two sub-regions: a particle-rich

region near the wall with settled particles; and a particle-depleted zone where particles settled. In addition, his simulation results did not show particle settling from the plug region. Experimental studies are required to identify these regions and validate both models.

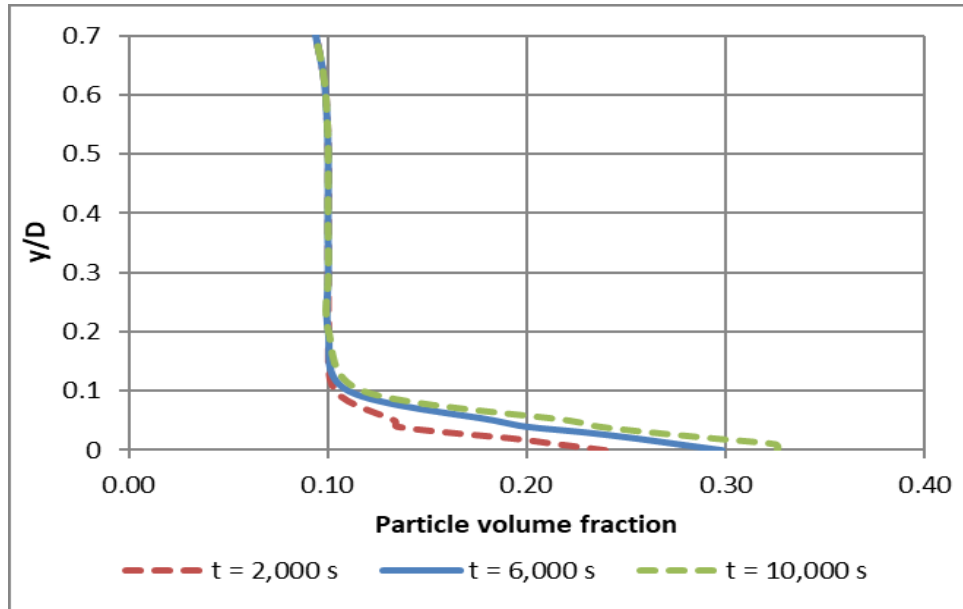


Figure 5.9: Particle volume fraction variation with time for case 10B

Furthermore, the variation of maximum particle volume fraction and maximum wall shear stress with position in the direction of the flow along the channel is shown as Figures 5.10 and 5.11, respectively. The maximum particle settling increases as the distance from the channel inlet increases, achieving a maximum at 16 m and then decreases again, which can be attributed to exit effects. Likewise, the maximum wall shear stress increases in a similar way to the maximum particle volume fraction. This is because as particles settle, their contribution to the wall shear stress increases as well.

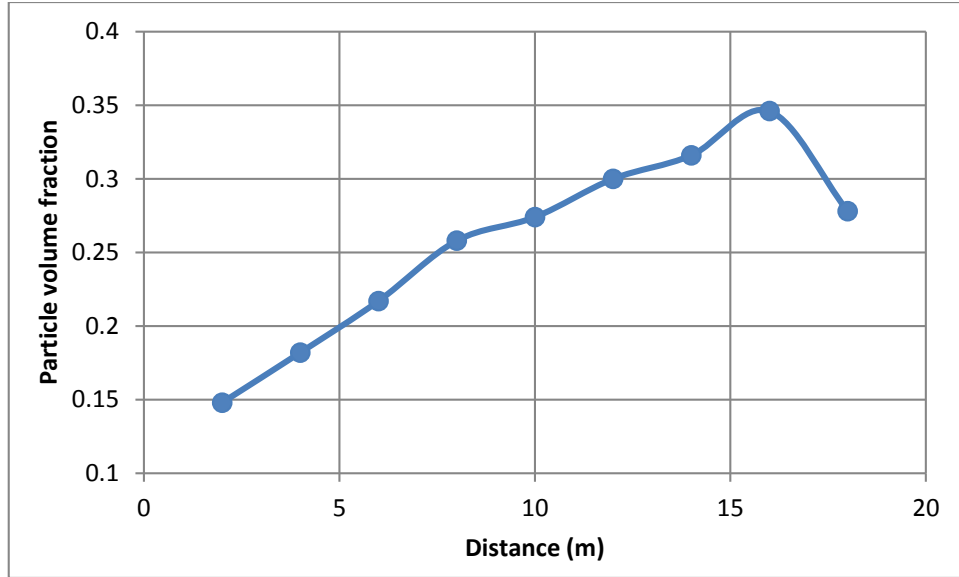


Figure 5.10: Simulated maximum particle volume fraction variation with distance from the inlet

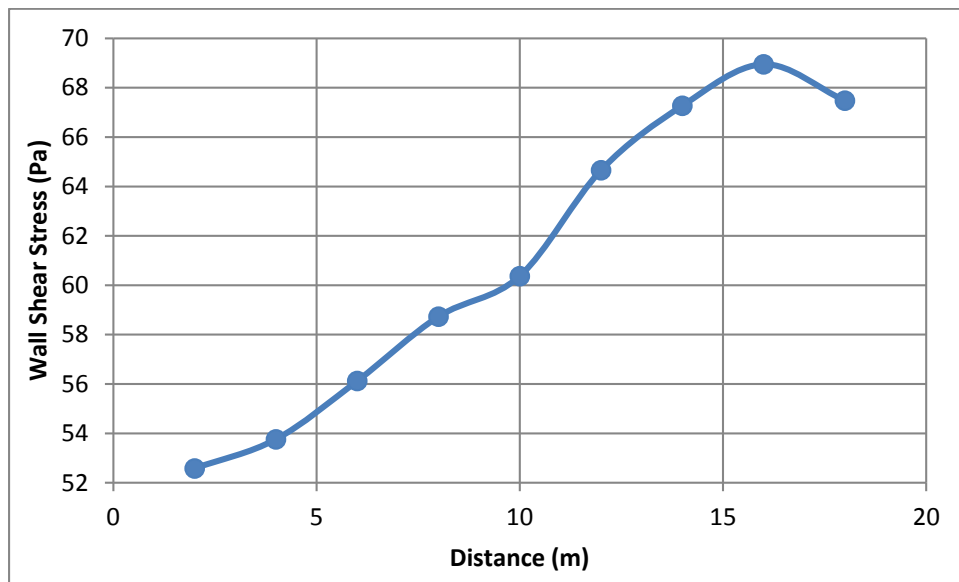


Figure 5.11: Simulated maximum wall shear stress variation with distance from the inlet

5.2 Parametric analysis

In order to determine which parameters have greater effect on coarse particle transport in viscoplastic fluids, it is necessary to perform a parametric analysis. For this, Case 12B was chosen as the base case because it was the most comparable to the experimental data. The effect of the variation of each parameter has on the particle volume fraction and velocity profiles will be discussed.

i. Carrier fluid yield stress

The carrier fluid yield stress was varied as $\pm 50\%$ of the base case; i.e. $\tau_{y-} = 20$ Pa and $\tau_{y-} = 60$ Pa. The results from these simulations are shown in Figures 5.12 and 5.13. Figure 5.12 shows there is little variation in the predicted particle volume fraction profile; i.e. less than 5% of variation for $y/D \sim 0$. Most variation occurs in the region $0.1 < y/D < 0.2$. In addition, Figure 5.13 shows increasing the yield stress has an offsetting effect on the velocity profile, but it is less than 3% different with respect to Case 12B. This can be explained by an increase in the apparent viscosity of the carrier fluid as the yield stress is increased; the inverse is true when the yield stress is decreased. It can be concluded that the yield stress, in the context of the numerical model, does not play a significant role on coarse particle settling, at least for the conditions studied here.

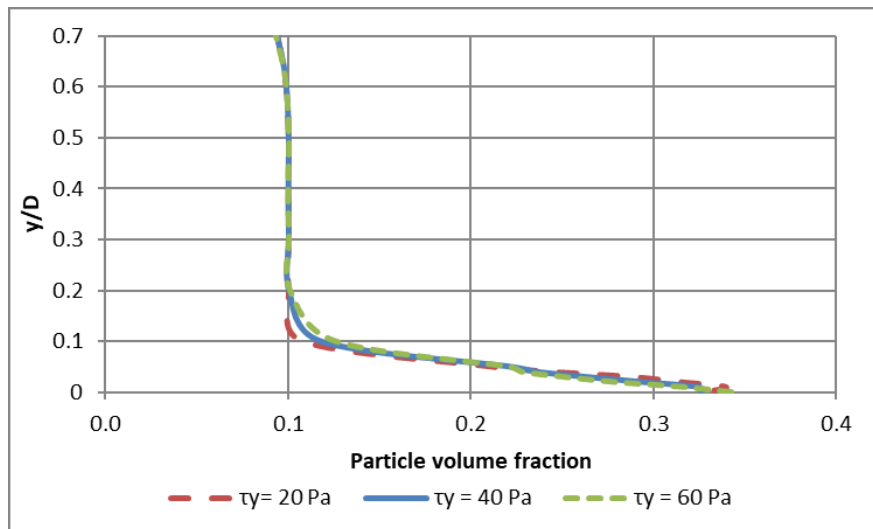


Figure 5.12: Chord-averaged particle volume fraction variation with carrier fluid yield stress

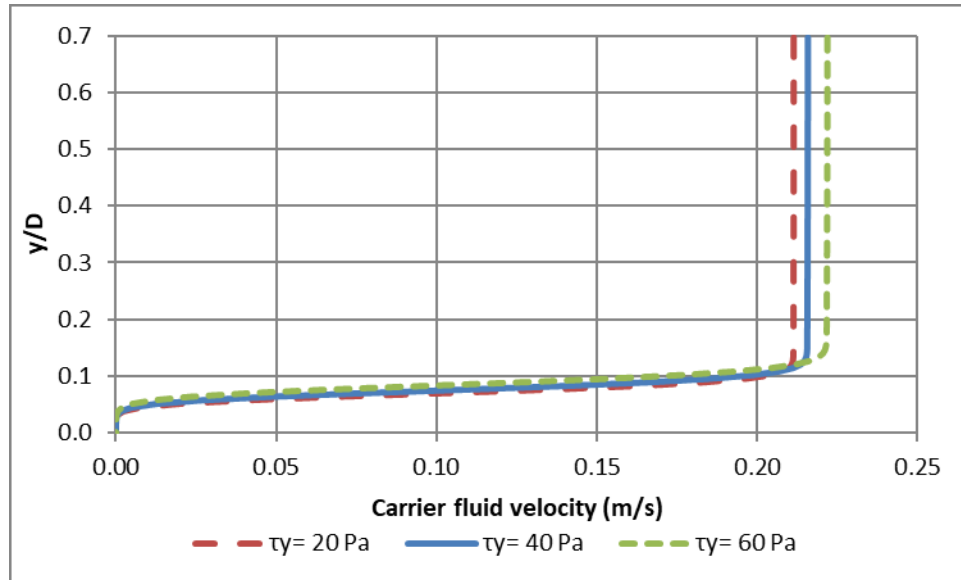


Figure 5.13: Predicted carrier fluid centerline velocity profile with varying carrier fluid yield stress

ii. *Flow geometry*

The impact of changing the channel geometry on particle settling was studied as follows:

- Channel diameter and depth of flow (i.e. keeping a constant h/D ratio)
- Channel diameter increase with constant depth of flow
- Replacement of the semi-circular channel with an equivalent rectangular channel

- Channel diameter

Scaling the channel diameter and the depth of flow by 50% has a minor effect on the normalized particle volume fraction and velocity profiles as shown in Figures 5.14 and 5.15. However, there is some variation for $0 \leq y/D \leq 0.04$ where the particle volume fraction at the wall increases by 16% when compared with the results from Case 12B. In addition, the height of the settled bed is increased from approximately 7 mm to 14 mm when the channel diameter is increased by 50%. These results suggest the model could be used for scaling purposes.

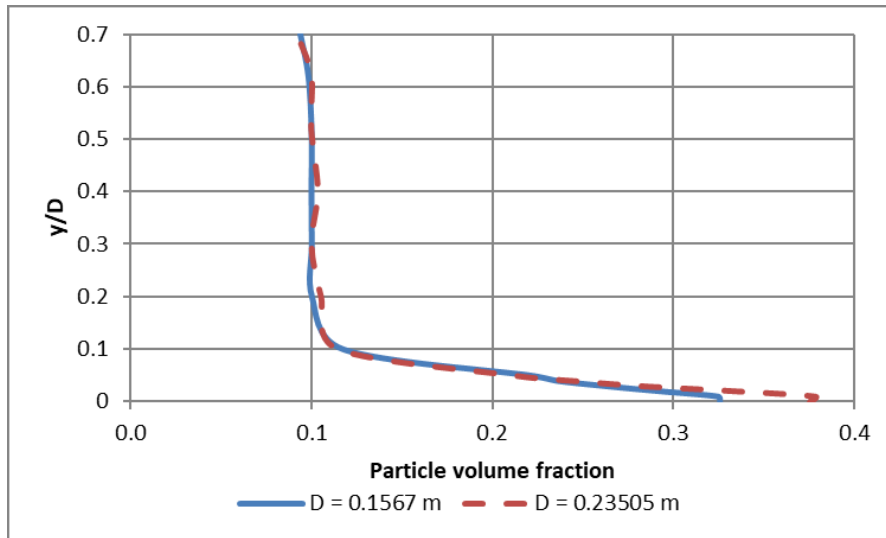


Figure 5.14: Chord-averaged particle volume fraction profile with varying channel diameter and depth of flow

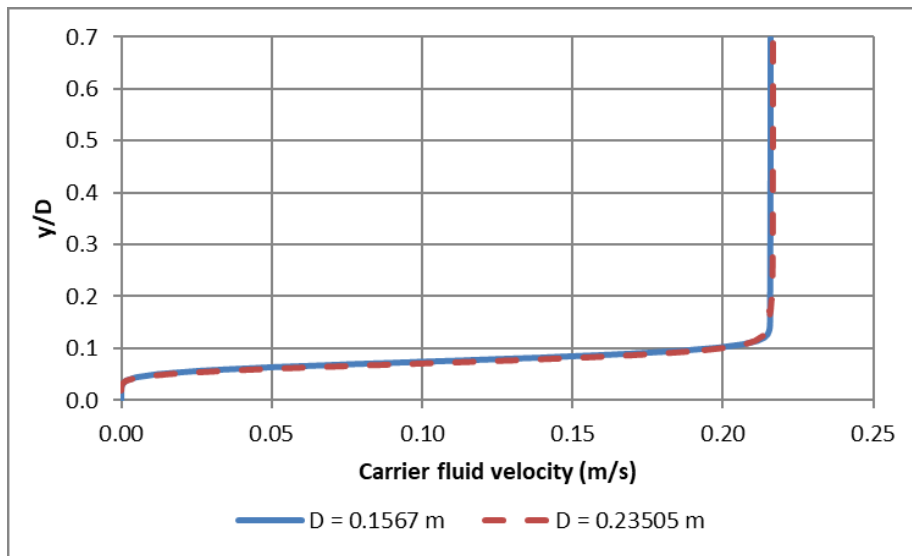


Figure 5.15: Predicted carrier fluid centerline velocity profile with varying channel diameter and depth of flow

When the diameter is increased while keeping a constant depth of flow, there is more wall area for particles to settle. Consequently, particle settling is increased by as much as 17% with respect to the base case. In addition, the height of the settled bed is increased from 7 mm to 9 mm, approximately. This is shown in Figures 5.16 and 5.17 by plotting the simulation data against a y/h for an equivalent comparison.

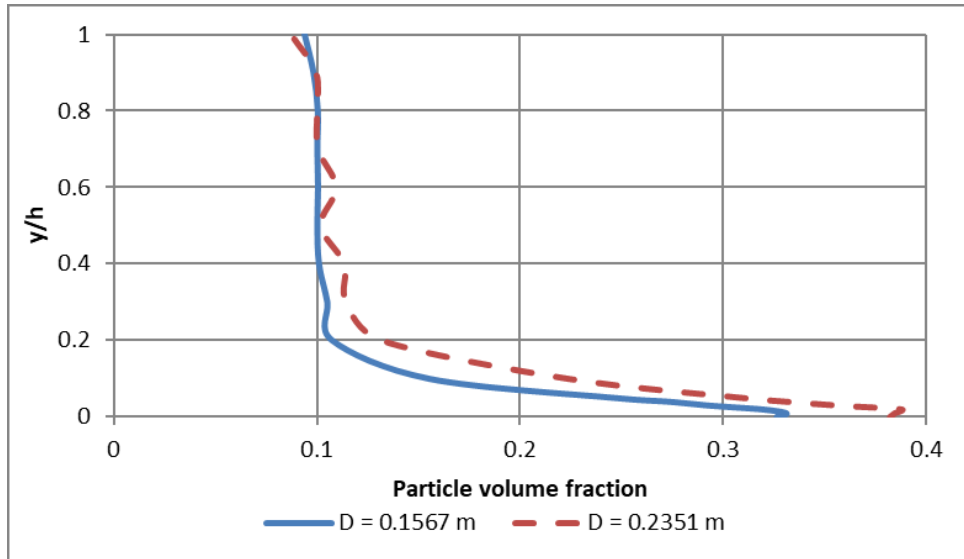


Figure 5.16: Chord-averaged particle volume fraction profile with varying channel diameter and constant depth of flow

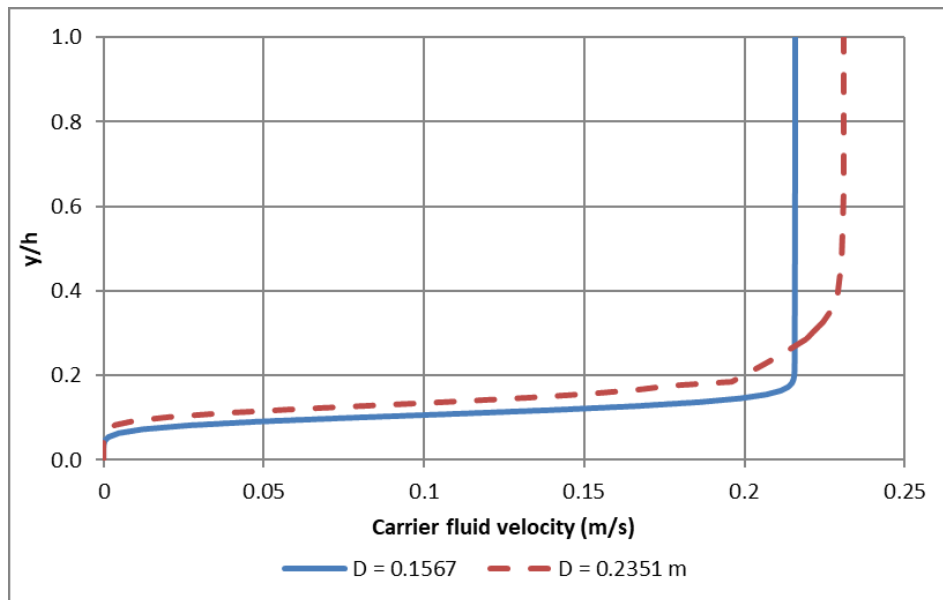


Figure 5.17: Predicted carrier fluid centerline velocity profile with varying channel diameter and constant depth of flow

- Rectangular channel

The channel geometry was changed to a rectangular channel of equivalent hydraulic radius as the semi-circular channel in Case 12B. Consequently, the dimensions of the rectangular channel are 0.1077 m in height (equivalent to the depth of flow) and 0.1614 m in width.

The comparison for the chord-averaged particle volume fraction and velocity profiles is shown in Figures 5.19 and 5.20, respectively.

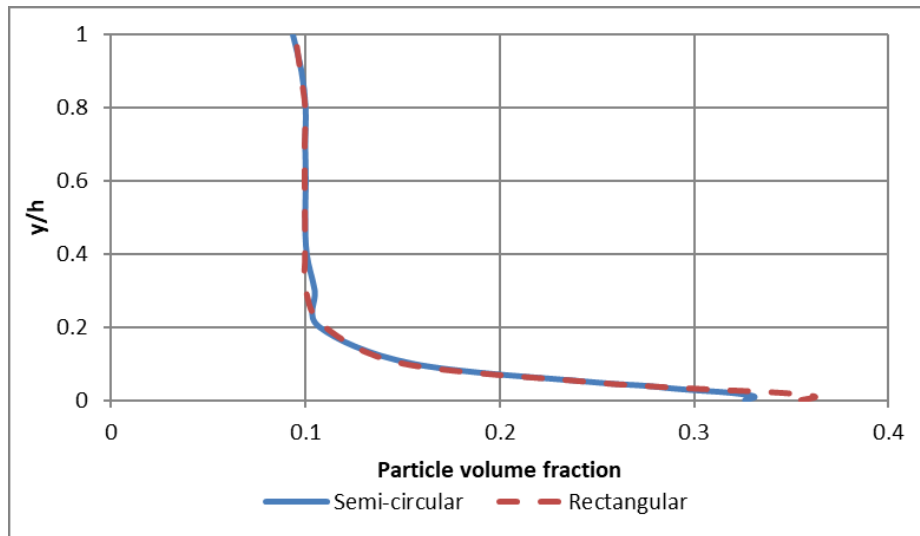


Figure 5.18: Chord-averaged particle volume fraction profile in a semi-circular and rectangular channel

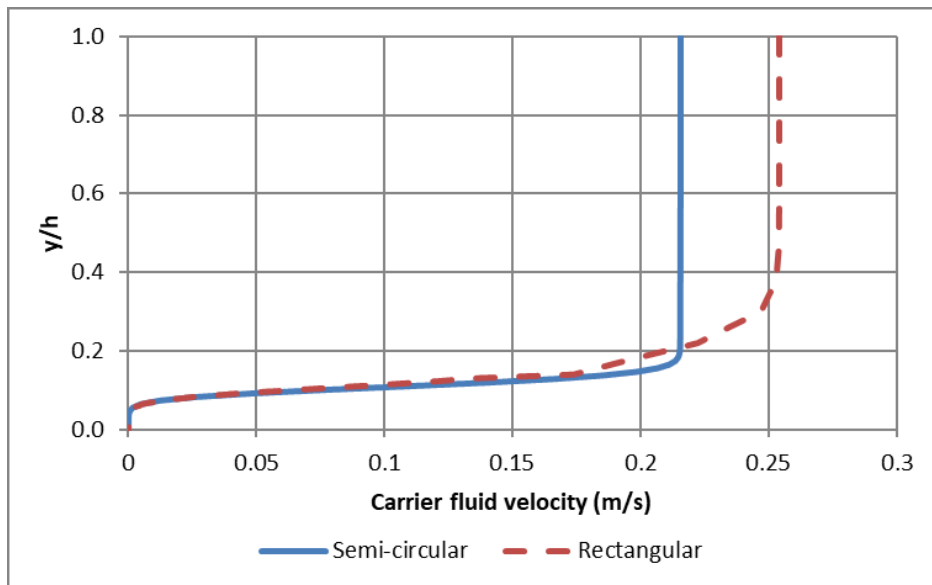


Figure 5.19: Predicted carrier fluid centerline velocity profile in a semi-circular and rectangular channel

In Figure 5.19, it is shown that the geometry variation has a minor effect on the chord-averaged particle volume profile; there is some variation, of about 9%, on the sedimentation front for $0 \leq y/D \leq 0.05$. However, Figure 5.19 shows a difference of 16% for

the velocity in the plug region when compared with the base case, while the height of the settled bed remains unchanged. To further analyze this, consider scalar scenes for the velocity of the particle phase shown in Figure 5.20. It can be seen that even though the height of the beds is similar, the area covered by the settled bed is larger for the rectangular channel, with an increase of about 270 % with respect to the base case. This shows the semi-circular channel is more efficient in transporting coarse particles under the studied conditions.

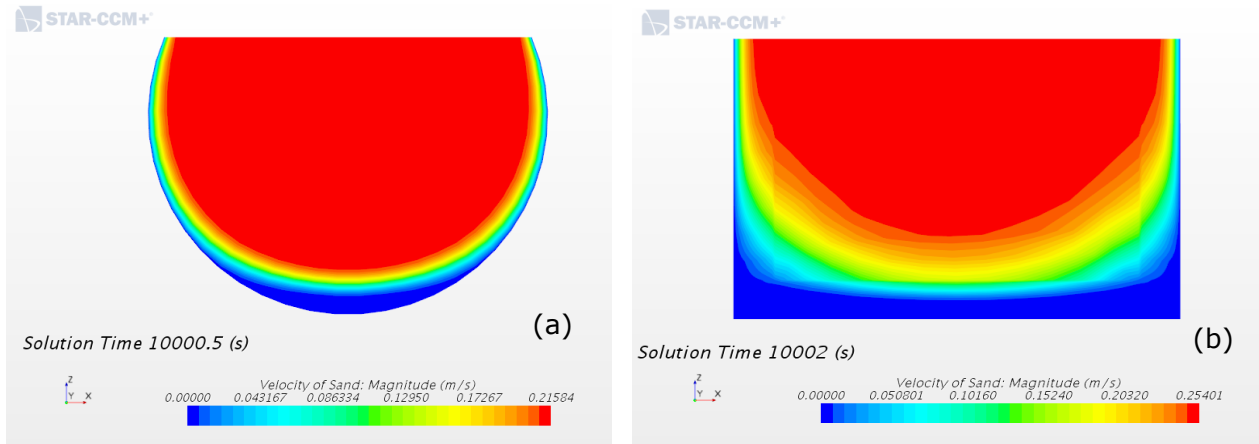


Figure 5.20: Contour plot for velocity of the particle phase 14.5 m away from the channel inlet in: (a) Semi-circular channel and (b) rectangular channel

Furthermore, Figure 5.21, shows a comparison between the shear stress distribution for the simulation results in the semi-circular and rectangular channel. It can be seen that in both cases, the minimum shear stress is found at the plug region. This region is larger in the semi-circular channel when compared to the rectangular channel. For the semi-circular channel, the maximum shear stress is found in the upper part of the channel, where the plug region transitions into the sheared region; and at the bottom of the channel. For the rectangular channel, the maximum shear stress is calculated near the bottom part of the lateral walls. The shear stress was calculated using a user-defined function: $\tau = \mu_{(\dot{\gamma})}\dot{\gamma}$, where $\mu_{(\dot{\gamma})}$ is the dynamic viscosity defined by Equation (2.68). The average wall shear stress was 57 Pa in the semi-circular channel and 54 Pa in the rectangular channel.

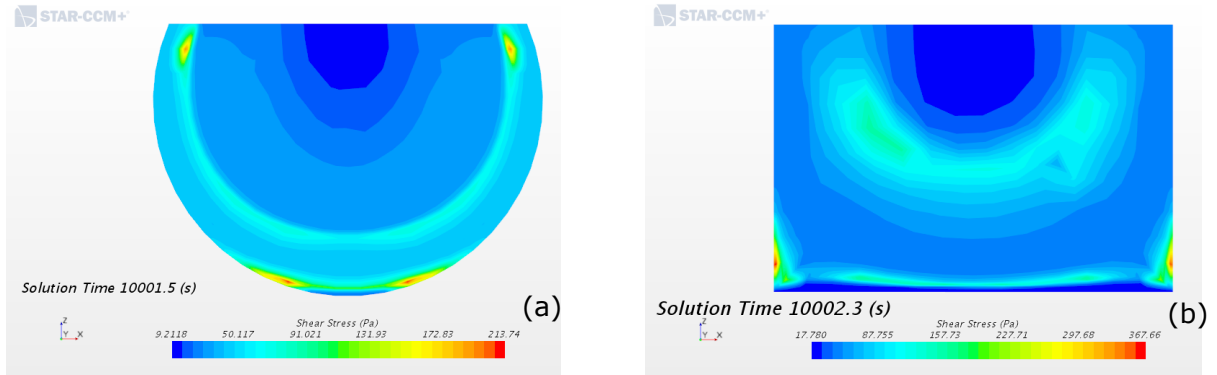


Figure 5.21: Contour plot for shear stress 14.5 m away from the channel inlet in: (a) Semi-circular channel and (b) rectangular channel

iii. Particle diameter

The particle diameter was increased to values 0.27 mm and 1 mm, to study the effect on particle settling. The resulting particle volume fraction profiles is shown as Figure 5.22 and the velocity profiles as Figure 5.23. While it has been shown the particle diameter does not have a significant effect on the suspension viscosity²⁴, it does have an effect on particle settling since, as shown in Section 2.4.1, the particle diameter is to the particle settling velocity. This is shown in Figure 5.22, when the particle diameter is increased to 0.27 mm, the chord-averaged volume fraction profile indicates slightly higher particle settling, with less than 5% difference close the wall. The settling is more pronounced when the particle diameter is increased to 1 mm, increasing the difference to up 19% close to the wall. The effect on the carrier fluid velocity profile is shown in Figure 5.23: there is no significant difference on the carrier fluid velocity when the particle diameter is increased to 0.27 mm. However, when the particle diameter is increased to 1 mm, the velocity at the core is increased to compensate for an increase of approximately 10 mm in the height of the settled bed.

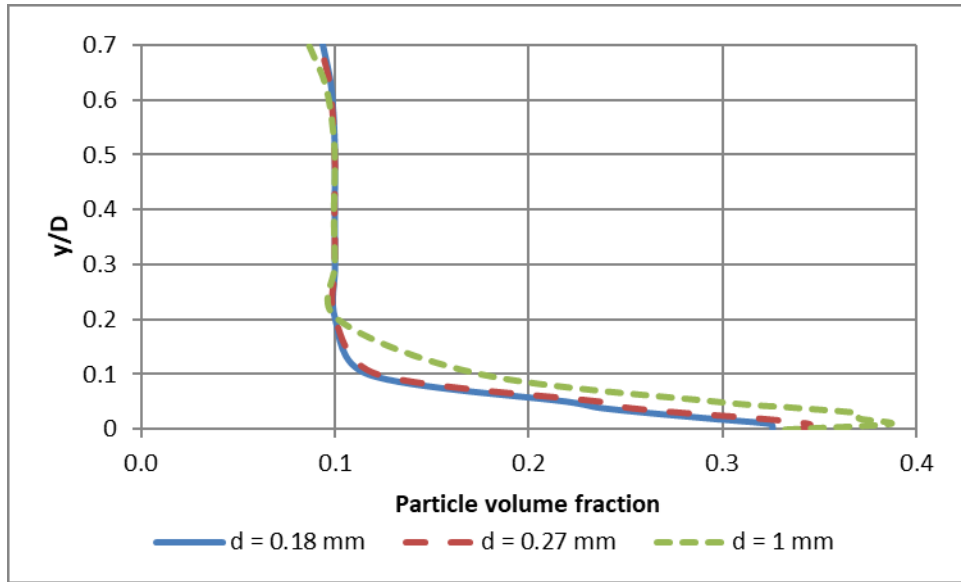


Figure 5.22: Chord-averaged particle volume fraction with varying particle diameter

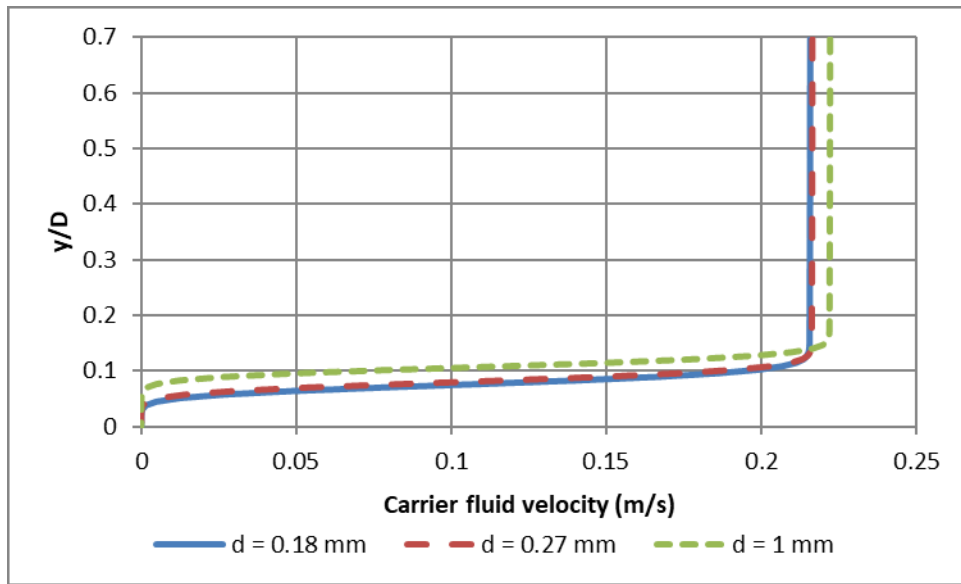


Figure 5.23: Predicted carrier fluid centerline velocity profile with varying particle diameter

iv. Bulk particle volume fraction

The bulk particle volume fraction of the suspension was increased to 0.2 and 0.3 v/v. The resulting particle volume fraction and velocity profiles are shown in Figures 5.24 and 5.26.

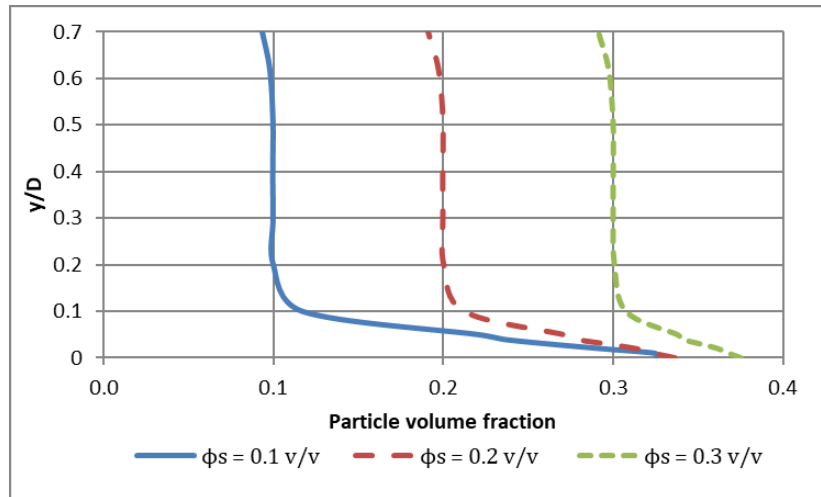


Figure 5.24: Chord-averaged particle volume fraction with varying particle volume fraction

As expected, increasing the particle volume fraction tends to hinder settling. Figure 5.24 shows the chord-averaged particle volume fraction profiles, for bulk volume fractions of 0.1 and 0.2 v/v the profiles tend to the same values as at y/D approaches zero. In addition, the deviation from the particle volume fraction at the core is higher for the 0.1 v/v case. To illustrate this point, the volume fraction profiles are normalized using the average particle volume fraction, as shown in Figure 5.25. As the bulk particle volume fraction is increased the deviation from the volume fraction of the plug decreases. The carrier fluid velocity profiles, shown in Figure 5.26, also show a decrease in size of the settled bed as the inlet particle volume fraction is increased.

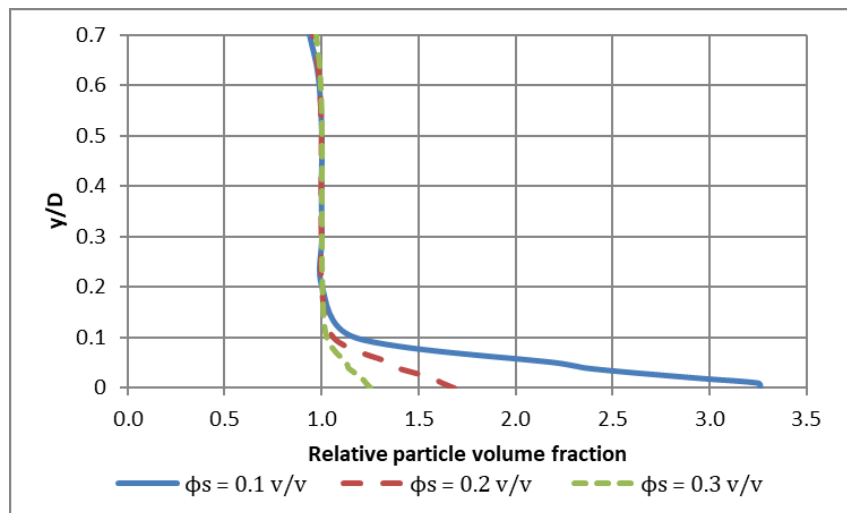


Figure 5.25: Relative particle volume fraction profiles with varying inlet particle volume fraction

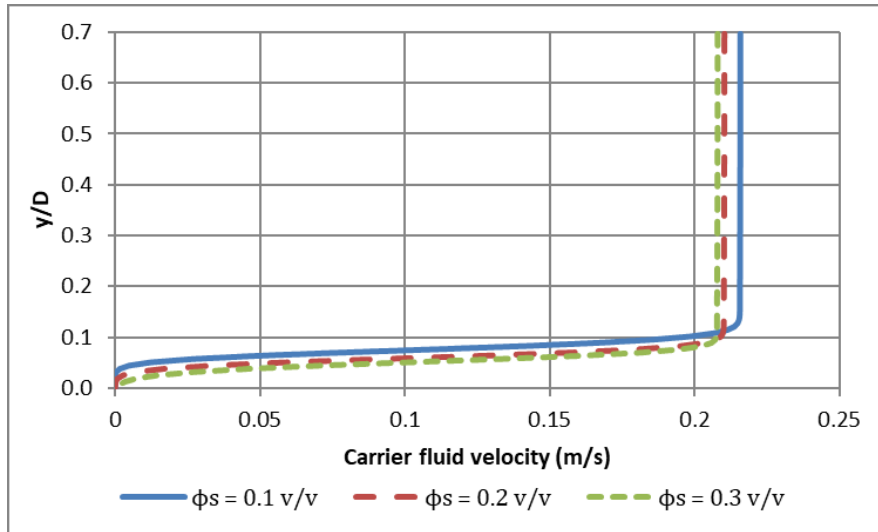


Figure 5.26: Carrier fluid velocity profiles with varying inlet particle volume fraction

v. *Mixture density*

The mixture density was increased to 1750 and 2000 kg/m³ to reduce the density difference between the carrier fluid and particles ($\rho_s = 2650$ kg/m³) and evaluate its impact on particle settling. The results are shown in Figure 5.27 and 5.28.

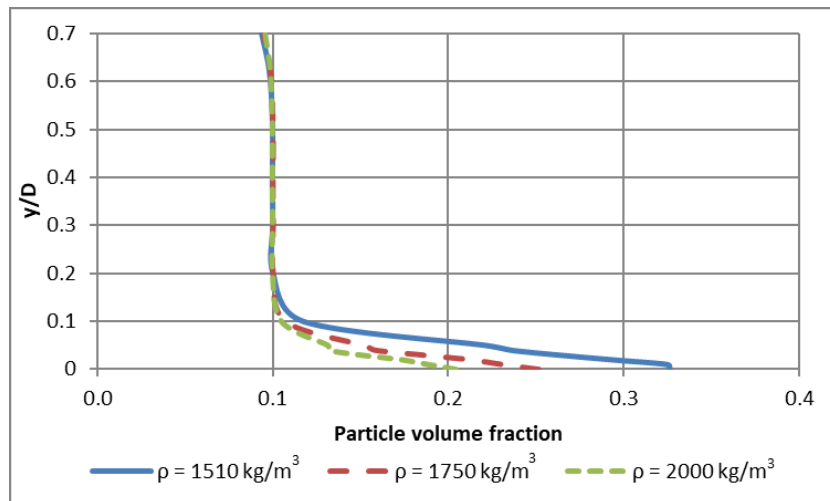


Figure 5.27: Chord-averaged particle volume fraction with varying carrier fluid density

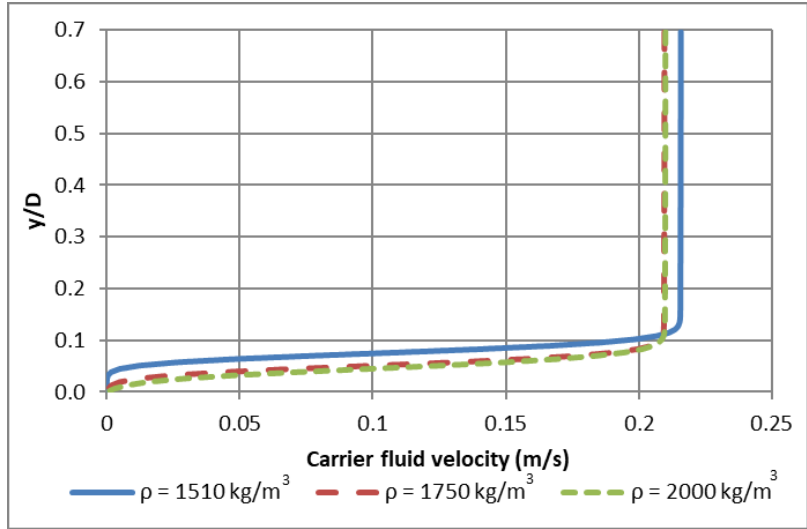


Figure 5.28: Predicted carrier fluid centerline velocity profile with varying carrier fluid density

Figure 5.27 shows that decreasing the mixture density hinders particle settling as the difference between the mixture and the solid density is decreased. Increasing the mixture density to 1750 kg/m³ decreases the particle volume fraction at the bottom wall by 23% whereas a further increase to 2000 kg/m³ decreases the maximum particle volume fraction by 37% with respect to the base case. In addition, Figure 5.28 suggests the disappearance of the settled bed by increasing the carrier fluid density to 1750 kg/m³, which offsets the velocity profile when compared with the base case because of the increase in the flow area.

vi. Flow rate

The flow rate was varied in increments of 50% with respect to Case 12B, and the resulting effects on particle volume fraction and centerline velocity profiles are shown in Figure 5.29 and 5.30. Increasing the flow rate to 3.75 L/s reduces the maximum particle settling by 11% with respect to Case 12B; further increasing the flow rate to 5 L/s reduces the maximum particle volume fraction by 24%. In addition, the normalized velocity profiles show more efficient particle transport by decreasing the apparent size of the settled bed.

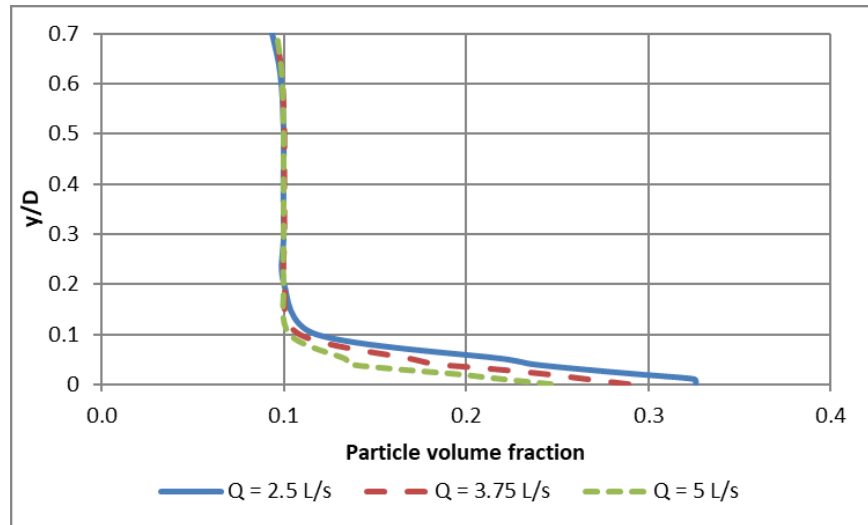


Figure 5.29: Chord averaged particle volume fraction profile with varying flow rate

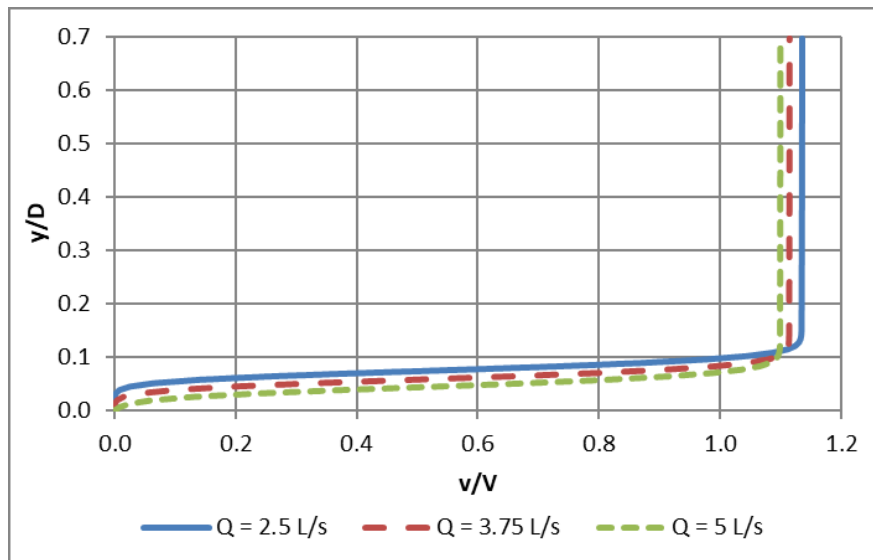


Figure 5.30: Normalized centerline velocity profile with varying flow rate

From the parametric analysis, it is shown the carrier fluid density, flow rate, and coarse particle volume fraction each play a major role in coarse particle settling; increasing one of these parameters can decrease particle settling significantly. However, the implications of changing these parameters must be considered to determine the best approach from an operational point of view. For example, increasing the coarse particle volume fraction might have effects in the erosion rate of the channel, increasing the carrier fluid density might not be beneficial for the rest of the process, since this would imply adding more particles to the system; furthermore, increasing the flow rate of the suspension is dependent on pump capacity and can affect erosion of the pipe walls. On the other hand, varying the yield stress

did not result in a significant change in coarse particle settling; and increasing the particle diameter had an increasing effect in particle settling. In terms of the geometry of the channel, the simulation results showed that scaling up both the diameter of the channel and the depth of flow was possible with particle volume fraction and velocity profiles unchanged; scaling the diameter of the channel while having a constant depth of flow as the base case, had an increasing effect in coarse particle settling because of an increase in the wall area for particles to settle; replacing the semi-circular channel by an equivalent rectangular channel had an increasing effect in the size of the area covered by the apparent settled bed. Other factors that can influence the particle transport is the length of the channel, and the time of operation as particles tend to accumulate.

5.3 Limitations

- The current model is limited to a constant depth of flow for a given simulation. Modelling three Eulerian phases requires significantly more time and computational power. Preliminary simulations including air-mixture-particle phases required many weeks or sometimes months to complete
- The solution was initialized with the boundary conditions to improve convergence and simulation time
- The validation of the model was limited to a small set of data from the experiments by Spelay¹⁷
- Turbulent effects were not considered in the modelling. As mentioned in Chapter 1, due to the high apparent viscosity of thickened tailings, it becomes cost-prohibitive to work under turbulent conditions
- The particle phase was modelled as monodisperse and smooth. Particle surface roughness was not considered and its effect on the simulation is unknown.
- The effect of particle concentration on yield stress and consistency parameters was not considered. The expressions by Ovarlez et al.⁸³ were considered in preliminary modelling but the results did not agree quantitatively with the experimental data from Spelay¹⁷
- The relative viscosity and normal viscosity was taken into account using the Morris and Boulay²⁷ model, which was developed for Newtonian carrier fluids
- The velocity profile predictions could not be validated against experimental data because of the lack of meaningful data due to the high apparent viscosity of the mixtures¹⁷

- The model does not account for microstructure changes in the mixture because of shear rate variation, as it was shown recently by Ovarlez et al.⁸³ during their experimental studies

5.4 Conclusions

- A numerical model was developed to predict coarse particle settling in the laminar, open-channel flow of non-Newtonian suspensions and successfully compared with experimental data. There was good agreement between the simulation results and the experiments by Spelay¹⁷ for the particle volume fraction distribution
- The simulated velocity profiles suggested the formation of a settled bed for the conditions that were studied
- A parametric analysis was performed to identify the major parameters affecting coarse particle settling. Increasing the yield stress had a minor effect on the simulated particle volume fraction and velocity profiles
- Increasing the channel diameter, while increasing the depth of flow (constant h/D values) had a minor effect on the particle volume fraction and velocity profiles. The height of the settled bed was increased with the scale up as well
- Increasing the channel diameter, while maintaining the depth of flow constant with respect of the base case, had an increase on the maximum particle volume fraction at the bottom of the channel. Consequently, the velocity profile changed to account for an increase in size of the settled bed, i.e. the velocity at the core increases
- Changing the flow geometry to a rectangular channel of equivalent hydraulic radius to the base had a minor effect on the shape of the particle volume fraction. However, there was a significant offset of the velocity profile. Closer inspection of the scalar scenes revealed that the cross-sectional area of the settled bed increased significantly in the rectangular channel when compared with the semi-circular channel results. Thus, a semi-circular channel is more efficient transporting coarse particles under the studied conditions
- Increasing the particle diameter had an increasing effect on coarse particle settling when evaluation the particle volume fraction profiles. The velocity profiles changed to account for an increase in particle settling
- Increasing the bulk particle volume fraction hindered particle settling. The particle volume fraction profiles were compared using a relative particle volume fraction, which showed the smaller the bulk volume fraction the more it deviates from the particle volume fraction at the plug region. Furthermore, the simulated velocity

profiles indicated a decrease in the apparent height of the settled bed with increasing particle volume fraction

- Increasing the carrier fluid density also had a hindering effect on coarse particle settling. Furthermore, the size of the settled bed decreases with increasing mixture density.
- Increasing the flow rate improves the transport of coarse particles, by decreasing the particle settling at the bottom of the channel. This is also shown in the velocity profiles where there is no indication of settled bed.
- Of the parameters studied, flow rate, carrier fluid density, and particle volume fraction were the ones which had the most significant impact on coarse particle settling. Considerations should be taken on how these parameters affect other integral parts of the process, such as channel erosion, pump capacity, and friction losses

5.5 Recommendations

The following studies are recommended to improve the modelling of non-Newtonian suspensions:

- Develop experimental techniques to study the presence of a settled bed more accurately. This will improve the validation of the model
- Develop experimental studies to evaluate microstructure changes in water-clay-sand mixtures as this would improve our understanding in the area and develop models that can account for this effect properly
- Validate the expressions developed by Ovarlez et al.⁸³ to account for the particle volume fraction effect on yield stress and consistency index using water-clay-sand mixtures so they can be incorporated in the modelling stage of these suspensions
- Study the effect of particle surface roughness on the rheological parameters and flow characteristics, to evaluate to what extent this difference affects the velocity field in viscoplastic carrier fluids
- Continue developing the CFD model to include air, clay-water mixture, and solid particle phases as advances in software and hardware become available
- Perform experiments where the velocity distribution of clay-water-sand mixtures can be measured to further validate the model

6. Conclusions and recommendations for future work

6.1 Summary and conclusions

The primary goal of this project was to develop a model, using a commercially-available CFD software, to predict the flow behaviour of non-Newtonian suspensions under laminar, open-channel flow conditions. This was achieved by first validating STAR-CCM+ modelling capabilities in less complex cases. First, the ability of the model to predict depth of flow, wall shear stress, and velocity field of homogeneous, non-Newtonian mixtures was validated against experimental data^{17,45}, as shown in Chapter 3. In Chapter 4, shear-induced migration, single-particle settling, and laminar transport of settling slurries were studied separately and compared with experimental data^{29,32,35}. Lastly, in Chapter 5, the transport of monodisperse coarse particles suspended in viscoplastic fluids was modelled and compared against experimental data¹⁷. After a thorough validation, it was possible to study several modelling conditions, that would be otherwise difficult and expensive with experiments to determine efficient approaches to coarse particle transport using non-Newtonian fluids.

The main findings of this project are summarized as follows:

- The model developed using STAR-CCM+, for the laminar, open-channel flow of non-Newtonian fluids can successfully predict the depth of flow, wall shear stress, and velocity field when compared with experimental data from Spelay¹⁷. Also, the local mixture velocity was studied further by using the laminar sheet flow model⁴⁴, to address some of the discrepancies observed earlier during the studies, as shown in Section 3.2. The simulation results were used to calculate the Fanning friction factor and compare it with an available correlation⁵³ with excellent agreement. The model presented in Chapter 3 can be used to study the behaviour of these mixtures under a wide range of conditions.
- Shear-induced migration of neutrally-buoyant particles suspended in a Newtonian fluid, was modelled using the normal viscosity approach in Chapter 4, which was compared with experimental data by Hampton et al.²⁹. The simulation results showed migration towards the center of the tube because of gradients in shear rate. However, the model is not able to predict particle-wall collisions, which caused a depletion of the particle volume fraction at the walls in the experiments
- Single-particle settling through viscoplastic fluids was modelled implementing two different correlations. The correlation by Shokrollahzadeh³⁵, which uses an

“equivalent Newtonian viscosity” to account for the dynamic viscosity of the viscoplastic fluids proved to be the better of the two, for the evaluated conditions shown in Section 4.2. While the model is in good agreement with experimental data³⁵, it suffers from the same limitations as the correlation; i.e., there is significant scatter of the results with respect of the Newtonian Drag curve as $Re^* < 50$

- The laminar pipeline transport of settling was modelled as preliminary studies of monodisperse coarse particle settling. While the simulation results capture the overall behaviour of particle settling in Newtonian slurries when compared to the experimental data of Gillies et al.³², there were some discrepancies in the particle volume fraction profiles. This was associated with the stability of the solver as the particle volume fraction reached the maximum packing fraction in the flow domain. In addition, the velocity profiles showed an asymmetry with respect of the center of the pipe that is characteristic of particle settling and asymmetric particle concentration profiles
- In Chapter 5, a model was developed to study monodisperse coarse particle settling in non-Newtonian fluids under laminar, open-channel flow. The simulated volume fraction profiles were compared successfully with experimental data from Spelay¹⁷. The simulation results showed that particles settle predominantly in the sheared zone where they form a stationary bed. The maximum particle volume fraction and maximum wall shear stress were found 16 m away from the channel inlet
- A parametric analysis involving the mixture yield stress, channel geometry, particle diameter, particle volume fraction, mixture density, and flow rate was performed. The results showed that increasing flow rate, particle volume fraction, and the density of the suspending fluid are the parameters which have a greater hindering effect on coarse particle settling. Also, the simulation results showed that the model can be used for scaling purposes

6.2 Recommendations for future work

The following studies are proposed to improve the model and the knowledge of non-Newtonian suspensions:

- Perform reliable, high-quality measurements of local velocities of viscoplastic fluids flowing through an open channel. A comparison with additional experimental data, maintaining $Re_H < 1000$ and using mixtures with a wide range of yield stresses, for example 2-40 Pa, could help to address some of the discrepancies observed in some of the modelling results. In addition, if a Pitot tube is used in conjunction with

another measurement method, such as ultrasonic velocity profiling (UVP), one could validate or disprove the assumptions made for the Pitot tube local velocity measurements for viscoplastic fluids

- Study the ability of the Multiphase segregated model, described in Section 2.6.2, to model the homogeneous, laminar, open-channel flow of non-Newtonian fluids. This will allow to study the air and mixture phases separately and make it easier for the user to extract the desired results
- Study in more detail the wall effects in particle volume fraction profiles of neutrally buoyant particle in a tube. Discrete Element Method (DEM) studies can be done to account for particle-wall collisions, which can aid in the development of more accurate models in an Eulerian framework
- Study the mechanism(s) that govern particle settling in viscoplastic fluids when $Re^* < 50$, as that is would provide more insight for modelling purposes. For example, particle-level numerical studies, using DEM or Lattice-Boltzmann, can be performed to study the drag around a sphere as they settle in a viscoplastic fluid in more detail
- Develop experimental protocols to characterize and evaluate microstructure changes in water-clay-sand mixtures under shear, as it has been shown the microstructure of viscoplastic suspensions is shear-dependent, while the model assumes a constant microstructure. Ovarlez et al.⁸³ used a rheo-X-microtomography setup to study the microstructure of polystyrene particles suspended in a concentrated emulsion, a similar setup could be used to study sand-clay-water mixtures
- Study the effect of particle surface roughness in the rheological parameters and flow characteristics. This would provide more insight in how surface roughness affects the flow field as this was not considered in the modelling. Ovarlez et al.⁸⁹ used nuclear magnetic resonance (NMR) to measure the local particle volume fraction and local suspension velocities in a Couette geometry. A similar setup can be used to characterize neutrally-buoyant suspensions with rough and smooth particles
- Continue developing the CFD model to include air, clay-water mixture, and solid particle phases at the same time in the calculation of the flow behaviour of non-Newtonian suspensions, as advances in software and hardware become available, as this was one of the challenges during this study. This can provide with more applications for the model, such as the prediction of the slope of the deposit once the thickened tailings have been disposed.

References

- (1) National Energy Board. 2016 Estimated Production of Canadian Crude Oil and Equivalent <https://www.neb-one.gc.ca/nrg/sttstc/crdlndptrlmprdct/stt/stmtdprdctn-eng.html> (accessed Apr 21, 2017).
- (2) Government of Alberta. Alberta Energy Facts <http://www.energy.alberta.ca/oilsands/791.asp> (accessed Apr 21, 2017).
- (3) Masliyah, J. H.; Czarnecki, J.; Xu, Z. Colloidal Science in Tailings Management. In *Handbook on Theory and Practice of Bitumen Recovery from Athabasca Oil Sands*; Kingsley Knowledge Publishing, 2011; p 392.
- (4) Boger, D. V. Rheology and the resource industries. *Chem. Eng. Sci.* **2009**, *64* (22), 4525–4536.
- (5) Oil Sands Magazine. MINING FOR BITUMEN <http://www.oilsandsmagazine.com/technical/mining> (accessed Jun 23, 2017).
- (6) Alberta Energy. About Oil Sands <http://www.energy.alberta.ca/OilSands/791.asp> (accessed Jun 23, 2017).
- (7) Government of Alberta. Alberta's Tailings Management Framework <https://www.aer.ca/about-aer/spotlight-on/alberta-tailings-managment-framework> (accessed Aug 27, 2017).
- (8) Alberta Energy Regulator. Directive 085 <https://www.aer.ca/rules-and-regulations/directives/directive-085> (accessed Aug 27, 2017).
- (9) Canada's Oil Sands Innovation Alliance. About COSIA <http://www.cosia.ca/about-cosia> (accessed Apr 21, 2017).
- (10) Canadian Natural Ltd. *Horizon Oil Sands Application for tailings management plan (TMP)*; 2016.
- (11) Shell Canada Energy. *Muskeg River Mine Fluid Tailings Management Plan*; 2016.
- (12) Shell Canada Energy. *Jackpine Mine Fluid Tailings Management Plan*; 2016.
- (13) Imperial Oil Resources Ventures Limited. *Kearl Oil Sands Tailings Management Plan*; 2016.

- (14) Suncor Energy. Report on Sustainability 2017 <https://sustainability.suncor.com/2017/en/environment/tailings-management.aspx> (accessed Aug 28, 2017).
- (15) Syncrude. *Tailings Management Plan Application Syncrude Aurora North Mine*; 2016.
- (16) Sun, R.; Goldszal, A.; Li, C. Optimizing the capture of oil sand fines in sand beach area. In *Proceedings of the International Oil Sands Tailings Conference*; Edmonton, Canada, 2012.
- (17) Spelay, R. B. SOLIDS TRANSPORT IN LAMINAR, OPEN CHANNEL FLOW OF NON-NEWTONIAN SLURRIES, University of Saskatchewan, 2007.
- (18) Shook, C. A.; Gillies, R. G.; Sanders, R. S. *Pipeline Hydrotransport with Applications in the Oil Sand Industry*; SRC Pipe Flow Technology Centre: Saskatoon, SK, 2002.
- (19) Sumner, R. S.; Munkler, J. J.; Carriere, S. M.; Shook, C. A. Rheology of Kaolin Slurries Containing Large Silica Particles. *J. Hydrol. Hydromechanics* **2000**, *48* (2), 110–124.
- (20) Chhabra, R. P.; Richardson, J. F. *Non-Newtonian Flow in the Process Industries, Fundamentals and Engineering Applications*, 1st ed.; Butterworth Heinemann: Oxford, 1999.
- (21) Tu, J.; Yeoh, G. H.; Liu, C. *Computational fluid dynamics: a practical approach*, 1st Editio.; Butterworth Heinemann: Amsterdam, 2008.
- (22) Treinen, J. M.; Cooke, R. Energy induced rheology reduction of flocculated slurries. In *Proceedings of the 18th International Conference on Hydrotransport*; BHR Group: Rio de Janeiro, Brazil, 2010; p 487.
- (23) Balmforth, N. J.; Frigaard, I. A.; Ovarlez, G. Yielding to Stress: Recent Developments in Viscoplastic Fluid Mechanics. *Annu. Rev. Fluid Mech.* **2014**, *46* (1), 121–146.
- (24) Mewis, J.; Wagner, N. J. *Colloidal Suspension Rheology*; Varma, A., Ed.; Cambridge University Press: New York, 2012.
- (25) Krieger, I. M.; Dougherty, T. J. A mechanism of non-Newtonian flow in suspensions of rigid spheres. *Trans Soc Rheol* **1959**, *3*, 137.
- (26) Krieger, I. M. Rheology of monodisperse latices. *Adv Colloid Interface* **1972**, *3*, 111.

- (27) Morris, J. F.; Boulay, F. Curvilinear flows of noncolloidal suspensions: The role of normal stresses. *J. Rheol. (N. Y. N. Y)*. **1999**, *43* (5), 1213.
- (28) Leighton, D.; Acrivos, A. The shear-induced migration of particles in concentrated suspensions. *J. Fluid Mech.* **1987**, *181*, 415–439.
- (29) Hampton, R. E.; Mammoli, A. a.; Graham, A. L.; Tetlow, N.; Altobelli, S. a. Migration of particles undergoing pressure-driven flow in a circular conduit. *J. Rheol. (N. Y. N. Y)*. **1997**, *41* (3), 621.
- (30) Phillips, R. J.; Armstrong, R. C.; Brown, R. A.; Graham, A. L.; Abbott, J. R.; Phillips, R. J.; Armstrong, R. C.; Brown, R. A.; Graham, A. L.; Abbott, J. R. A constitutive equation for concentrated suspensions that accounts for shear - induced particle migration A constitutive equation for concentrated for shear-induced particle migration suspensions that accounts. *Phys. Fluids* **1992**, *30*, 30–40.
- (31) Richardson, J. F.; Zaki, W. N. Sedimentation and fluidization. *Trans. Inst. Chem.* **1954**, *35*, 32.
- (32) Gillies, R. G.; Hill, K. B.; McKibben, M. J.; Shook, C. A. Solids transport by laminar Newtonian flows. *Powder Technol.* **1999**, *104* (3), 269–277.
- (33) Treinen, J. M.; Jacobs, J. The Applicability of The Eulerian-Eulerian CFD Approach Using Granular Kinetic Theory to Predict Particle Settling and Migration in Viscoplastic Fluids. In *17th International Conference on Transport and Sedimentation of Solid Particles*; Sobota, J., van Rhee, C., Eds.; Wroclaw: Delft, The Netherlands, 2015; pp 345–354.
- (34) Sittoni, L.; Talmon, A.; van Kester, J.; Uittenbogaard, R. Latest numerical developments for the prediction of beaching flow and segregating behavior of thick Non-Newtonian mixtures. In *17th International Conference on Transport and Sedimentation of Solid Particles*; Sobota, J., van Rhee, C., Eds.; Wroclaw: Delft, The Netherlands, 2015; pp 309–316.
- (35) Shokrollahzadeh, A. Terminal Settling Velocity of a Sphere in a non-Newtonian Fluid, University of Alberta, 2015.
- (36) Straub, L. G.; Silberman, E.; Nelson, H. C. Open channel flow at small Reynolds numbers. *Trans ASCE* **1958**, *123*, 685–706.

- (37) Chow, V. Te. *Open-channel hydraulics*; McGraw-Hill: New York, 1959.
- (38) White, F. *Fluid Mechanics*, 8th editio.; McGraw-Hill: New York, 2016.
- (39) Haeri, S.; Hashemabadi, S. H. Experimental Study of Gravity-Driven Film Flow of Non-Newtonian Fluids. *Chem. Eng. Commun.* **2008**, *196* (5), 519–529.
- (40) Slatter, P.; Haldenwang, R.; Chhabra, R. P. The Sheet Flow Viscometer. In *Proceedings of the 18th Conference on the Hydraulic Transport of Solids*; BHR Group Ltd: Rio de Janeiro, 2010; pp 299–307.
- (41) Astarita, G.; Marrucci, G.; Palumbo, G. Non-Newtonian Gravity Flow Along Inclined Plane Surfaces. *I E Fundam.* **1964**, *3* (4), 333–339.
- (42) Coussot, P.; Proust, S. Slow, unconfined spreading of a mudflow. *J. Geophys. Res.* **1996**, *101* (B11), 25217–25229.
- (43) Coussot, P. Steady, laminar, flow of concentrated mud suspensions in open channel. *J. Hydraul. Res.* **1994**, *32* (4), 535–559.
- (44) DE KEE, D.; CHHABRA, R. P.; POWLEY, M. B.; ROY, S. Flow of Viscoplastic Fluids on an Inclined Plane: Evaluation of Yield Stress. *Chem. Eng. Commun.* **1990**, *96* (1), 229–239.
- (45) Haldenwang, R.; Kotzé, R.; Chhabra, R. Determining the viscous behavior of non-newtonian fluids in a flume using a laminar sheet flow model and Ultrasonic Velocity Profiling (UVP) system. *J. Brazilian Soc. Mech. Sci. Eng.* **2012**, *34* (3), 276–284.
- (46) Alderman, N. J.; Haldenwang, R. A review of Newtonian and non-Newtonian flow in rectangular open channels. In *Proceedings of the 17th International on the Hydraulic Transport of Solids*; BHR Group Ltd: Cape Town, 2007.
- (47) Haldenwang, R.; Slatter, P. Experimental procedure and database for non-Newtonian open channel flow. *J. Hydraul. Res.* **2006**, *44* (2), 283–287.
- (48) Kozicki, W.; Tiu, C. Parametric modelling of flow geometries in non-Newtonian flows. *Encyclopedia of Fluid Mechanics*; Gulf Publishing Co, 1986; pp 199–252.
- (49) Zhang, H.; Ren, Z. Discussion of resistance of hyperconcentrated flow in open channels. *Sci. Sin. (Series A)* **1982**, *25* (12), 1332–1342.

- (50) Abulnaga, B. *Slurry Systems Handbook*; McGraw-Hill: New York, 2002.
- (51) Haldenwang, R.; Slatter, P.; Chhabra, R. Laminar and transitional flow in open channels for non-Newtonian fluids. In *Proceedings of the 15th International on the Hydraulic Transport of Solids*; Heywood, N. I., Ed.; BHR Group Ltd: Banff, 2002.
- (52) Burger, J.; Haldenwang, R.; Alderman, N. Friction factor-Reynolds number relationship for laminar flow of non-Newtonian fluids in open channels of different cross-sectional shapes. *Chem. Eng. Sci.* **2010**, *65* (11), 3549–3556.
- (53) Burger, J. H.; Haldenwang, R.; Chhabra, R. P.; Alderman, N. J. Power law and composite power law friction factor correlations for laminar and turbulent non-Newtonian open channel flow. *J. Brazilian Soc. Mech. Sci. Eng.* **2015**, *37* (2), 601–612.
- (54) Garcia, F.; Garcia, J.; Padrino, J.; Mata, C.; Trallero, J.; Joseph, D. Power law and composite power law friction factor correlations for laminar and turbulent gas-liquid flow in horizontal pipelines. *Int. J. Multiph. Flow* **2003**, *29*, 1605–1624.
- (55) Stokes, G. G. On the effect of internal friction on fluids on the motion of pendulums. *Trans. Cambridge Philos. Soc.* **1851**, *9*, 48.
- (56) Schiller, L.; Naumann, A. Über die grundlegenden Berechnungen der Schwerkraftaufbereitung. *Z. Ver. Deutsch Ing.* **1933**, *77*, 318–320.
- (57) Rhodes, M. *Introduction to Particle Technology*, 2nd editio.; John Wiley & Sons Ltd, 2008.
- (58) Renaud, M.; Mauret, E.; Chhabra, R. P. Power-Law Fluid Flow Over a Sphere_Average Shear Rate and Drag Coefficient.pdf. *Can. J. Chem. Eng.* **2004**, *82* (5), 1066–1070.
- (59) Chhabra, R. P.; Richardson, J. F. *Non-Newtonian Flow and applied rheology: engineering applications*, 2nd ed.; Butterworth Heinemann: Amsterdam, 2008.
- (60) Dhole, S. D.; Chhabra, R. P.; Eswaran, V. Flow of power-law fluids past a sphere at intermediate reynolds numbers. *Ind. Eng. Chem. Res.* **2006**, *45* (13), 4773–4781.
- (61) Chhabra, R. P. *Bubbles, drops, and particles in non-Newtonian fluids*, 2nd ed.; CRC Taylor & Francis: Boca Raton, FL, 2007.
- (62) Beris, A. N.; Tsamopoulos, J. A.; Armstrong, R. C.; Brown, R. A. Creeping motion of a

- sphere through a Bingham plastic. *J. Fluid Mech.* **1985**, *158*, 219–244.
- (63) Tabuteau, H.; Coussot, P.; de Bruyn, J. R. Drag force on a sphere in steady motion through a yield-stress fluid. *J. Rheol. (N. Y. N. Y.)*. **2006**, *51* (1), 125–137.
- (64) Andres, U. T. Equilibrium and motion of spheres in a viscoplastic liquid. *Sov. Phys. - Dokl.* **1961**, *5*, 753.
- (65) Uhlherr, P. H. T. A novel method for measuring yield stress in static fluids. In *IVth Nat. Conf. Rheol.*; Adelaide, 1986; p 231.
- (66) Schurz, J. The yield stress — an empirical reality. *Rheol. Acta* **1990**, *29*, 170.
- (67) Ansley, R. W.; Smith, T. N. Motion of spherical particles in a Bingham plastic. *AIChE J.* **1967**, *13*, 1193.
- (68) Yoshioka, N.; Adachi, K.; Ishimura, H. On creeping flow of a viscoplastic fluid past a sphere. *Kagaku Kogaku* **1971**, *10*, 1144.
- (69) Atapattu, D. D.; Chhabra, R. P.; Uhlherr, P. H. T. Creeping sphere motion in Herschel–Bulkley fluids: flow field and drag. *J. Non-Newton. Fluid Mech.* **1995**, *59*, 245.
- (70) Wilson, K. C.; Horsley, R. R.; Kealy, T.; Reizes, J. A.; Horsley, M. Direct prediction of fall velocities in non-Newtonian materials. *Int. J. Miner. Process.* **2003**, *71* (1–4), 17–30.
- (71) Prandtl, L. Neuere Ergebnisse Turbulenzforschung. *Z. Ver. Deutsch Ing.* **1933**, *77* (5), 105–144.
- (72) Colebrook, C. F. Turbulent flow in pipes, with particular reference to the transition region between the smooth and rough pipe laws. *J. Inst. Civ. Eng.* **1939**, *11*, 133–156.
- (73) Wilson, K. C.; Thomas, A. D. A new analysis of the turbulent flow of non-Newtonian fluids. *Can. J. Chem. Eng.* **1985**, *63*, 539–546.
- (74) Valentik, L.; Whitmore, R. L. The terminal velocity of spheres in Bingham plastics. *Br. J. Appl. Phys.* **1965**, *16*, 1197.
- (75) Tran, Q. K.; Trinh, D. T.; Horsley, R. R.; Reizes, J. A. Drag coefficients and settling

- velocities of spheres in yield-pseudoplastic slurries. *ASME Appl. Mech. Div.* **1993**, 175, 131.
- (76) Rutgers, R. Relative viscosity and concentration. *Rheol. Acta* **1962**, 2, 305.
- (77) Einstein, A. Berichtigung zu meiner Arbeit: "Eine neue Bestimmung der Moleküldimensionen." *Ann Phys.* **1911**, 34 (2), 591.
- (78) Parsi, F.; Gadala-Maria, F. Fore-and-aft asymmetry in a concentrated suspension of solid spheres. *J. Rheol.* **1987**, 325 (32), 725.
- (79) Thomas, D. G. Transport characteristics of suspension: VIII. A note on the viscosity of Newtonian suspensions of uniform spherical particles. *J. Colloid Sci.* **1965**, 20 (3), 267–277.
- (80) Chakrabandhu, K.; Singh, R. K. Rheological properties of coarse food suspensions in tube flow at high temperatures. *J. Food Eng.* **2005**, 66 (1), 117–128.
- (81) Mahaut, F.; Chateau, X.; Coussot, P.; Ovarlez, G. Yield stress and elastic modulus of suspensions of noncolloidal particles in yield stress fluids. **2008**, 52, 287–313.
- (82) Chateau, X.; Ovarlez, G.; Trung, K. L. Homogenization approach to the behavior of suspensions of noncolloidal particles in yield stress fluids. *J. Rheol. (N. Y. N. Y.)*. **2008**, 52 (2), 489.
- (83) Ovarlez, G.; Mahaut, F.; Deboeuf, S.; Lenoir, N.; Hormozi, S.; Chateau, X. Flows of suspensions of particles in yield stress fluids. *J. Rheol. (N. Y. N. Y.)*. **2015**, 59 (6), 1449–1486.
- (84) Drazer, G.; Koplik, J.; Khusid, B.; Acrivos, A. Deterministic and stochastic behaviour of non-Brownian spheres in sheared suspensions. *J. Fluid Mech.* **2002**, 460 (2002), 307–335.
- (85) Eckstein, E. C.; Bailey, D. G.; Shapiro, A. H. Self-diffusion of particles in shear flow of a suspension. *J. Fluid Mech.* **1977**, 79, 191.
- (86) Rao, R. R.; Mondy, L. A.; Baer, T. A.; Altobelli, S. A.; Stephens, T. S. NMR measurements and simulations of particle migration in non-newtonian fluids. *Chem. Eng. Commun.* **2002**, 189 (1), 1–22.
- (87) Di Felice, R.; Parodi, E. Wall effects on the sedimentation velocity of suspensions in

- viscous flow. *Am. Inst. Chem. Eng. J.* **1996**, 42 (4), 927–931.
- (88) Baldock, T. E.; Tomkins, M. R.; Nielsen, P.; Hughes, M. G. Settling velocity of sediments at high concentrations. **2006**, 51 (2004), 91–100.
- (89) Ovarlez, G.; Bertrand, F.; Coussot, P.; Chateau, X. Shear-induced sedimentation in yield stress fluids. *J. Non-Newton. Fluid Mech.* **2012**, 177–178, 19–28.
- (90) Glowinski, R.; Wachs, A. *On the numerical simulation of viscoplastic fluid flow*; Glowinski, R., Xu, J., Eds.; Elsevier: Amsterdam, 2011.
- (91) Frigaard, I. A.; Nouar, C. On the usage of viscosity regularisation methods for viscoplastic fluid flow computation. *J. Non-Newton. Fluid Mech.* **2005**, 127 (1), 1–26.
- (92) Brady, J. F.; Bossis, G. Stokesian dynamics. *Annu Rev Fluid Mech* **1988**, 20, 111.
- (93) Ladd, A. J. C. Numerical simulations of particulate suspensions via discretized Boltzmann equation: 2. Numerical results. *J. Fluid Mech.* **1994**, 271, 329.
- (94) Martys, N. S. Study of a dissipative particle dynamics based approach for modelling suspensions. *J. Rheol. (N. Y. N. Y.)* **2005**, 49 (2), 401.
- (95) Melrose, J. R.; Ball, R. C. The pathological behaviour of sheared hard spheres with hydrodynamic interactions. *Eurphys Lett* **1995**, 32 (6), 535–540.
- (96) Ekambara, Ak.; Sanders, R. S.; Nandakumar, K.; Masliyah, J. H. Hydrodynamic simulation of horizontal slurry pipeline flow using ANSYS-CFX. *Ind. Eng. Chem. Res.* **2009**, 48 (17), 8159–8171.
- (97) Eesa, M.; Barigou, M. CFD investigation of the pipe transport of coarse solids in laminar power law fluids. *Chem. Eng. Sci.* **2009**, 64 (2), 322–333.
- (98) Siemens PLM Software. STAR-CCM+ User guide. 2017.
- (99) Spelay, R. B.; Adane, K. F.; Sanders, R. S.; Sumner, R. J.; Gillies, R. G. The effect of low Reynolds number flows on pitot tube measurements. *Flow Meas. Instrum.* **2015**, 45, 247–254.
- (100) Antal, S. P.; Lahey, R. T.; Flaherty, J. E. Analysis of phase distribution in fully developed laminar bubbly two-phase flow. *Int. J. Multiph. Flow* **1991**, 17 (5), 635–652.

(101) Tomac, I.; Gutierrez, M. Fluid lubrication effects on particle flow and transport in a channel. *Int. J. Multiph. Flow* **2014**, *65* (October), 143–156.

APPENDIX A: SOFTWARE AND HARDWARE TECHNICAL SPECIFICATIONS

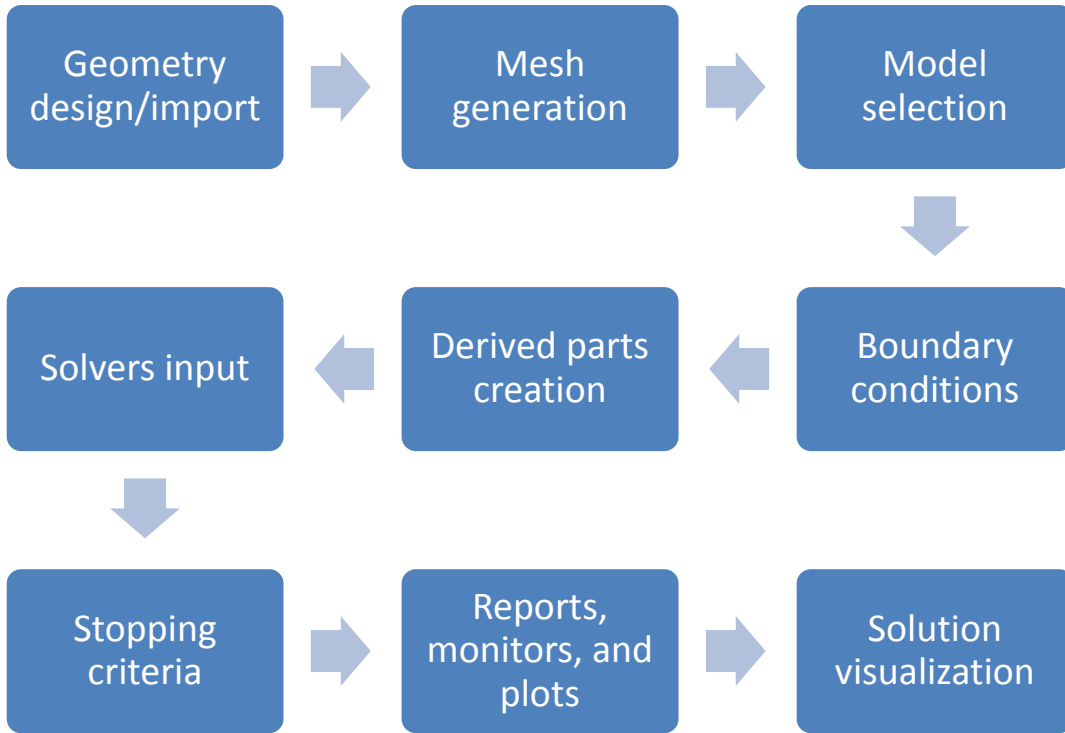


Figure A.1: STAR-CCM+ simulation workflow

SIEMENS
Ingenuity for life

Siemens PLM Software
SIMCENTER
 STAR-CCM+

Version 12.04
 © 2017 Siemens Product Lifecycle Management Software Inc.

Product Version STAR-CCM+ 12.04.010 (win64/intel16.3-r8 Double Precision)
Operating System Microsoft Windows 7 Enterprise version 6.1.7601 running on amd64
System Locale en_US (star)

Java API 1.7.0_75
Java VM Java HotSpot(TM) 64-Bit Server VM 24.75-b04
Java VM Vendor Oracle Corporation
Java Home C:\Program Files\CD-adapco\12.04.010-R8\jdk\win64\jdk1.7.0_75\jre

Figure A.2: STAR-CCM+ version

Table A.1: Computers technical specifications

Computer name	Processor	Number of cores	Installed memory (RAM)	Operating system
BULLDOZER	Intel® Core™ i5-2500 CPU @ 3.30 GHz	4	12.0 GB	Windows 7 Enterprise
CME593617	Intel® Core™ i7-860 CPU @ 2.80 GHz	8	8.0 GB	Windows 7 Professional

APPENDIX B: SIMULATION DATA

Table B.1: Input parameters summary for the simulation results shown on Chapter 3

Case	Inlet depth of flow (m)	Mass flow rate (kg/s)	Time-step (s)	Solution time (s)	Real time (h)	Iterations
1A	0.0782	8.195	0.002	50	5	130,000
1B	0.0656	4.166	0.004	50	3	65,000
1C	0.0598	1.746	0.005	100	2	500,000
1D	0.0618	5.427	0.0015	40	8	140,000
1E	0.0435	2.776	0.005	40	3	50,000
2A	0.0200	2.823	0.0015	10	2	36,000
2B	0.0218	4.125	0.0035	15	2	23,000
2C	0.0249	3.460	0.004	25	3.5	32,000
2D	0.0304	3.432	0.003	30	4	140,000
2E	0.0222	2.131	0.002	35	4	86,000
2F	0.0294	2.767	0.003	35	3	57,000
2G	0.0257	4.159	0.006	20	2	16,000
3A	0.0438	2.863	-	-	1	2,000
3B	0.0587	6.993	-	-	1	1,500
4A	0.0226	3.220	-	-	3	70,000
4B	0.0243	4.450	-	-	2	28,000

Table B.2: Simulation results shown on Chapter 3

Case	\bar{v} (m/s)	h_1 (m)	h_2 (m)	τ_w (Pa)	f	Re_H
1A	0.776	0.07276	0.06994	37.0	0.093	187.1
1B	0.39	0.06670	0.06642	36.4	0.354	48.1
1C	0.17	0.06330	0.06150	33.48	1.846	9.2
1D	0.532	0.06477	0.06896	37.18	0.208	88.8
1E	0.44	0.04537	0.04537	34.91	0.276	60.6
2A	1.808	0.01548	0.01523	15.5	0.006	3121.7
2B	2.142	0.01831	0.01680	15.86	0.005	4363.3
2C	0.998	0.02118	0.02464	10.14	0.014	1240.6
2D	0.66	0.03010	0.02992	9.92	0.029	610.1
2E	1.06	0.02042	0.02030	9.56	0.012	1370.9
2F	0.551	0.02771	0.02783	7.96	0.038	430.2
2G	1.13	0.021332	0.02164	10.21	0.011	1549.6

Table B.3: Simplified simulation results for the centerline velocity profiles for cases 2A, 2B, and 2G

Case 2A		Case 2B		Case 2G	
y/h	v/V	y/h	v/V	y/h	v/V
1.0	1.65	1.0	1.53	1.0	1.43
0.9	1.65	0.9	1.53	0.9	1.43
0.8	1.65	0.8	1.53	0.8	1.43
0.7	1.64	0.7	1.53	0.7	1.43
0.6	1.63	0.6	1.52	0.6	1.42
0.5	1.60	0.5	1.52	0.5	1.42
0.4	1.51	0.4	1.50	0.4	1.39
0.3	1.33	0.3	1.41	0.3	1.30
0.2	1.03	0.2	1.14	0.2	1.06
0.1	0.57	0.1	0.65	0.1	0.63
0.05	0.33	0.05	0.38	0.05	0.34
0	0	0	0	0	0

Table B.4: Simplified simulation results for the centerline velocity profiles for cases 3A, 3B, 4A, and 4B

Case 3A		Case 3B		Case 4A		Case 4B	
y/h	v/V	y/h	v/V	y/h	v/V	y/h	v/V
1.0	1.41	1.0	1.40	1.0	1.16	1.0	1.16
0.9	1.40	0.9	1.40	0.9	1.16	0.9	1.16
0.8	1.38	0.8	1.37	0.8	1.16	0.8	1.16
0.7	1.33	0.7	1.33	0.7	1.16	0.7	1.16
0.6	1.25	0.6	1.25	0.6	1.15	0.6	1.16
0.5	1.15	0.5	1.15	0.5	1.10	0.5	1.15
0.4	1.00	0.4	1.01	0.4	1.10	0.4	1.13
0.3	0.82	0.3	0.82	0.3	1.04	0.3	1.04
0.2	0.60	0.2	0.6	0.2	0.88	0.2	0.87
0.1	0.34	0.1	0.32	0.1	0.57	0.1	0.55
0.05	0.17	0.05	0.17	0.05	0.32	0.05	0.30
0	0	0	0	0	0	0	0

Table B.5: Input parameters summary for the simulation results shown on Chapter 4

Case	Time-step (s)	Solution time (s)	Real time (h)	Iterations
5A	0.0001 – 1.8	1000	1	7500
5B	0.0001 – 1.0	1000	0.5	10500
5C	0.0001 – 0.8	4000	4	26000
6	0.0005	0.75	< 0.5	26000
7	0.0005	0.5	< 0.5	18000
8	0.0005	0.5	< 0.5	20000
9	0.0005	1.0	< 0.5	50000
10A	0.0005	0.5	< 0.5	20000
10B	0.0005	0.75	< 0.5	30000
11A	0.001 – 0.3	2200	2	40000
11B	0.001 – 0.1	1200	1.5	21000

Table B.6: Simplified simulation results for volume fraction profiles for cases 5A, 5B, and 5C

Case 5A		Case 5B		Case 5C	
r/R	ϕ_s	r/R	ϕ_s	r/R	ϕ_s
1.0	0.141	1.0	0.220	1.0	0.382
0.9	0.148	0.9	0.230	0.9	0.396
0.8	0.157	0.8	0.244	0.8	0.413
0.7	0.167	0.7	0.257	0.7	0.431
0.6	0.179	0.6	0.274	0.6	0.450
0.5	0.194	0.5	0.294	0.5	0.471
0.4	0.213	0.4	0.318	0.4	0.498
0.3	0.238	0.3	0.355	0.3	0.522
0.2	0.277	0.2	0.416	0.2	0.557
0.1	0.334	0.1	0.488	0.1	0.581
0.05	0.357	0.05	0.508	0.05	0.588
0	0.357	0	0.521	0	0.589

Table B.7: Simplified simulation results for the centerline velocity profiles for cases 5A, 5B, and 5C

Case 5A		Case 5B		Case 5C	
r/R	v/V	r/R	v/V	r/R	v/V
1.0	0.0	1.0	0.0	1.0	0.0
0.9	0.37	0.9	0.39	0.9	0.39
0.8	0.7	0.8	0.75	0.8	0.72
0.7	0.99	0.7	1.04	0.7	0.98
0.6	1.23	0.6	1.28	0.6	1.18
0.5	1.44	0.5	1.48	0.5	1.33
0.4	1.58	0.4	1.62	0.4	1.42
0.3	1.70	0.3	1.71	0.3	1.48
0.2	1.77	0.2	1.77	0.2	1.51
0.1	1.81	0.1	1.80	0.1	1.53
0.05	1.82	0.05	1.80	0.05	1.53
0	1.83	0	1.80	0	1.53

Table B.8: Simulation results for cases 6, 7, 8, 9, 10A, and 10B

Case	V_t	V^*/V_t	Re^*
6A	1.612	4.79	135.5
6B	1.468	3.88	296.8
7A	0.628	2.77	13.5
7B	0.827	3.19	24.2
8	0.056	0.05	0.7
9	0.250	0.67	4.3
10A	1.019	3.56	57.2
10B	0.48	2.27	9.1
10C	0.856	3.47	38

Table B.9: Simplified simulation results for the volume fraction profiles for cases 11A and 11B

Case 11A		Case 11B	
y/D	ϕ_s	y/D	ϕ_s
1.0	0	1.0	0
0.9	0	0.9	0
0.8	0	0.8	0
0.7	0	0.7	0.005
0.6	0.022	0.6	0.063
0.5	0.265	0.5	0.215
0.4	0.450	0.4	0.332
0.3	0.494	0.3	0.393
0.2	0.533	0.2	0.450
0.1	0.573	0.1	0.504
0.05	0.600	0.05	0.529
0	0.617	0	0.553

Table B.10: Simplified simulation results for the centerline velocity profiles for cases 11A and 11B

Case 11A		Case 11B	
y/D	v/V	y/D	v/V
1.0	0	1.0	0
0.9	1.54	0.9	1.13
0.8	2.48	0.8	1.94
0.7	2.69	0.7	2.25
0.6	2.20	0.6	2.18
0.5	1.45	0.5	1.85
0.4	0.98	0.4	1.40
0.3	0.64	0.3	0.98
0.2	0.38	0.2	0.59
0.1	0.10	0.1	0.24
0.05	0.02	0.05	0.11
0	0	0	0

Table B.11: Input parameters summary for the simulation results shown on Chapter 5

Case	Time-step (s)	Solution time (s)	Real time (h)	Iterations
12A	0.0001 – 0.17	10,000	25	500,000
12B	0.0001 – 1.1	10,000	12	65,000
12C	0.0001 – 0.17	10,000	10	130,000
12D	0.0001 – 0.2	10,000	30	650,000

Table B.12: Simplified simulation results of the volume fraction profiles for cases 12A, 12B, 12C, 12D on Chapter 5

Case 12A		Case 12B		Case 12C		Case 12D	
y/D	ϕ_s	y/D	ϕ_s	y/D	ϕ_s	y/D	ϕ_s
0.64	0.122	0.64	0.098	0.61	0.108	0.55	0.107
0.5	0.125	0.5	0.100	0.5	0.110	0.5	0.109
0.4	0.125	0.4	0.100	0.4	0.110	0.4	0.109
0.3	0.125	0.3	0.100	0.3	0.110	0.3	0.112
0.2	0.127	0.2	0.100	0.2	0.121	0.2	0.110
0.1	0.136	0.1	0.117	0.1	0.120	0.1	0.114
0.05	0.224	0.05	0.221	0.05	0.143	0.05	0.158
0.04	0.254	0.04	0.236	0.04	0.150	0.04	0.138
0.03	0.316	0.03	0.263	0.03	0.168	0.03	0.175
0.02	0.316	0.02	0.293	0.02	0.203	0.02	0.220
0.01	0.350	0.01	0.325	0.01	0.232	0.01	0.233
0	0.366	0	0.326	0	0.261	0	0.280

Table B.13: Simplified simulation results of the velocity profiles for cases 12A, 12B, 12C, 12D on Chapter 5

Case 12A		Case 12B		Case 12C		Case 12D	
y/D	v (m/s)						
0.64	0.478	0.64	0.216	0.61	0.499	0.55	0.576
0.5	0.478	0.5	0.216	0.5	0.499	0.5	0.576
0.4	0.478	0.4	0.216	0.4	0.499	0.4	0.576
0.3	0.478	0.3	0.216	0.3	0.499	0.3	0.576
0.2	0.478	0.2	0.216	0.2	0.499	0.2	0.576
0.1	0.405	0.1	0.194	0.1	0.494	0.1	0.559

Table B.13: Simplified simulation results of the velocity profiles for cases 12A, 12B, 12C, 12D on Chapter 5 (continued)

Case 12A		Case 12B		Case 12C		Case 12D	
y/D	v (m/s)						
0.05	0.006	0.05	0.012	0.05	0.227	0.05	0.245
0.04	0.001	0.04	0.003	0.04	0.115	0.04	0.140
0.03	0.000	0.03	0.000	0.03	0.032	0.03	0.063
0.02	0.000	0.02	0.000	0.02	0.003	0.02	0.019
0.01	0.000	0.01	0.000	0.01	0.000	0.01	0.004
0	0.000	0	0.000	0	0.000	0	0

Table B.14: Simplified simulation results of the volume fraction profiles for case 12B varying solution time

t = 2000s		t = 4000s		t = 6000s		t = 8000s		t = 10000 s	
y/D	ϕ_s	y/D	ϕ_s	y/D	ϕ_s	y/D	ϕ_s	y/D	ϕ_s
0.7	0.094	0.7	0.094	0.7	0.094	0.7	0.094	0.7	0.094
0.62	0.098	0.62	0.098	0.62	0.098	0.62	0.098	0.62	0.098
0.51	0.100	0.51	0.100	0.51	0.100	0.51	0.100	0.51	0.100
0.4	0.100	0.4	0.100	0.4	0.100	0.4	0.100	0.4	0.100
0.3	0.100	0.3	0.100	0.3	0.100	0.3	0.100	0.3	0.100
0.2	0.100	0.2	0.100	0.2	0.100	0.2	0.100	0.2	0.100
0.1	0.100	0.1	0.105	0.1	0.110	0.1	0.114	0.1	0.117
0.05	0.133	0.05	0.158	0.05	0.184	0.05	0.205	0.05	0.221
0.04	0.134	0.04	0.169	0.04	0.199	0.04	0.220	0.04	0.236
0.03	0.160	0.03	0.200	0.03	0.229	0.03	0.248	0.03	0.263
0.02	0.192	0.02	0.228	0.02	0.254	0.02	0.274	0.02	0.293
0.01	0.216	0.01	0.251	0.01	0.276	0.01	0.302	0.01	0.325
0	0.239	0	0.274	0	0.298	0	0.294	0	0.326

Table B.15: Wall shear stress and maximum particle concentration at the bottom of the channel along the flow axis for case 12B

Distance from the channel inlet (m)	Wall shear stress (Pa)	Maximum particle volume fraction
2	52.6	0.148
4	53.8	0.182
6	56.1	0.217
8	58.7	0.258
10	60.4	0.274
12	64.7	0.300
14	67.7	0.316
16	69.0	0.346
18	67.5	0.278

Table B.16: Simplified results of the particle volume fraction profiles with varying yield stress

$\tau_y = 20 \text{ Pa}$		$\tau_y = 40 \text{ Pa}$		$\tau_y = 60 \text{ Pa}$	
y/D	ϕ_s	y/D	ϕ_s	y/D	ϕ_s
0.7	0.094	0.7	0.094	0.7	0.093
0.62	0.098	0.62	0.098	0.62	0.098
0.51	0.100	0.51	0.100	0.51	0.100
0.4	0.100	0.4	0.100	0.4	0.100
0.3	0.100	0.3	0.100	0.3	0.100
0.2	0.100	0.2	0.100	0.2	0.101
0.1	0.107	0.1	0.117	0.1	0.126
0.05	0.211	0.05	0.221	0.05	0.221
0.04	0.243	0.04	0.236	0.04	0.228
0.03	0.287	0.03	0.263	0.03	0.251
0.02	0.313	0.02	0.293	0.02	0.278
0.01	0.339	0.01	0.325	0.01	0.317
0	0.328	0	0.326	0	0.342

Table B.17: Simplified results of velocity profiles with varying yield stress

$\tau_y = 20 \text{ Pa}$		$\tau_y = 40 \text{ Pa}$		$\tau_y = 60 \text{ Pa}$	
y/D	$v \text{ (m/s)}$	y/D	$v \text{ (m/s)}$	y/D	$v \text{ (m/s)}$
0.7	0.211	0.7	0.216	0.7	0.222
0.62	0.211	0.62	0.216	0.62	0.222
0.51	0.211	0.51	0.216	0.51	0.222
0.4	0.211	0.4	0.216	0.4	0.222
0.3	0.211	0.3	0.216	0.3	0.222
0.2	0.211	0.2	0.216	0.2	0.222
0.1	0.202	0.1	0.194	0.1	0.169
0.05	0.019	0.05	0.012	0.05	0.005
0.04	0.004	0.04	0.003	0.04	0.001
0.03	0.000	0.03	0.000	0.03	0.000
0.02	0.000	0.02	0.000	0.02	0.000
0.01	0.000	0.01	0.000	0.01	0.000
0	0.000	0	0.000	0	0.000

Table B.18: Simplified results of the particle volume fraction profiles with channel geometry

Constant h/D		Constant h		Rectangular channel	
y/D	ϕ_s	y/h	ϕ_s	y/h	ϕ_s
-	-	1.0	0.087	1.0	0.095
-	-	0.9	0.100	0.9	0.098
-	-	0.8	0.100	0.8	0.100
0.7	0.093	0.7	0.101	0.7	0.100
0.62	0.100	0.6	0.109	0.6	0.100
0.51	0.100	0.5	0.102	0.5	0.100
0.4	0.104	0.4	0.113	0.4	0.100
0.3	0.100	0.3	0.114	0.3	0.101
0.2	0.105	0.2	0.132	0.2	0.110
0.1	0.115	0.1	0.224	0.1	0.151
0.05	0.212	0.05	0.310	0.05	0.246

Table B.18: Simplified results of the particle volume fraction profiles with channel geometry (continued)

Constant h/D		Constant h		Rectangular channel	
y/D	ϕ_s	y/h	ϕ_s	y/h	ϕ_s
0.04	0.243	0.04	0.332	0.04	0.271
0.03	0.281	0.03	0.357	0.03	0.306
0.02	0.335	0.02	0.388	0.02	0.345
0.01	0.378	0.01	0.385	0.01	0.362
0	0.375	0	0.382	0	0.355

Table B.19: Simplified results of the velocity profiles with channel geometry

Constant h/D		Constant h		Rectangular channel	
y/D	v (m/s)	y/h	v (m/s)	y/h	v (m/s)
-	-	1.0	0.231	1.0	0.254
-	-	0.9	0.231	0.9	0.254
-	-	0.8	0.231	0.8	0.254
0.7	0.217	0.7	0.231	0.7	0.254
0.62	0.217	0.6	0.231	0.6	0.254
0.51	0.217	0.5	0.231	0.5	0.254
0.4	0.217	0.4	0.229	0.4	0.253
0.3	0.217	0.3	0.221	0.3	0.247
0.2	0.217	0.2	0.200	0.2	0.210
0.1	0.198	0.1	0.018	0.1	0.065
0.05	0.015	0.05	0.000	0.05	0.001
0.04	0.003	0.04	0.000	0.04	0.000
0.03	0.000	0.03	0.000	0.03	0.000
0.02	0.000	0.02	0.000	0.02	0.000
0.01	0.000	0.01	0.000	0.01	0.000
0	0.000	0	0.000	0	0.000

Table B.20: Simplified results of the particle volume fraction profiles with varying particle diameter

d = 0.27 mm		d = 1 mm	
y/D	ϕ_s	y/D	ϕ_s
0.7	0.093	0.7	0.087
0.62	0.098	0.62	0.096
0.51	0.100	0.51	0.100
0.4	0.100	0.4	0.100
0.3	0.100	0.3	0.100
0.2	0.100	0.2	0.102
0.1	0.123	0.1	0.176
0.05	0.238	0.05	0.299
0.04	0.250	0.04	0.336
0.03	0.281	0.03	0.370
0.02	0.319	0.02	0.371
0.01	0.345	0.01	0.386
0	0.340	0	0.333

Table B.21: Simplified results of the velocity profiles with varying particle diameter

d = 0.27 mm		d = 1 mm	
y/D	v (m/s)	y/D	v (m/s)
0.7	0.216	0.7	0.222
0.62	0.216	0.62	0.222
0.51	0.216	0.51	0.222
0.4	0.216	0.4	0.222
0.3	0.216	0.3	0.222
0.2	0.216	0.2	0.222
0.1	0.186	0.1	0.073
0.05	0.006	0.05	0.000
0.04	0.001	0.04	0.000
0.03	0.000	0.03	0.000
0.02	0.000	0.02	0.000
0.01	0.000	0.01	0.000
0	0.000	0	0.000

Table B.22: Simplified results of the particle volume fraction profiles with varying particle bulk volume fraction

$\phi_{s,bulk} = 0.2$		$\phi_{s,bulk} = 0.3$	
y/D	ϕ_s	y/D	ϕ_s
0.7	0.191	0.7	0.291
0.62	0.197	0.62	0.297
0.51	0.200	0.51	0.300
0.4	0.200	0.4	0.300
0.3	0.200	0.3	0.300
0.2	0.200	0.2	0.301
0.1	0.212	0.1	0.307
0.05	0.271	0.05	0.338
0.04	0.278	0.04	0.341
0.03	0.296	0.03	0.352
0.02	0.314	0.02	0.362
0.01	0.324	0.01	0.368
0	0.335	0	0.376

Table B.23: Simplified results of the velocity profiles with varying particle bulk volume fraction

$\phi_{s,bulk} = 0.2$		$\phi_{s,bulk} = 0.3$	
y/D	v (m/s)	y/D	v (m/s)
0.62	0.210	0.62	0.208
0.51	0.210	0.51	0.208
0.4	0.210	0.4	0.208
0.3	0.210	0.3	0.208
0.2	0.210	0.2	0.208
0.1	0.209	0.1	0.207
0.05	0.056	0.05	0.097
0.04	0.022	0.04	0.053
0.03	0.006	0.03	0.024
0.02	0.001	0.02	0.009
0.01	0.000	0.01	0.003
0	0.000	0	0.000

Table B.24: Simplified results of the particle volume fraction profiles with varying particle mixture density

$\rho_m = 1750 \text{ kg/m}^3$		$\rho_m = 2000 \text{ kg/m}^3$	
y/D	ϕ_s	y/D	ϕ_s
0.7	0.095	0.7	0.096
0.62	0.098	0.62	0.099
0.51	0.100	0.51	0.100
0.4	0.100	0.4	0.100
0.3	0.100	0.3	0.100
0.2	0.100	0.2	0.100
0.1	0.107	0.1	0.105
0.05	0.151	0.05	0.132
0.04	0.158	0.04	0.132
0.03	0.185	0.03	0.132
0.02	0.212	0.02	0.150
0.01	0.231	0.01	0.189
0	0.251	0	0.205

Table B.25: Simplified results of the velocity profiles with varying particle mixture density

$\rho_m = 1750 \text{ kg/m}^3$		$\rho_m = 2000 \text{ kg/m}^3$	
y/D	$v \text{ (m/s)}$	y/D	$v \text{ (m/s)}$
0.7	0.210	0.7	0.210
0.62	0.210	0.62	0.210
0.51	0.210	0.51	0.210
0.4	0.210	0.4	0.210
0.3	0.210	0.3	0.210
0.2	0.210	0.2	0.210
0.1	0.208	0.1	0.208
0.05	0.096	0.05	0.121
0.04	0.052	0.04	0.079
0.03	0.021	0.03	0.042
0.02	0.006	0.02	0.018
0.01	0.001	0.01	0.006
0	0.000	0	0.000

Table B.26: Simplified results of the particle volume fraction profiles with varying flow rate

Q = 3.75 L/s		Q = 5 L/s	
y/D	ϕ_s	y/D	ϕ_s
0.7	0.095	0.7	0.096
0.62	0.100	0.62	0.099
0.51	0.100	0.51	0.100
0.4	0.100	0.4	0.100
0.3	0.100	0.3	0.100
0.2	0.100	0.2	0.100
0.1	0.108	0.1	0.103
0.05	0.170	0.05	0.134
0.04	0.183	0.04	0.135
0.03	0.215	0.03	0.162
0.02	0.244	0.02	0.195
0.01	0.266	0.01	0.220
0	0.289	0	0.247

Table B.27: Simplified results of the particle volume fraction profiles with varying flow rate

Q = 3.75 L/s		Q = 5 L/s	
y/D	v/V	y/D	v/V
0.7	1.11	0.7	1.10
0.62	1.11	0.62	1.10
0.51	1.11	0.51	1.10
0.4	1.11	0.4	1.10
0.3	1.11	0.3	1.10
0.2	1.11	0.2	1.10
0.1	1.09	0.1	1.09
0.05	0.31	0.05	0.66
0.04	0.13	0.04	0.42
0.03	0.04	0.03	0.21
0.02	0.01	0.02	0.08
0.01	0.00	0.01	0.02
0	0.00	0	0.00